

Modeling and Control for Microgrids

by

Joel Steenis

A Dissertation Presented in Partial Fulfillment
of the Requirements for the Degree
Doctor of Philosophy

Approved August 2013 by the
Graduate Supervisory Committee:

Raja Ayyanar, Chair

Raja Ayyanar

Hans Mittelmann

Konstantinos Tsakalis

Daniel Tylavsky

ARIZONA STATE UNIVERSITY

December 2013

ABSTRACT

Traditional approaches to modeling microgrids include the behavior of each inverter operating in a particular network configuration and at a particular operating point. Such models quickly become computationally intensive for large systems. Similarly, traditional approaches to control do not use advanced methodologies and suffer from poor performance and limited operating range.

In this document a linear model is derived for an inverter connected to the Thevenin equivalent of a microgrid. This model is then compared to a nonlinear simulation model and analyzed using the open and closed loop systems in both the time and frequency domains. The modeling error is quantified with emphasis on its use for controller design purposes.

Control design examples are given using a Glover McFarlane controller, gain scheduled Glover McFarlane controller, and bumpless transfer controller which are compared to the standard droop control approach. These examples serve as a guide to illustrate the use of multi-variable modeling techniques in the context of robust controller design and show that gain scheduled MIMO control techniques can extend the operating range of a microgrid. A hardware implementation is used to compare constant gain droop controllers with Glover McFarlane controllers and shows a clear advantage of the Glover McFarlane approach.

DEDICATION

This work is dedicated my parents, Richard and Marsha Steenis, for a lifetime of support and encouragement.

ACKNOWLEDGEMENTS

The author wishes to thank the FREEDM systems center at North Carolina State University, the LightWorks initiative at Arizona State University, and Arizona State University for funding. The author would also like to thank Dr. Ayyanar and Dr. Tsakalis for support and Lloyd Breazeale for assistance with the hardware.

TABLE OF CONTENTS

	Page
LIST OF TABLES	vi
LIST OF FIGURES	vii
CHAPTER	
1 INTRODUCTION AND BACKGROUND	1
1.1 What is a microgrid?	1
1.2 What is a solid state transformer?	2
1.3 Problem definition, research objectives, and contributions.	3
1.4 Survey of Microgrid Control	6
Droop Control	6
Master-Slave Control	13
Current Mode Control	15
2 ANALYTICAL SYSTEM MODELS	19
2.1 Model Derivation for Voltage Sources with Constant Gain Droop Control	19
2.2 A Generalized Model for Converters with Constant Gain Droop Control	25
2.3 A General Linear Model for Robust Controller Design	30
Model Validation	32
3 COPRIME FACTORIZATION AND THE GAP METRIC	40
4 GLOVER MCFARLANE LOOPSHAPING BACKGROUND	43
4.1 Glover-McFarlane Loopshaping Applied to Droop Control with Dy- namics	44
Synthesizing Glover McFarlane Controllers for a Small Microgrid . .	44
Nine-Inverter Microgrid Testbed	49
5 GAIN SCHEDULED CONTROLLER SYNTHESIS	67

CHAPTER	Page
5 GAIN SCHEDULED CONTROLLER SYNTHESIS	67
5.1 Gain Scheduling Based on Line Phase	67
5.2 Polytopic and Affine System Models	69
Polytopic Representations	70
Affine Representations	71
Quadratic Stability	73
5.3 The Family of Plants	73
5.4 Synthesis of Gain Scheduled Glover McFarlane Controller	73
5.5 Bumpless Control	80
Representing the Scheduling Parameters in Polytopic Coordinates and Controller Selection	83
Simulation Example	84
Application to an Inverter	87
6 HARDWARE IMPLEMENTATION	91
6.1 Power Calculation	91
6.2 Control Design	92
6.3 Hardware Results	94
7 SUMMARY AND CONCLUSIONS	105
REFERENCES	106

LIST OF TABLES

Table	Page
2.1 Parameters used in the system where one inverter has virtual output impedance control.	27
2.2 Parameters used to validate the open loop model.	33
2.3 Parameters used to validate the closed loop model.	33
4.1 Parameters used in the design and validation of the proposed controller. Note that the inverter parameters are given in terms of their maximum values and grid parameters are given in terms of their nominal values.	46
4.2 Results of report generated using the Matlab command “robuststab”. Note that the sensitivity is the reduction in stability margin divided by change in the given parameter. The standard abbreviation for “with respect to” wrt is used here. . .	48
4.3 Range of values about nominal operating point. Note that “ Δ ” is a factor denoting the tolerance of any given parameter value.	49
4.4 Parameters used in the testing of the nine-inverter microgrid.	53
5.1 Two uncertainty descriptions for a family of plants.	74
6.1 Parameters used for both inverter 1 and inverter 2 shown in Figure 6.15. . . .	102

LIST OF FIGURES

Figure	Page
1.1 Average model of a solid state transformer.	3
1.2 High level diagram of SST with droop control.	4
1.3 Two loop (current mode) control with inductor current and output voltage feed-back.	5
1.4 A system with two voltage sources. Note that the variable “S” denotes complex power transfer between the two sources.	6
1.5 Power transferred between two inverters. Please refer to equations (1.16) and (1.17).	10
1.6 Conventional variations of droop control.	12
1.7 Master-slave control for a system of two inverters.	14
1.8 Two loop (current mode) control with inductor feedback.	16
1.9 Current sharing with two inverters.	17
1.10 CMC with modified output impedance.	18
2.1 Sequence of approximations used to model the SST.	20
2.2 Flowchart illustrating how the virtual output impedance is derived.	26
2.3 Block diagram illustrating how the virtual output impedance is implemented.	27
2.4 Virtual output resistance necessary to ensure inverter stability.	28
2.5 Transient response of inverter without output impedance control.	29
2.6 Transient response of inverter with output impedance control.	29
2.7 Inverter connected to Thevenin equivalent of the microgrid.	30
2.8 Two inverter system.	31
2.9 Two inverter system where “ $Z_{e^{j\theta}}$ ” is the sum of the line and Thevenin impedances.	34
2.10 Conventional implementation of droop control.	34

Figure	Page
2.11 Bode plot of system transfer function using droop parameters in Table 2.3. Note: The typical MIMO convention is used where the rows and columns represent the two outputs and inputs respectively.	34
2.12 Transient power response of open loop linear and nonlinear systems for a sequence of perturbations in frequency. The percent error plot quantifies the linearization error.	35
2.13 Transient power response of open loop linear and nonlinear systems for a sequence of perturbations in voltage. The percent error plot quantifies the linearization error.	36
2.14 Transient power response of closed loop linear and nonlinear systems for a sequence of perturbations in frequency. The error is quite small and is dominated by 120 Hz ripple from the nonlinear model. The percent error plot quantifies the linearization error.	37
2.15 Transient power response of closed loop linear and nonlinear systems for a sequence of perturbations in voltage. The percent error plot quantifies the linearization error.	38
2.16 Multiplicative uncertainty of open loop system for perturbations in frequency. .	38
2.17 Multiplicative uncertainty of closed loop system for perturbations in voltage. . .	39
2.18 Illustration of linearization error ($\Delta_m(s)$) and derivation of closed loop constraint based on the small gain theorem [49].	39
3.1 Block diagram representation of coprime factorized system with uncertainty. . .	42
3.2 Block diagram representation of system with exogenous inputs and outputs. . .	42
4.1 Problem formulation used to design dynamic controller.	44
4.2 Problem formulation used to design a controller “k”.	45

Figure	Page
4.3 Bode magnitude plot of the plant. Note: The typical MIMO convention is used where the rows and columns represent the two outputs and inputs respectively. .	46
4.4 Sigma plot of the inverter sensitivity and complementary sensitivity responses when using a Glover McFarlane loopshaping controller.	47
4.5 Sigma plot of the inverter sensitivity and complementary sensitivity responses when using conventional droop control with no dynamics.	47
4.6 Stability margin for constant gain droop control over a wide range of gains. The stability margin is defined as the reciprocal of the gap metric in equation (4.4) in the first section of this chapter.	49
4.7 Stability margin for Glover McFarlane controllers with a wide range of DC gains. The stability margin is defined as the reciprocal of the gap metric in equation (4.4) in the first section of this chapter.	50
4.8 This figure illustrates the difference between stability margins for Glover McFarlane and constant gain droop controllers with a wide range of DC gains. The stability margin is defined as the reciprocal of the gap metric in equation (4.4) in the first section of this chapter.	50
4.9 This illustrates the gap between plants with parameter values in the set in Table 4.3.	51
4.10 A microgrid with nine inverters.	52
4.11 Transient power response of inverters 1 – 3 in the nine-inverter microgrid shown in Figure 4.10. Each inverter uses CGDC.	55
4.12 Transient power response of inverters 4 – 6 in the nine-inverter microgrid shown in Figure 4.10. Each inverter uses CGDC.	55
4.13 Transient power response of inverters 7 – 9 in the nine-inverter microgrid shown in Figure 4.10. Each inverter uses CGDC.	56

Figure	Page
4.14 Transient power response of inverters 1 – 3 in the nine-inverter microgrid shown in Figure 4.10. Each inverter uses conventional droop control with virtual output resistance.	56
4.15 Transient power response of inverters 4 – 6 in the nine-inverter microgrid shown in Figure 4.10. Each inverter uses conventional droop control with virtual output resistance.	57
4.16 Transient power response of inverters 7 – 9 in the nine-inverter microgrid shown in Figure 4.10. Each inverter uses conventional droop control with virtual output resistance.	57
4.17 Transient power response of inverters 1 – 3 in the nine-inverter microgrid shown in Figure 4.10. Each inverter uses conventional droop control with virtual output inductance.	58
4.18 Transient power response of inverters 4 – 6 in the nine-inverter microgrid shown in Figure 4.10. Each inverter uses conventional droop control with virtual output inductance.	58
4.19 Transient power response of inverters 7 – 9 in the nine-inverter microgrid shown in Figure 4.10. Each inverter uses conventional droop control with virtual output inductance.	59
4.20 Transient power response of inverters 1 – 3 in the nine-inverter microgrid shown in Figure 4.10. Each inverter uses GMFDC.	59
4.21 Transient power response of inverters 4 – 6 in the nine-inverter microgrid shown in Figure 4.10. Each inverter uses GMFDC.	60
4.22 Transient power response of inverters 7 – 9 in the nine-inverter microgrid shown in Figure 4.10. Each inverter uses GMFDC.	60
4.23 An alternate microgrid configuration with nine inverters.	61

Figure	Page
4.24 Transient power response of inverters 1 – 3 in the alternative configuration of the nine-inverter microgrid shown in Figure 4.23. Each inverter uses a Glover McFarlane loopshaping controller.	62
4.25 Transient power response of inverters 4 – 6 in the alternative configuration of the nine-inverter microgrid shown in Figure 4.23. Each inverter uses a Glover McFarlane loopshaping controller.	62
4.26 Transient power response of inverters 7 – 9 in the alternative configuration of the nine-inverter microgrid shown in Figure 4.23. Each inverter uses a Glover McFarlane loopshaping controller.	63
4.27 Nine inverter microgrid with dynamic load.	63
4.28 Parameters for dynamic load for the system shown in Figure 4.27.	64
4.29 Top level for dynamic load model used in the system shown in Figure 4.27. . .	64
4.30 Model for dynamic load for the system shown in Figure 4.29. Note that the top level of the model is shown in Figure 4.29 and this figure is the contents of the “model” block in the same figure.	65
4.31 Transient power response of inverters 1-3 as shown in Figure 4.27.	65
4.32 Transient power response of inverters 1-3 as shown in Figure 4.27.	66
4.33 Transient power response of inverters 1-3 as shown in Figure 4.27.	66
5.1 Two inverter system.	67
5.2 Implementation of the rotational transformation based on line impedance. . . .	69
5.3 Block diagram of linear parameter dependent system and gs GMFDC controller implemented in Simulink.	74
5.4 Plot of the plant coefficients as shown in Figure 5.3.	75
5.5 Transient PQ response of parameter dependent system in Figure 5.3. This plot is for a parameter dependent system with a CGDC.	76

Figure	Page
5.6 Transient PQ response of parameter dependent system in Figure 5.3. This plot is for a parameter dependent system with a GMFDC.	76
5.7 Transient PQ response of parameter dependent system in Figure 5.3. This plot is for a parameter dependent system with a gain scheduled GMFDC.	77
5.8 This figure contains Bode magnitude plots for the system at several instants in time. These Bode plots may be thought of as “snapshots” of the plant magnitude response as the system evolves over time. Corresponding “snapshots” of the gain scheduled controller are contained in Figure 5.9.	78
5.9 This figure contains Bode magnitude plots for the gain scheduled controller at several instants in time. These Bode plots may be thought of as “snapshots” of the controller magnitude response as the system evolves over time. Corresponding “snapshots” of the plant are contained in Figure 5.8.	78
5.10 This figure contains Bode magnitude plots for the plant at several instants in time. These Bode plots may be thought of as “snapshots” of the controller magnitude response as the system evolves over time.	79
5.11 This figure contains Bode magnitude plots for the gain scheduled controller at several instants in time. These Bode plots may be thought of as “snapshots” of the controller magnitude response as the system evolves over time.	79
5.12 Plant with a set of “n” conventional, “bumpy” controllers. These plants are bumpy since switching between them will result in discontinuities at the plant input.	80
5.13 Hypothetical transient plot of plant input “u” with a set of conventional, “non-bumpless” controllers. Clearly the discontinuity will perturb the system and create undesirable issues. The purpose of bumpless control is to minimize the discontinuity shown in this figure.	81

Figure	Page
5.14 Plant with a set of “n” bumpless controllers. These controllers are called bumpless because the discontinuity between controller outputs is negligible.	81
5.15 Implementation of a bumpless controller. Note that when the controller is not active, the switch “S” is open and the feedback gain “L” is used to drive the output of the controller to the current value of the active controller (not shown) at the output.	82
5.16 This block diagram illustrates the selection of a bumpless controller based on the distance between vertices in a polytope. The selection is based on the nearest vertex in a polytope. When the difference between the nearest vertex and second nearest vertex is less than a specified value then one may say that the vertices are equidistant or nearly equidistant. Under such conditions chatter may occur, thus the deadband and memory blocks simply and easily incorporate hysteresis to eliminate such issues.	85
5.17 Parametric plot of normalized parameter trajectories. Note the trajectory of the parameters is counterclockwise in time from 0 seconds to 10 seconds.	86
5.18 Plot of polytopic coordinates and enable signal to select the nearest vertex. The state of the logic signal in time ensures that the controller selection will not chatter between controllers. For this example the deadband threshold is selected as 0.3 and is the distance between the maximum weight and second largest weight in order for a switching event to occur.	87
5.19 Parametric plot of normalized parameter trajectories. Note the trajectory of the parameters is counterclockwise in time from 0 seconds to 10 seconds.	88

5.20	Plot of polytopic coordinates and enable signal to select the nearest vertex. The state of the logic signal in time ensures that the controller selection will not chatter between controllers. For this example the deadband threshold is selected as 0.3 and is the distance between the maximum weight and second largest weight in order for a switching event to occur.	88
5.21	Transient active and reactive power response for an inverter using a set of 16 bumpless controllers. The inline controller is chosen according to the nearest vertex (largest weight for the gain scheduled case). The parameters for the system are given in Table 2.3 with a 2 rad/s perturbation at $t = 1$ second and 2 V perturbation at $t = 2$ seconds.	89
5.22	Transient active and reactive power response for an inverter using a set of 4 bumpless controllers. The inline controller is chosen according to the nearest vertex (largest weight for the gain scheduled case). The parameters for the system are given in Table 2.3 with a 2 rad/s perturbation at $t = 1$ second and 2 V perturbation at $t = 2$ seconds.	90
6.1	Two-inverter configuration used in the hardware implementation.	91
6.2	Methodology used to calculate the active and reactive inverter output power. Note that the sinusoidal voltage input is assumed to be the output of the droop control and the co-sinusoidal input is derived from the same source.	92
6.3	Sigma plot of the controller synthesized using the weight (6.3).	93
6.4	Sigma plot of the controller synthesized using the weight (6.6).	94

Figure	Page
6.5 Transient plot comparing two system configurations. One configuration uses two CGDC and the other system configuration uses two GMFDC. It can be seen that the system with CGDC is poorly damped, but is stable. This is an indication of the conservative nature of the gap margin. It will be shown in section 6.3 that CGDC is not robust and destabilizes the physical system.	95
6.6 Photograph of one, 5 kw, single phase inverter, with DSP driving a parallel RC load.	96
6.7 Architecture used to test open loop frequency perturbations in hardware.	96
6.8 Architecture used to test open loop voltage perturbations in hardware.	97
6.9 Methodology used to characterize Thevenin equivalent of auto-transformer. . .	98
6.10 This figure depicts parasitics that influence hardware. Note that the inverter output impedance is negligible for this particular case. In general it is good to consider the effect of inverter output impedance and include or exclude it accordingly.	99
6.11 Transient response of active power (top) and reactive power (bottom) for a perturbation of 0.05 rad/s.	100
6.12 Transient response of active power (top) and reactive power (bottom) for a perturbation of 0.1 rad/s.	100
6.13 Transient response of active power (top) and reactive power (bottom) for a perturbation of 2V.	101
6.14 Transient response of active power (top) and reactive power (bottom) for a perturbation of 5V.	101
6.15 Two-inverter configuration used in the hardware implementation.	102

6.16 Comparison of transient power response using hardware. Inverters 1 and 2 are configured as shown in Figure 6.15. Controller 1 denotes a controller with larger DC gain than controller 2. The inverters using constant gain controllers are clearly unstable and the inverters using GMFDC controllers are stable and well behaved. It can be seen the the DC gain and dynamics, or lack of dynamics, have a strong impact on the stability and dynamic performance of the system.	103
6.17 Comparison of transient voltage and current response using hardware. Inverters 1 and 2 are configured as shown in Figure 6.15. Controller 1 denotes a controller with larger DC gain than controller 2. The inverters using constant gain controllers are clearly unstable and the inverters using GMFDC controllers are stable and well behaved. It can be seen the the DC gain and dynamics, or lack of dynamics, have a strong impact on the stability and dynamic performance of the system.	104

NOMENCLATURE

A, A	Ampere (Current value) or System state-space A matrix (Determined by content)
AC	Alternating current
AC-DC	Conversion from AC voltage to DC voltage
B	System state-space B matrix
C	System state-space C matrix
CCA	Cycle-by-cycle average
CGDC	Constant gain droop control
CLC	Capacitive-inductive-capacitive filter
CMC	Current mode control
D	System state-space D matrix
DAB	Dual-active-bridge
DC	Direct current
DC-DC	Conversion from DC voltage to DC voltage
DER	Distributed energy resources
DES	Distributed energy storage

NOMENCLATURE Continued

det	Matrix determinant
DESD	Distributed energy storage device
DG	Distributed generation
DRER	Distributed renewable energy resources
DSP	Digital signal processor
F	Faraday (Capacitance value)
$F_l(M, \Delta_l)$	Lower linear fractional transformation of M and Δ_l
$F_u(M, \Delta_u)$	Upper linear fractional transformation of M and Δ_u
FREEDM	Future Renewable Electric Energy Delivery and Management
f_s	Switching frequency (Hertz)
GMFDC	Glover McFarlane droop control
H	Henry (Inductance value)
HF	High frequency
HVAC	High voltage AC
HVDC	High voltage DC
Hz	Hertz (measurement of frequency)

NOMENCLATURE Continued

i	Denotes current in this report. This character is sometimes used to denote the imaginary unit $\sqrt{-1}$. In this report, the imaginary unit will be denoted by j .
Island	An interconnection of SST's that are self sufficient. (not connected to the utility grid)
j	The imaginary unit $\sqrt{-1}$
kHz	kilo Hertz
kVA	kilo Volt-Ampere
kW	kilo Watts
LC	Inductive-capacitive filter
LFT	Linear fractional transformation
LHP	Left half plane. (This refers to complex numbers with real part less than zero.)
LMI	Linear matrix inequality
LPF	Low pass filter
LTI	Linear time invariant
LVDC	Low voltage DC

NOMENCLATURE Continued

MAB	Multi-active-bridge
max	Maximum value
MHB	Multi-half-bridge
MIMO	Multiple-input-multiple-output
min	Minimum value
ms	millisecond
N/A	Not Applicable
P	Active power
PCC	Point of common coupling
PFC	Power-factor-correction
PID	Proportional Integral Differential
PLL	Phase locked loop
PV	Photovoltaic
PWM	Pulse-width modulation
Q	Reactive power
QAB	Quad-active-bridge

NOMENCLATURE Continued

R	Ohmic resistance
RHP	Right half plane. (This refers to complex numbers with real part greater than zero.)
RMS	Root mean square
rad/s	Radians per second
S	Sensitivity function
\vec{S}	Complex power
sec	Second
SISO	Single-input-single-output
SST	Solid state transformer
T	Complimentary sensitivity function
THD	Total harmonic distortion
u	Control variable in state space representation
VA	Volt-Ampere
V	Voltage
V_{Batt}	Battery voltage

NOMENCLATURE Continued

X	Ohmic reactance
x	State variable in state space representation
y	Output variable in state space representation
\vec{Z}	Complex impedance
$\ \cdot\ _n$	Denotes the n-norm of \cdot
Ω	Ohms (Resistance value)
ω_s	Switching frequency (rad/s)
θ	Phase angle of complex line impedance (arctan of resistance divided by reactance).
δ	This is used to denote the phase difference between two voltage sources and the gap metric.
μs	Micro second
$\bar{\sigma}(M)$	Maximum singular value of matrix M
$\underline{\sigma}(M)$	Minimum singular value of matrix M
\Re	Real part of complex number
\Im	Imaginary part of complex number

A Note on Convention

Every attempt has been made to make this document as readable as possible. While not strictly enforced, one may in general assume the following:

Upper case variables are phasors, DC quantities, or matrices.

Lower case variables are time varying quantities, scalars, or integer indices.

Voltage, current, and power are expressed using RMS values unless stated otherwise.

Any exception from this convention is typically made to draw a distinction that would otherwise be unclear. The nature of the quantities drawn to exception should be obvious from the context in which they are used.

Chapter 1

INTRODUCTION AND BACKGROUND

1.1 What is a microgrid?

Use of the term microgrid may be somewhat ambiguous and has evolved over time. The traditional definition of a microgrid is succinctly defined by Lasseter [33] as the following:

“The microGrid concept assumes a cluster of loads and microsources operating as a single controllable system that provides both power and heat to its local area.

To the utility the microgrid can be thought of as a controlled cell of the power system. For example this cell could be controlled as a single dispatchable load, which can respond in seconds to meet the needs of the transmission system. To the customer the microgrid can be designed to meet their special needs; such as, enhance local reliability, reduce feeder losses, support local voltages, provide increased efficiency through use waste heat, voltage sag correction or provide uninterruptible power supply functions to name a few.”

In this report a microgrid is considered to be an interconnection of power electronic converters (power inverters or solid state transformers) that facilitate the integration of renewable energy into the grid and is consistent with the emerging concept of an energy internet [26].

In the envisioned energy internet, energy is exchanged in a way analogous to the way information is exchanged on the internet. The transition to the envisioned paradigm may be realized if there is an interruption in service of the utility grid and the microgrid continues to operate, thereby providing service to its users. The distributed nature of

energy generation lends itself to lower transmission losses since the energy sources may be located near the load and reduces the effect of clouds with PV generation or aberrations in wind, with wind generation. The success of such projects is contingent on the stabilization and performance of power electronic sources over a wide range of operating conditions and configurations as discussed in this report.

1.2 What is a solid state transformer?

It is common to refer to power electronic sources in a microgrid simply as “inverters”. Use of this term refers to the conversion of a DC voltage to an AC one, and neglects additional functionality. The integration of additional functionality is accurately described by the solid state transformer [18]. The solid state transformer (SST) is a system that may be used to integrate distributed renewable energy resources (DRERs) and distributed energy storage devices (DESDs) into the power grid and form an island should the utility power system encounter an interruption in service. The SST is smaller and more flexible than traditional core-type transformers by providing power factor correction (PFC), current limiting, power source and sink capability, DC output, AC output, and voltage regulation. As described, the solid state transformer provides a greater degree of functionality compared to a traditional DC-to-AC inverter. One should note, however, that the model used to describe the behavior of the SST when connected to other voltage sources is applicable to both SSTs and inverters. Therefore, the terms “SST” and “inverter” are used interchangeably where appropriate. An average model of the SST used in the FREEDM Green Hub [18] is shown in Figure 1.1.

It can be seen that this SST has three stages that interface the power grid, renewable sources, and an individual users load. With bi-directional power flow, flexible system structure, and uncertain operating conditions, controlling the SSTs is a critical and challenging issue. While there are a variety of control schemes, they may be grouped into

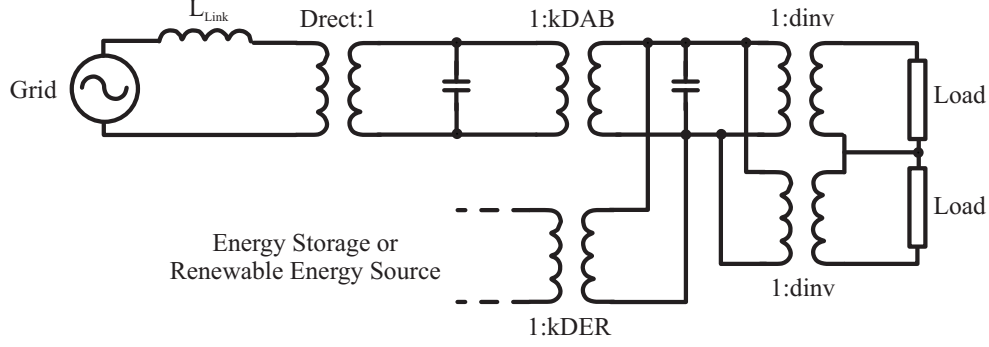


Figure 1.1: Average model of a solid state transformer.

two broad categories, centralized and decentralized. Centralized control relies on communications from and to each SST by a central controller that issues command signals to each SST in a given microgrid. While a variety of algorithms and implementation strategies exist, a central issue with this approach is that it is not robust. If the centralized controller fails or any of the communications links fail, the entire system may fail. Conversely, decentralized control relies only on local measurements. The decentralized approach makes the system self healing, this is to say that it can adapt to any number of configuration changes, and is therefore much more robust. The primary concerns with decentralized control are maintaining system stability over a wide operating range and limiting voltage and frequency excursions for perturbations in the system. While a variety of variations exist for decentralized control [35], [34], [29], [30], [21], [44], [43], [48], the two most fundamental approaches will be explored in this report.

1.3 Problem definition, research objectives, and contributions.

Traditional droop control uses a constant gain droop control (CGDC) schedule (k_p and k_v), as given in (1.1) and (1.2) and implemented in a SST as shown in Figure 1.2.

$$\omega = \omega_0 - k_p \Delta P \quad (1.1)$$

$$V = V_0 - k_v \Delta Q \quad (1.2)$$

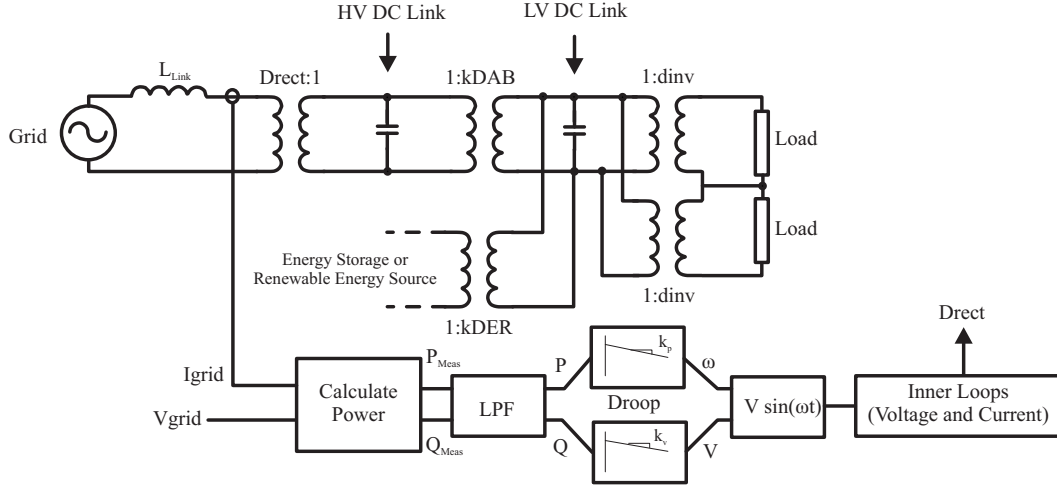


Figure 1.2: High level diagram of SST with droop control.

Such schemes have restricted operating range and may become unstable or exhibit poor performance if operated outside of a given range of loads [28], [47], [6].

Droop control issues a sinusoidal reference and requires additional feedback to track the desired value. Typically two loop, current mode control (CMC) as shown in Figure 1.3, is used to track the droop voltage or other synchronized voltage. While CMC controllers are typically designed considering one loop at a time, this approach has been shown to be unreliable. A classic example is the spinning satellite problem in which a two loop system is shown to have 90° phase margin and infinite gain margin in each loop, but is unstable for very small simultaneous perturbations [49]. Such problems are addressed using the tools of robust control [49].

The purpose of this report is the following:

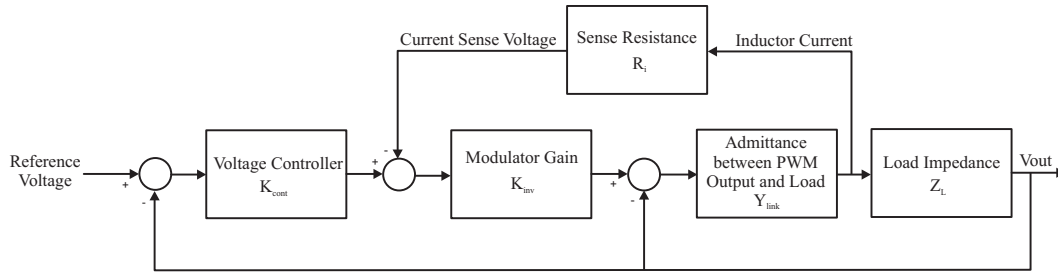


Figure 1.3: Two loop (current mode) control with inductor current and output voltage feed-back.

- Review prior analysis and control methods with a focus on constant gain droop control (CGDC).
- Present a new analytical model that is conducive to robust controller design.
- Synthesize a robust controller using Glover McFarlane loopshaping (GMFDC).
- Analyze the system using the gap metric.
- Compare the CGDC and GMFDC methods using hardware.
- Model the system using polytopic and affine representations.
- Design a gain scheduled GMFDC.
- Design a set of bumpless GMFDC.
- Compare the gain scheduled GMFDC, bumpless GMFDC, GMFDC, and CGDC in simulation

Through this work it will become apparent that the new approach to modeling and control provides a simpler framework for design, superior robustness, and superior performance when compared to CGDC that is typically used.

1.4 Survey of Microgrid Control

In this section a survey of prior approaches to microgrid control will be given. These approaches include droop, master-slave, and current mode control, which will be presented with typical variations.

Droop Control

Droop control is perhaps the most common distributed control method used in microgrids. One may think of droop control as “setpoint control” where the voltage magnitude and frequency setpoints change with reactive and active power¹. The applicability of droop control is readily apparent by considering the relationships that dictate the power transfer in a two inverter system as shown in Figure 1.4.

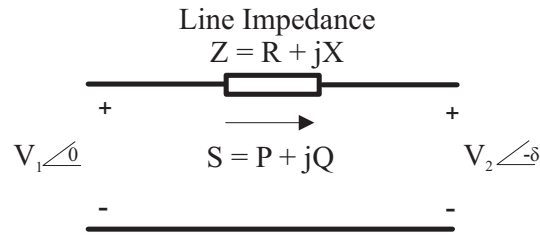


Figure 1.4: A system with two voltage sources. Note that the variable “S” denotes complex power transfer between the two sources.

The fundamental relationships relating system voltage and phase to active and reactive power are given as (1.3) and (1.4).

$$V_2 \sin(\delta) = \frac{XP - RQ}{V_1} \quad (1.3)$$

$$V_1 - V_2 \cos(\delta) = \frac{RP + XQ}{V_1} \quad (1.4)$$

¹The control variables are dictated by the line impedance and will be discussed in detail later in this section.

If one assumes $X \gg R$ and $\delta \ll 1$, the relationships may be simplified to (1.5) and (1.6). From these relationships one may observe a direct relationship between phase and active power and voltage and reactive power.

$$\delta \simeq \frac{XP}{V_1 V_2} \quad (1.5)$$

$$V_1 - V_2 \simeq \frac{XQ}{V_1} \quad (1.6)$$

Alternatively, if one assumes $R \gg X$ and $\delta \ll 1$, the relationships may be simplified to (1.7) and (1.8). From these relationships one may observe a direct relationship between voltage and active power and phase and reactive power.

$$\delta \simeq -\frac{RQ}{V_1 V_2} \quad (1.7)$$

$$V_1 - V_2 \simeq \frac{RP}{V_1} \quad (1.8)$$

Conventional droop control is based on several assumptions such as the output impedance having negligible effect on the power characteristic (output impedance is small compared to line impedance) and there is no cross coupling in the $P - \omega$ or $Q - V$ relationships. It is clear, however, that the assumptions made can significantly influence the appropriate control law. One way these issues are addressed is by applying a linear rotational transformation matrix and modifying the control law [16]. The linear rotational transformation is applied as (1.9).

$$\begin{pmatrix} P' \\ Q' \end{pmatrix} = \begin{pmatrix} \sin(\theta) & -\cos(\theta) \\ \cos(\theta) & \sin(\theta) \end{pmatrix} \begin{pmatrix} P \\ Q \end{pmatrix} \quad (1.9)$$

Where the angle of the complex line impedance is defined in (1.10) and X, R are the line reactance and resistance respectively.

$$\theta = \tan^{-1}(X/R) \quad (1.10)$$

The transformed power quantities P' and Q' , are then used in the power relationships (1.11) and (1.12).

$$\delta \simeq \frac{ZP'}{V_1 V_2} \quad (1.11)$$

$$V_1 - V_2 \cos(\delta) \simeq \frac{ZQ'}{V_1} \quad (1.12)$$

For $\delta \ll 1$ the droop control laws may be expressed as (1.13) and (1.14).

$$\omega - \omega_0 = -k_p(P' - P'_0) \quad (1.13)$$

$$V - V_0 = -k_v(Q' - Q'_0) \quad (1.14)$$

At some point, the reader may question why the the power transfer relation is expressed in terms of *phase* and voltage differences, but droop relies on *frequency* and voltage differences to transfer power. The answer lies in the fact that the frequency difference will periodically change by a small amount. The wandering droop frequency results in a constant phase difference that is necessary to transfer power. The droop frequency for a constant phase difference may be found by solving (1.15). For an inverter delivering 15 kW to a load, the frequency deviation is typically less than 0.2 rad/s (0.05 % deviation from nominal 377 rad/s signal).

$$\phi = (\omega_0 - \omega)t \mod 2\pi \quad (1.15)$$

One should be aware of the fact that there are certain fundamental limitations on the power that may be transferred between two systems. The equations (1.16) and (1.17) are plotted in Figure 1.5.

$$P = \frac{V_2}{Z} [(V_1 \cos(\delta) - V_2) \cos(\theta) + V_1 \sin(\theta) \sin(\delta)] \quad (1.16)$$

$$Q = \frac{V_2}{Z} [(V_1 \cos(\delta) - V_2) \sin(\theta) + V_1 \cos(\theta) \sin(\delta)] \quad (1.17)$$

Where $\theta = \tan^{-1}(X/R)$ is the angle of the complex line impedance.

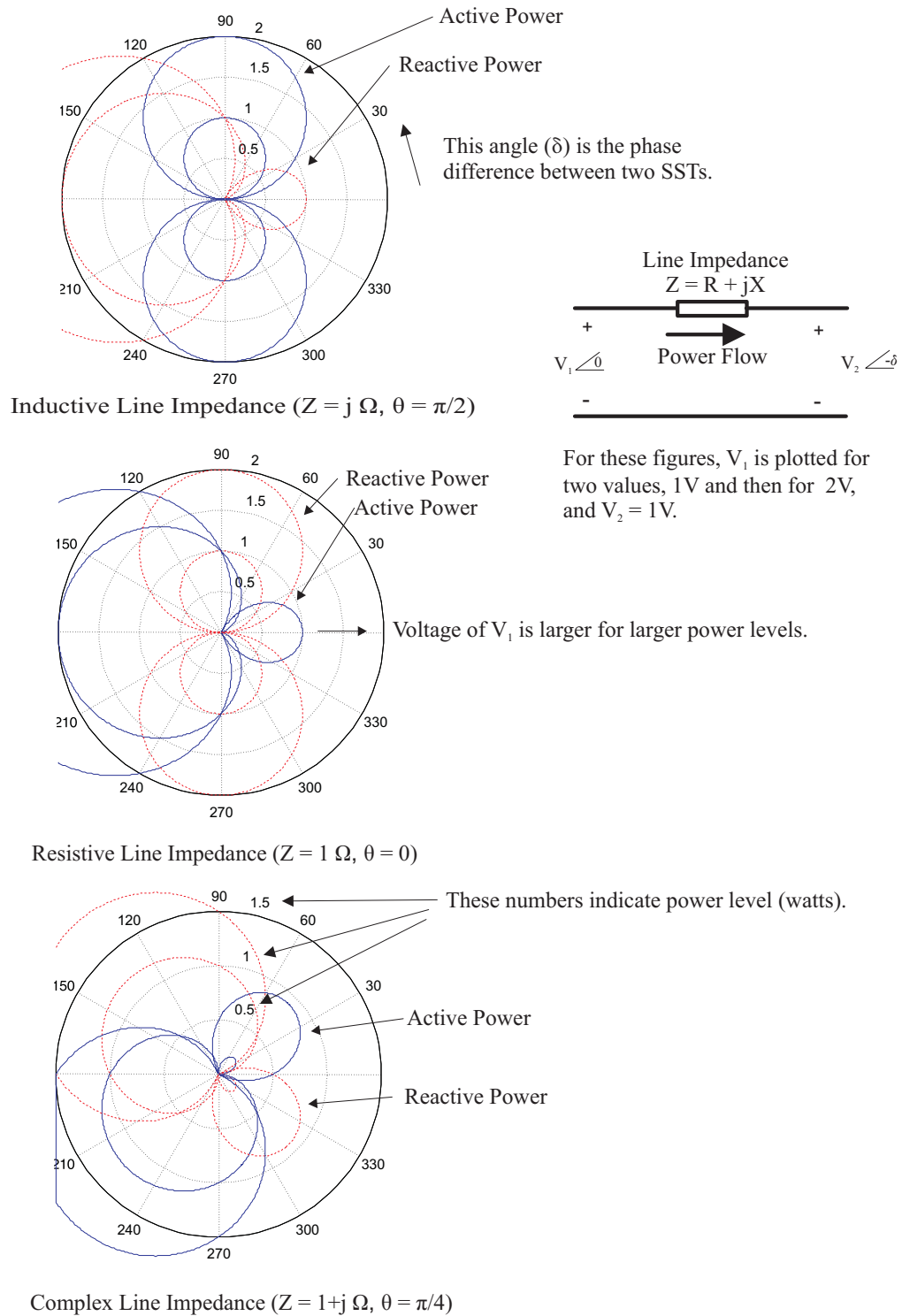


Figure 1.5: Power transferred between two inverters. Please refer to equations (1.16) and (1.17).

Most inverters operating with droop control will have an inductive filter (inductor in series with inverter output and microgrid). The primary purpose of the inductor is to filter the switching frequency components from the output². The impedance of the inductor is typically small enough that low order harmonics ($k\omega$, $k = 2, 3, \dots$, and ω is the line frequency) result in harmonic currents (1.18).

$$I_k = \frac{V_k - V_{INV}}{j\omega \cdot L_{Link}} \quad (1.18)$$

Where V_k and I_k are the k^{th} harmonic of the grid voltage and harmonic current respectively.

One solution to such problems is to increase the output impedance at harmonic frequencies. This is done by lowering the output voltage at harmonic frequencies in proportion to harmonic currents, this is to say lower V_k/I_k , k in the integers as shown in Figure 1.6. This functionality may be combined with the voltage feed-forward as shown in Figure 1.6. Other issues encountered with traditional droop control are slow phase response time and poor damping. These issues are addressed using phase feedforward which lowers the transient time of the phase response since the feed-forward path is in parallel with an integrator [49], [36], [21], and impedance feed-forward which lowers the output voltage in proportion to the output current. This increases the apparent output resistance and therefore increases damping in the system.

²The inductor may also be used to limit the inrush current to the microgrid should a fault occur.

Master-Slave Control

Conventional master-slave control may be considered a hybrid of centralized and decentralized control as shown in Figure 1.7. The master inverter utilizes droop control to set the voltage and frequency setpoints of the bus. The master inverter communicates with the slave inverters via a current calculator which generates reference currents so that the master and slave inverters share the appropriate load currents. The centralized computation of command signals and single loop control used in slave inverters simplify control design in a microgrid. The disadvantage of the master-slave control method is that it relies on calculating current references and communicating with all the slave inverters. This critical calculation and communications link make the master-slave approach less reliable than a system using inverters with droop control only.

There are a variety of modifications that can be made to the conventional master-slave approach [39]. Modifications to the conventional approach include allowing one of the slaves to become the master if the master or its controller should fail. Such selection may be made according to a rotating priority [46] or power capacity [45]. These approaches are not considered in detail as they all suffer from greater complexity and lower redundancy when compared to a purely decentralized approach.

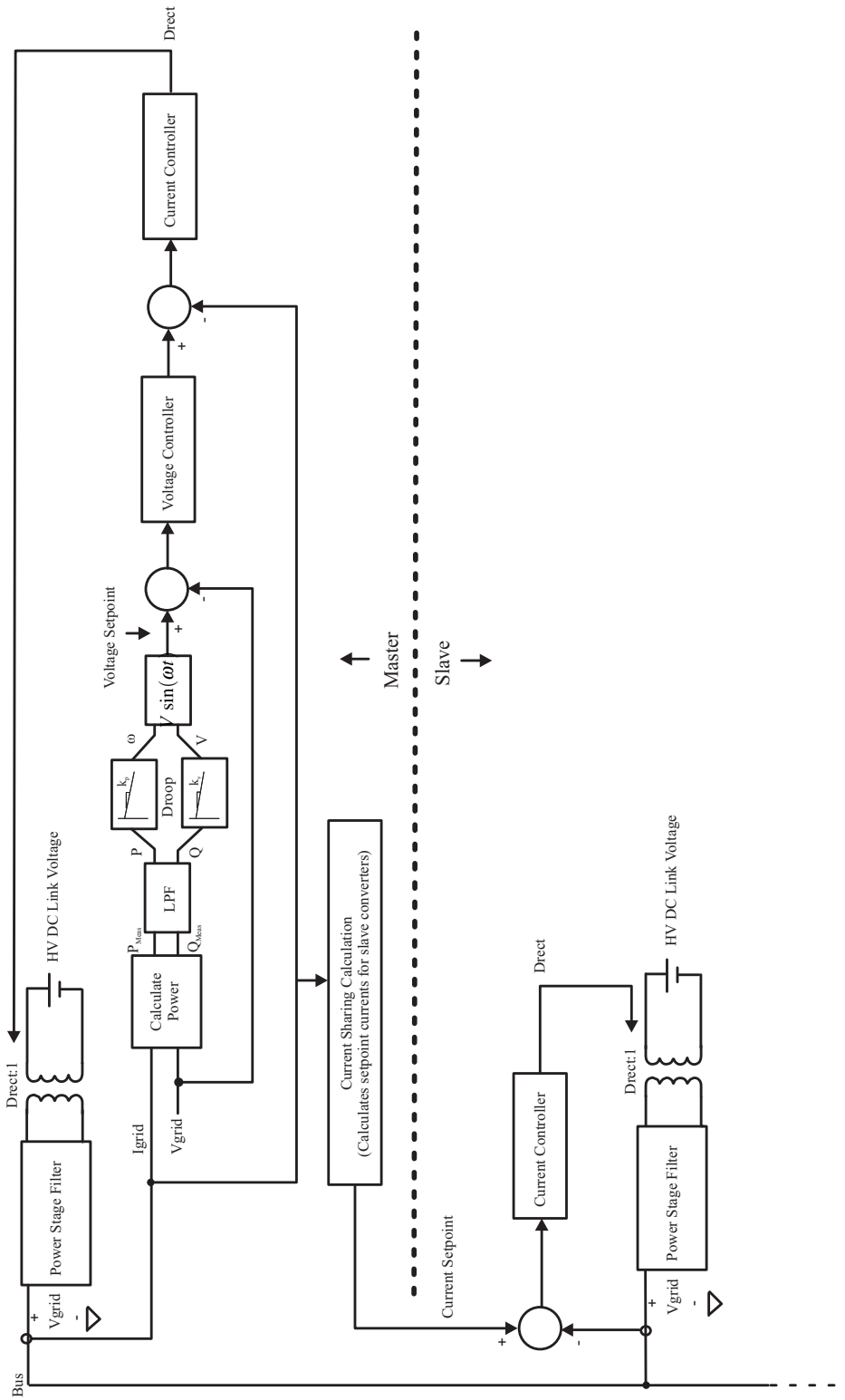


Figure 1.7: Master-slave control for a system of two inverters.

Current Mode Control

Current mode control, as shown in Figure 1.8, is typically used to track the setpoint derived from droop or other control approaches. Upon inspection of this control approach, one will note that both loops have finite gain, the inner (current) loop will act as a disturbance that introduces a voltage and phase offset proportional to load current. A result of the noted loop behavior is that changes in the load impedance will change the system transfer function, thereby changing the amplitude and phase at a given frequency. This is apparent from the system transfer function expressed in (1.19).

$$T = \frac{Z_L \cdot Y_{\text{link}} \cdot K_{\text{inv}} \cdot K_{\text{cont}}}{Z_L \cdot Y_{\text{link}} \cdot K_{\text{inv}} \cdot K_{\text{cont}} + Y_{\text{link}} \cdot K_{\text{inv}} \cdot R_i + Z_L \cdot Y_{\text{link}} + 1} \quad (1.19)$$

A simple example illustrates the validity of the approach. Let us assume the following parameter values $K_{\text{inv}} = 11800 \text{ V/V}$, $R_i = 1.8 \Omega$, $s = j377 \text{ rad/s}$, $Y_{\text{link}} = 1/(0.4s + 2)$, $K_{\text{cont}} = 1/(s + 0.001)$. A load impedance of $Z_L = 5000 \Omega$ results in a transfer function magnitude and phase of 0.987 V/V and -0.000882° respectively. If the load is changed to $Z_L = j5000 \Omega$, the associated transfer function magnitude and phase are 0.88 V/V and 0.000154° respectively. This change in response is consistent with the desired response for systems with lines dominated by inductive reactance (see equations (1.5) and (1.6)). Note that this approach can only accommodate small phase differences between any given source. As a result of this, all sources must have a common reference or use droop control to generate an appropriate setpoint.

Current mode control has been shown to have better dynamic response and tracking compared to the basic droop approach [29]. Current mode control also has inherent line feed-forward, current limit, and has been successfully used as the control strategy in parallel inverters. Two fundamental issues with nested control loops are instability due to simultaneous perturbations and uncertainty. Both of these issues are

addressed by designing a μ -controller which can be used to guarantee robust stability over all specified values of uncertainty [49]. Since uncertainty bounds may be specified for μ -controllers, one may specify the load as an uncertainty. The resulting controller would allow one to use the inverter as long as the load is within the specified range.

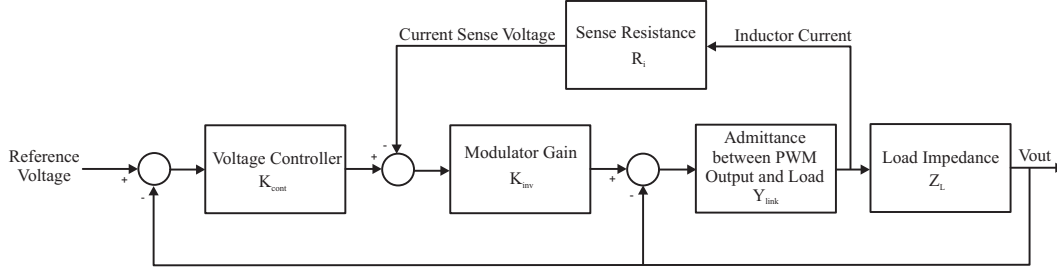


Figure 1.8: Two loop (current mode) control with inductor feedback.

At some point the reader may begin to consider the current sharing ability of inverters with CMC. One such system is shown in Figure 1.9. The difference in currents, also referred to as circulating current, may be expressed as in (1.20) and (1.21). If one considers these equations and the impedance “seen” by each inverter³, it becomes apparent that the difference in line impedances plays an important role in current sharing. At this point one may begin to consider the output impedance of each inverter. The output impedance of an inverter is typically ignored and all that is considered in a given analysis is the line impedance. One may, however, consider the output impedance to be in series with the impedances and represented as Z_1 and Z_2 as shown in Figure 1.9. One will note that if the output impedance is much larger than the line impedance, current sharing will improve.

$$\Re(I_1 - I_2) = \frac{V_1 R_1 \cos(\delta_1) + V_1 \omega L_1 \sin(\delta_1) - V_L R_1}{R_1^2 + (\omega L_1)^2} - \frac{V_2 R_2 \cos(\delta_2) + V_2 \omega L_2 \sin(\delta_2) - V_L R_2}{R_2^2 + (\omega L_2)^2} \quad (1.20)$$

³ Assume the inverters are identical.

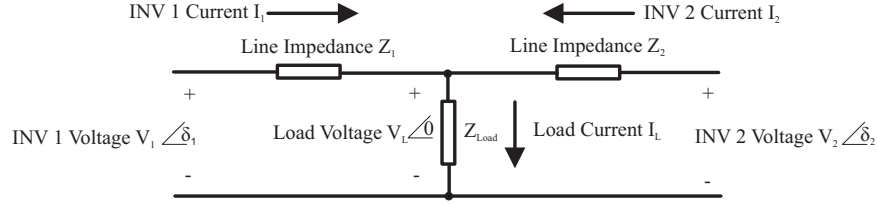


Figure 1.9: Current sharing with two inverters.

$$\begin{aligned} \Im(I_1 - I_2) = & \frac{V_1 R_1 \sin(\delta_1) + V_1 \omega L_1 \cos(\delta_1) - V_L R_1}{R_1^2 + (\omega L_1)^2} \\ & - \frac{V_2 R_2 \sin(\delta_2) + V_2 \omega L_2 \cos(\delta_2) - V_L R_2}{R_2^2 + (\omega L_2)^2} \end{aligned} \quad (1.21)$$

One proposed strategy to improve current sharing has been proposed [58] and is shown in Figure 1.10. Using this approach, $R_1 \approx R_2$, $L_1 \approx L_2$, and $\delta \approx 0$, and the current sharing equations may be approximated as in (1.22) and (1.23) where R_{nom} and L_{nom} are the sum of the nominal transmission line and output impedance parameters. From these expressions, it is easy to see that the circulating current will be determined by the difference in output voltages which are small if a common reference is used⁴.

$$\Re(I_1 - I_2) \simeq \frac{R_{\text{nom}}(V_1 - V_2)}{R_{\text{nom}}^2 + (\omega L_{\text{nom}})^2} \quad (1.22)$$

$$\Im(I_1 - I_2) \simeq \frac{\omega L_{\text{nom}}(V_2 - V_1)}{R_{\text{nom}}^2 + (\omega L_{\text{nom}})^2} \quad (1.23)$$

⁴The common reference may be a centralized setpoint or generated by droop (ie “setpoint”) control with common droop schedules.

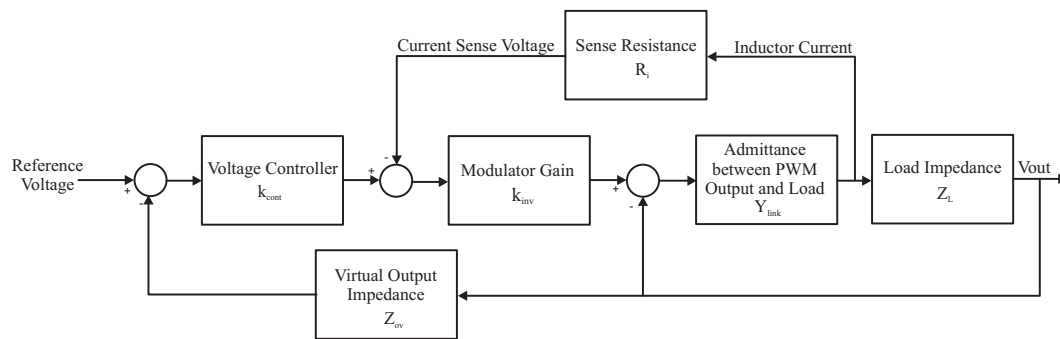


Figure 1.10: CMC with modified output impedance.

Chapter 2

ANALYTICAL SYSTEM MODELS

This chapter begins with a review of the standard modeling approach for CGDC as developed by Coelho [14] (section 2.1). While this model provides an excellent starting point, the model represents a specific system structure operating at a specific operating point. As such it is quite restrictive. A model developed by Iyer [28] is presented in section 2.2. This model is more general than Coelho's model, but is limited to CGDC. A new model was developed as part of this research and is presented in section 2.3 which may be used for any control structure, system configuration, and is particularly well suited to robust control design.

2.1 Model Derivation for Voltage Sources with Constant Gain Droop Control

Modeling voltage sources with droop control is the same whether they are inverters, SST, or otherwise. To illustrate this concept, the simplification process for a SST is shown graphically in Figure 2.1¹.

The system interconnection at the top of the figure simply illustrates the average model of an SST in grid connected mode. The system representation in the middle of the figure does not consider the effect of the DAB or low voltage load. The figure at the bottom of the page assumes that the voltage and control loops have a bandwidth much greater than the LPF and have a gain of approximately 1 for frequencies less than the bandwidth of the LPF. After performing this series of approximations, it becomes apparent that the behavior of the parallel connection of the grid-SST (grid-inverter) or an arbitrary number of SSTs (inverters) are analogous to the parallel connection of an arbitrary number of synchronous machines [14]. A general analytical analysis proceeds as the following:

¹One should note that while the figure shows a single grid-connected SST, the approach is applicable to an arbitrary number of parallel-connected SSTs.

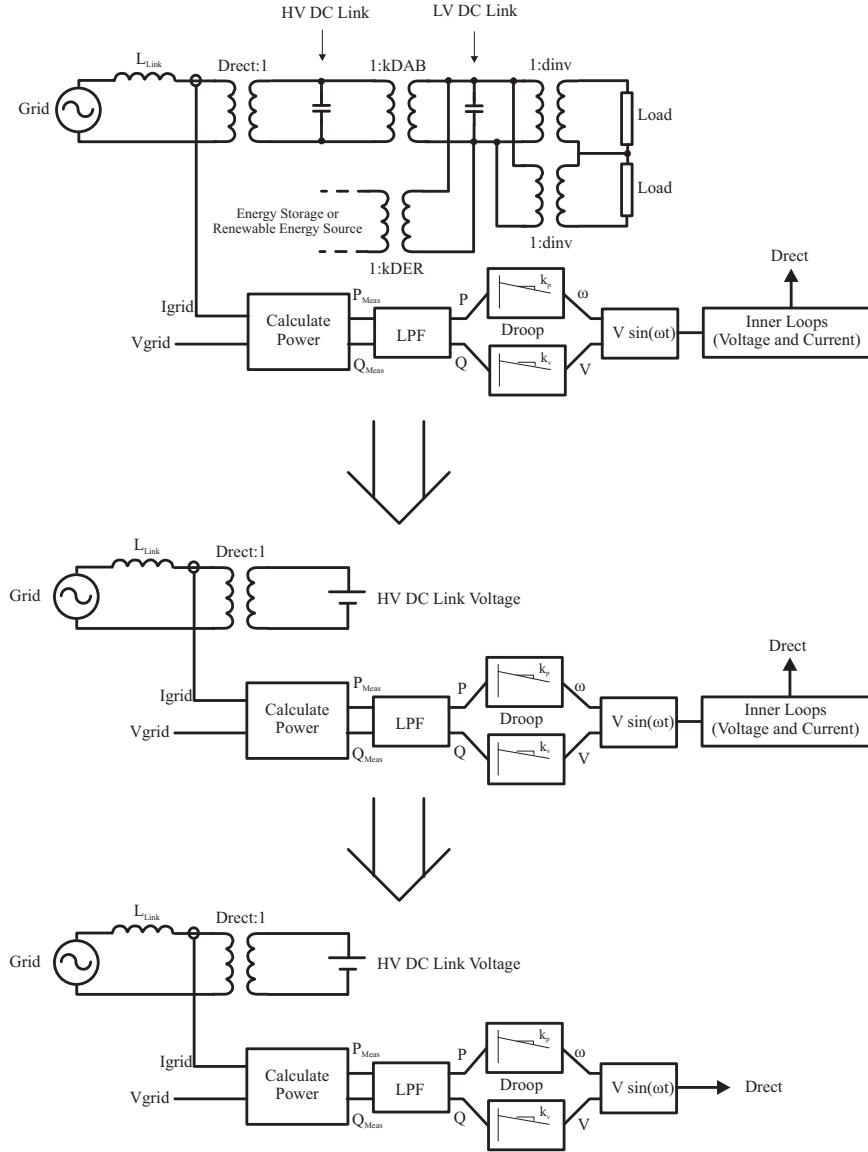


Figure 2.1: Sequence of approximations used to model the SST.

Given the standard droop equations (2.1), (2.2):

$$\omega = \omega_0 - k_p \Delta P \quad (2.1)$$

$$V = V_0 - k_v \Delta Q \quad (2.2)$$

The output of the LPF is represented analytically as (2.3), (2.4):

$$\Delta P(s) = \frac{\omega_f}{s + \omega_f} \Delta P_{meas}(s) \quad (2.3)$$

$$\Delta Q(s) = \frac{\omega_f}{s + \omega_f} \Delta Q_{meas}(s) \quad (2.4)$$

Making use of the droop equations and the LPF transfer relationships, the change in voltage and frequency in the frequency domain are expressed as (2.5), (2.6):

$$\Delta \omega(s) = -\frac{k_p \omega_f}{s + \omega_f} \Delta P_{meas}(s) \quad (2.5)$$

$$\Delta V(s) = -\frac{k_v \omega_f}{s + \omega_f} \Delta Q_{meas}(s) \quad (2.6)$$

In the time domain (2.5) and (2.6) are expressed as (2.7), (2.8):

$$\Delta \dot{\omega} = -\omega_f \Delta \omega - k_p \omega_f \Delta P_{meas} \quad (2.7)$$

$$\Delta \dot{V} = -\omega_f \Delta V - k_v \omega_f \Delta Q_{meas} \quad (2.8)$$

The output voltage of the inverter in the dq-frame is defined as (2.9) with angle defined as (2.10):

$$\vec{V} = v_d + jv_q \quad (2.9)$$

$$\delta = \tan^{-1}(v_q/v_d) \quad (2.10)$$

Linearizing (2.10) results in (2.11):

$$\Delta\delta = \frac{\partial\delta}{\partial v_d}\Delta v_d + \frac{\partial\delta}{\partial v_q}\Delta v_q \quad (2.11)$$

Considering (2.10), it follows that the phase relation is given as (2.12):

$$\Delta\delta = m_d\Delta v_d + m_q\Delta v_q \quad (2.12)$$

Where:

$$m_d = \frac{-v_q}{v_d^2 + v_q^2} \quad (2.13)$$

$$m_q = \frac{v_d}{v_d^2 + v_q^2} \quad (2.14)$$

Since frequency is the time derivative of phase, $\Delta\omega(s) = s\Delta\delta(s)$, the result (2.15) follows:

$$\Delta\omega = m_d\Delta\dot{v}_d + m_q\Delta\dot{v}_q \quad (2.15)$$

Given that $V = |\vec{V}| = \sqrt{v_d^2 + v_q^2}$, ΔV may be expressed as (2.16):

$$\Delta V = n_d\Delta v_d + n_q\Delta v_q \quad (2.16)$$

Where:

$$n_d = \frac{v_d}{v_d^2 + v_q^2} \quad (2.17)$$

$$n_q = \frac{v_q}{v_d^2 + v_q^2} \quad (2.18)$$

Therefore:

$$\Delta\dot{V} = \frac{v_d}{\sqrt{v_d^2 + v_q^2}}\Delta\dot{v}_d + \frac{v_q}{\sqrt{v_d^2 + v_q^2}}\Delta\dot{v}_q \quad (2.19)$$

One may then solve for $\Delta\dot{\omega}$, $\Delta\dot{v}_d$, and $\Delta\dot{v}_q$ as given in (2.20):

$$\begin{aligned} \Delta\dot{\omega} &= -\omega_f\Delta\omega - k_p\omega_f\Delta P_{meas} \\ \Delta\dot{v}_d &= \frac{n_q}{m_d n_q - m_q n_d}\Delta\omega + \frac{m_q n_d \omega_f}{m_d n_q - m_q n_d}\Delta v_d \\ &\quad + \frac{m_q n_q \omega_f}{m_d n_q - m_q n_d}\Delta v_q + \frac{k_v m_q \omega_f}{m_d n_q - m_q n_d}\Delta Q_{meas} \\ \Delta\dot{v}_q &= \frac{n_d}{m_q n_d - m_d n_q}\Delta\omega + \frac{m_d n_d \omega_f}{m_q n_d - m_d n_q}\Delta v_d \\ &\quad + \frac{m_d n_q \omega_f}{m_q n_d - m_d n_q}\Delta v_q + \frac{k_v m_d \omega_f}{m_q n_d - m_d n_q}\Delta Q_{meas} \end{aligned} \quad (2.20)$$

Equations (2.20) are given in matrix form for each inverter “k” as shown in (2.21):

$$\begin{pmatrix} \Delta\dot{\omega}_k \\ \Delta\dot{v}_{dk} \\ \Delta\dot{v}_{qk} \end{pmatrix} = (M_k) \begin{pmatrix} \Delta\omega_k \\ \Delta v_{dk} \\ \Delta v_{qk} \end{pmatrix} + (C_k) \begin{pmatrix} \Delta P_{meas_k} \\ \Delta Q_{meas_k} \end{pmatrix} \quad (2.21)$$

The remaining analysis consists of solving for the interconnection matrix and making the appropriate substitutions. The analysis here proceeds in general terms which may be easily extended to specific cases.

Given that the matrix of admittances relating the inverter voltages (v_{d1} , v_{q1} , v_{d2} , v_{q2} , etc) to inverter currents (i_{d1} , i_{q1} , i_{d2} , i_{q2} , etc) is given simply by the variable “Y”. The following relation (2.22) is given:

$$(\Delta i) = (Y)(\Delta v) \quad (2.22)$$

The relationship expressing inverter power is given as (2.23):

$$(\Delta S) = (i)(\Delta v) + (v)(\Delta i) \quad (2.23)$$

Using (2.22), equation (2.23) may be simplified and expressed as (2.24):

$$(\Delta S) = ((i) + (v)(Y))(\Delta v) \quad (2.24)$$

The relationship between complex power and voltage as given in (2.24) may be substituted into (2.21) with (2.25) as the result:

$$(\Delta \dot{x}) = (M)(\Delta x) + (c)((i) + (v)(Y))(\Delta v) \quad (2.25)$$

In order to further simplify (2.25), it is necessary to express Δv in terms of Δx . Since changes in voltage are contained within the state variables, there is a clear truncation in state variables as given by (2.26):

$$\begin{pmatrix} v_d \\ v_q \end{pmatrix} = K \begin{pmatrix} \Delta \omega \\ \Delta v_d \\ \Delta v_q \end{pmatrix} \quad (2.26)$$

Where:

$$K = \begin{pmatrix} 0 & 1 & 0 \\ 0 & 0 & 1 \end{pmatrix} \quad (2.27)$$

Therefore, the system response is given by (2.28):

$$\Delta \dot{x} = \{M + (c)[(i) + (v)(Y)](K)\}(\Delta x) \quad (2.28)$$

This result allows one to analyze the system in a variety of ways, the most popular being the root locus plot (eigenvalues as a function of a given parameter), and the state transition matrix.

Recent modeling work has revisited the traditional approach developed by Coelho and made use of dynamic phasors [57], [14]. The purpose of the extension is to include higher order dynamics that improve the accuracy of the model. While this approach may improve the model accuracy, the improvement is negligible and only impacts stability for examples with an unreasonably large droop gain.

2.2 A Generalized Model for Converters with Constant Gain Droop Control

The generalized microgrid model developed by Iyer [28] is given for any converter in a microgrid as (2.29).

$$P_{cl} = \left(s + k_{pm} \left(-Q_m + \sum_n \frac{\omega L_{mn}}{|Z_{mn}|^2} \right) \right) \left(1 + k_{vm} \left(Q_m + \sum_n \frac{\omega L_{mn}}{|Z_{mn}|^2} \right) \right) \quad (2.29)$$

Where “n” denotes the set of microgrid connections made by inverter “m”.

After considering (2.29), one will note two significant implications of the model. These implications are the ability to estimate the stability of any given inverter in a

microgrid by analyzing only one polynomial, and the effect of line impedance on stability. While one may modify the output impedance as a function of line impedance and output power, an initial investigation was made considering only the line impedance. The necessary virtual output impedance was derived as shown in Figure 2.2 and implemented as shown in Figure 2.3. As a test case, a system with parameters given in Table 2.1. The necessary output impedance was derived from the experimental results in Figure 2.4. The transient response without and with the output impedance modification are shown in Figure 2.5 and Figure 2.6 respectively.

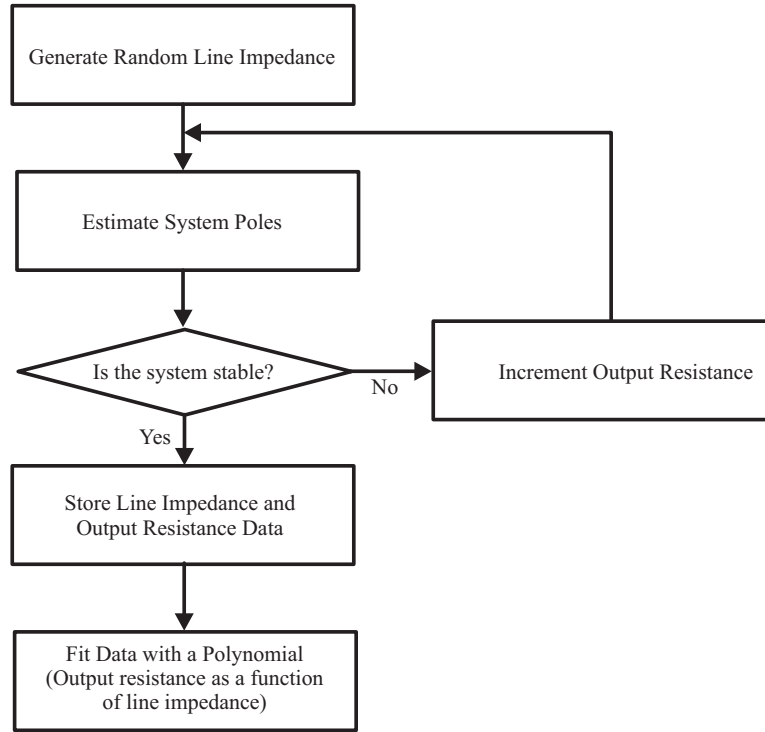


Figure 2.2: Flowchart illustrating how the virtual output impedance is derived.

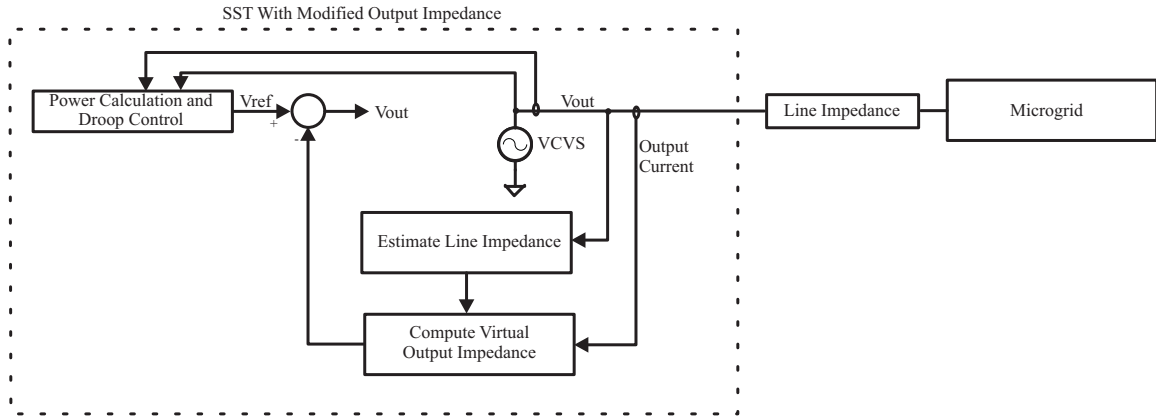


Figure 2.3: Block diagram illustrating how the virtual output impedance is implemented.

Table 2.1: Parameters used in the system where one inverter has virtual output impedance control.

Parameter	Value
V_{INV}	$180 V_{peak}$
ω_{INV}	380 rad/s
V_{PCC}	$170 V_{peak}$
ω_{PCC}	377 rad/s
Z_{Line}	$0.005 + j 0.1 \Omega$
k_p	10^{-4} rad/s/w
k_v	10^{-4} V/VA

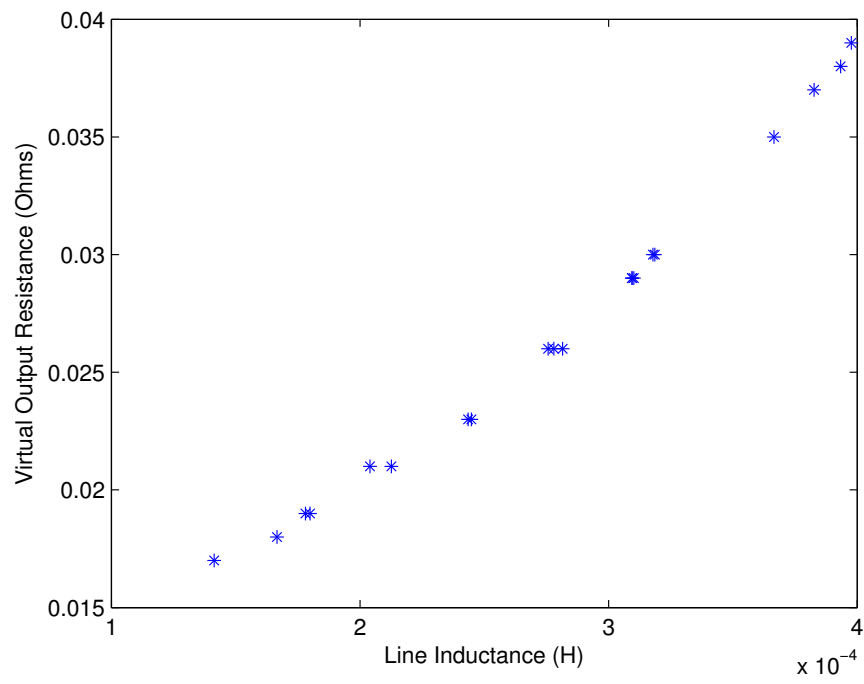


Figure 2.4: Virtual output resistance necessary to ensure inverter stability.

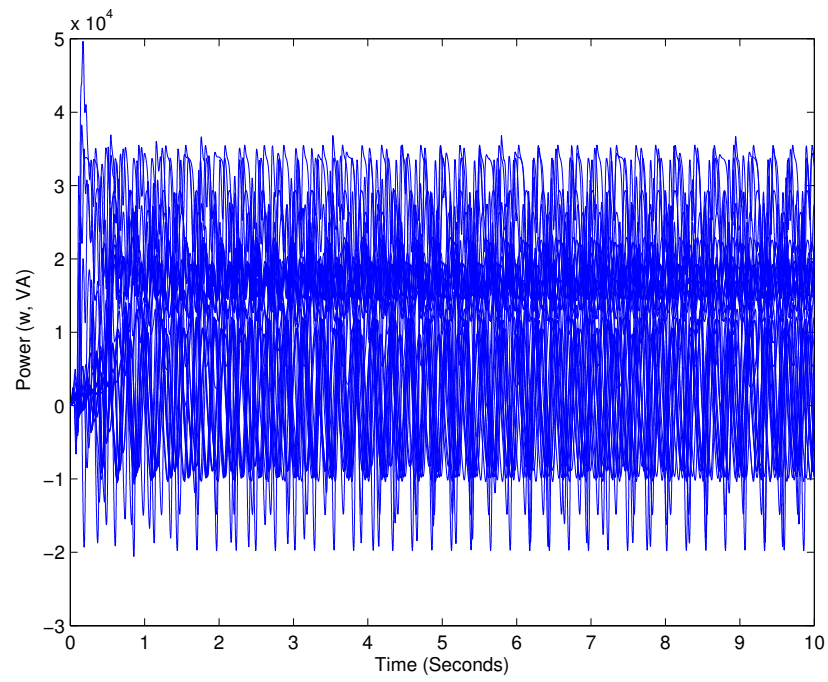


Figure 2.5: Transient response of inverter without output impedance control.

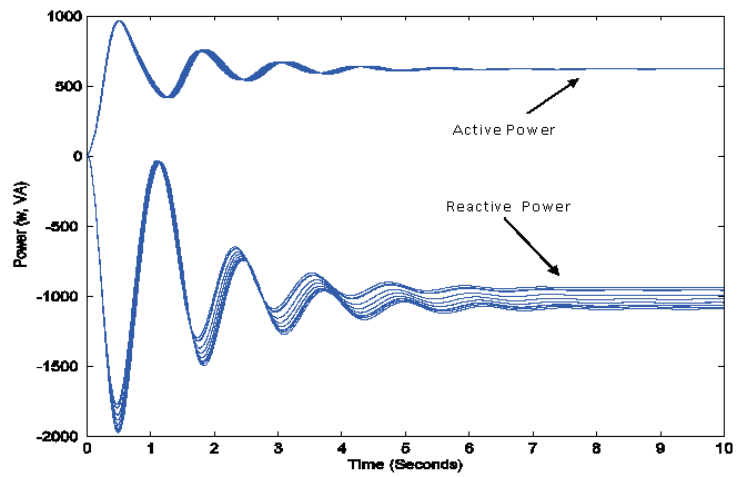


Figure 2.6: Transient response of inverter with output impedance control.

2.3 A General Linear Model for Robust Controller Design

The modeling approaches presented in the previous sub-sections all suffer from an inability to accommodate changing network configurations and are not conducive to robust controller design. Addressing these issues requires a fundamental paradigm shift in which an inverter connected to the remainder of a microgrid is modeled using the Thevenin equivalent for the remainder of the microgrid². Modeling the network in this way dismisses the traditional perspective of grid-connected or islanded mode, and simply considers one mode with a range of parameters. Such a perspective facilitates the design of a “plug-and-play” inverter using the techniques of robust control systems [49]. The idea of modeling the power grid using its Thevenin equivalent circuit was presented in [54], however the model derived is a closed loop characteristic equation that does not include the filter dynamics used to average inverter output power. The open loop MIMO transfer function for an inverter connected to the remainder of a microgrid will be derived in this section.

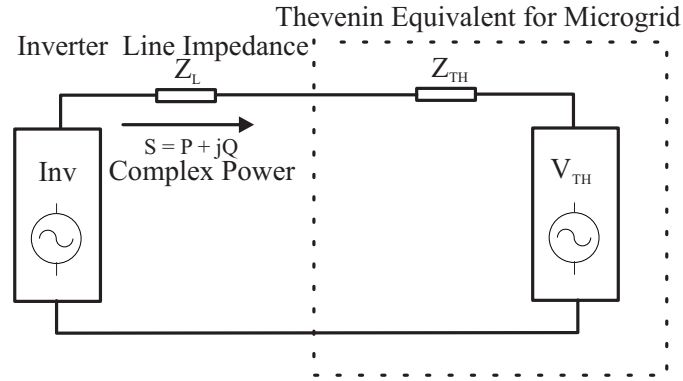


Figure 2.7: Inverter connected to Thevenin equivalent of the microgrid.

The linearized equations for the system in Figure 2.7 are easily derived using the

²The same modeling and control theory applies to inverters and SSTs. The terms “inverter” and “SST” are therefore used interchangeably in this report.

fundamental power expressions (2.30) and (2.31) (see Figure 2.8), where the voltages are the peak instantaneous values, the power is the average value, and δ is the phase difference between the two sources.

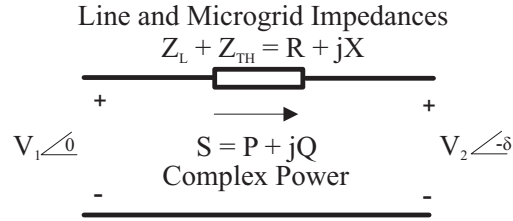


Figure 2.8: Two inverter system.

After isolating the active and reactive power, P and Q , the first order Taylor series expansion is given as (2.32) and (2.33) [52].

$$V_2 \sin(\delta) = \frac{XP - RQ}{2V_1} \quad (2.30)$$

$$V_1 - V_2 \cos(\delta) = \frac{RP + XQ}{2V_1} \quad (2.31)$$

$$P(V_1, \delta) \approx P_0 + \frac{\partial P}{\partial \delta} \Delta \delta + \frac{\partial P}{\partial V_1} \Delta V_1 \quad (2.32)$$

$$Q(V_1, \delta) \approx Q_0 + \frac{\partial Q}{\partial \delta} \Delta \delta + \frac{\partial Q}{\partial V_1} \Delta V_1 \quad (2.33)$$

$$\frac{\delta}{\omega} = \frac{1}{s} \quad (2.34)$$

Taking the Laplace transform of (2.32) and (2.33), and given the relationship between phase and frequency in (2.34), the open loop expressions may be expressed as (2.35) where θ is the angle of the complex line and Thevenin impedances as shown in Figure 2.7. This model may then be cascaded with the low pass filter used in the power calculation block [14].

$$\begin{pmatrix} \Delta P(s) \\ \Delta Q(s) \end{pmatrix} \approx \begin{pmatrix} \frac{V_2(-V_1 \cos(\theta) \sin(\delta) + V_1 \sin(\theta) \cos(\delta))}{2Zs} & \frac{V_2(\cos(\delta) \cos(\theta) + \sin(\theta) \sin(\delta))}{2Z} \\ \frac{V_2(-V_1 \sin(\theta) \sin(\delta) - V_1 \cos(\theta) \cos(\delta))}{2Zs} & \frac{V_2(\cos(\delta) \sin(\theta) - \cos(\theta) \sin(\delta))}{2Z} \end{pmatrix} \begin{pmatrix} \Delta \omega \\ \Delta V \end{pmatrix} \quad (2.35)$$

One will note that there will always be some degree of coupling between any given inverter and the rest of the system, particularly in weak microgrids. This is to say that there will be interplay between the sources V_1 and V_2 in Figure 2.8. For practical systems this interplay may not be described by a simple relationship and is generally unknown. Having run a wide range of simulations, the effect of coupling has been negligible and is not considered here.

Model Validation

The system configuration used to validate the model is shown in Figure 2.9. The open loop inverter is modeled as a voltage source operating at the setpoint given in Table 2.2. The closed loop inverter uses the standard droop implementation as shown in Figure 2.10, operating under the conditions given in Table 2.3, with loop gain shown in Figure 2.11. The maximum perturbations used for comparing the open loop models were limited to 1 rad/s and 10V. These values were chosen as they represent the maximum excursions one may expect in a practical implementation. The minimum perturbations for the closed loop models were limited to 0.01 rad/s and 1V. Values less than this were not considered because they have negligible effect on the plant output.

By inspection of Figures 2.12, 2.13, 2.14, and 2.15, it can be seen that the linear and nonlinear simulation models closely resemble each other. It can be seen that the dominant mode of the frequency-active power channel occurs at $s = 0$. This is due to the integrator that converts frequency-to-phase. Since perturbations in frequency are quite small in practice, there is very little linearization error. It can be seen that the dominant

Table 2.2: Parameters used to validate the open loop model.

Parameter	Value
V_{INV}	170 V
ω_{INV}	377 rad/s
V_{Grid}	170 V
ω_{Grid}	377 rad/s
$Z_L + Z_{\text{TH}}$	$j\ 0.1\ \Omega$
Lowpass Filter	$\frac{1421}{s^2 + 53.32 \cdot s + 1421}$

Table 2.3: Parameters used to validate the closed loop model.

Parameter	Value
$V_{\text{INV MAX}}$	180 V
$\omega_{\text{INV MAX}}$	380 rad/s
V_{Grid}	170 V
ω_{Grid}	377 rad/s
$Z_L + Z_{\text{TH}}$	$j\ 0.1\ \Omega$
k_p	$1 \cdot 10^{-4}\ \text{rad/s/w}$
k_v	$1 \cdot 10^{-4}\ \text{V/VA}$
Lowpass Filter	$\frac{1421}{s^2 + 53.32 \cdot s + 1421}$

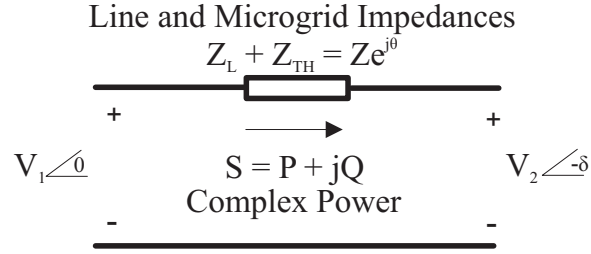


Figure 2.9: Two inverter system where “ $Ze^{j\theta}$ ” is the sum of the line and Thevenin impedances.

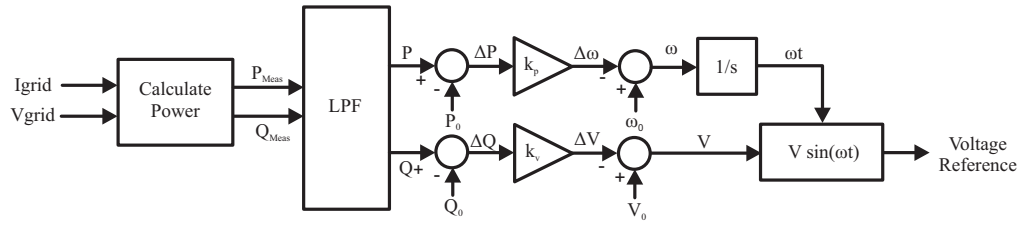


Figure 2.10: Conventional implementation of droop control.

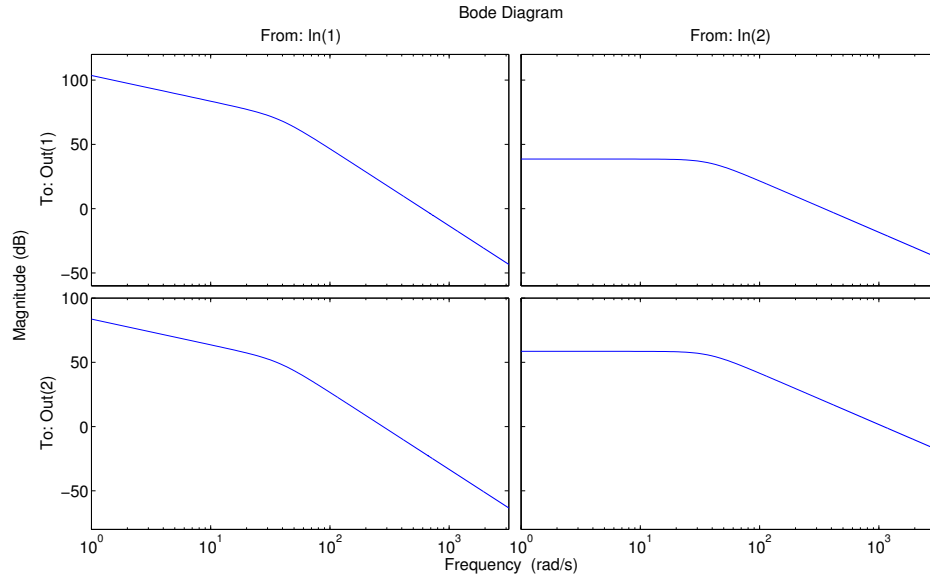


Figure 2.11: Bode plot of system transfer function using droop parameters in Table 2.3. Note: The typical MIMO convention is used where the rows and columns represent the two outputs and inputs respectively.

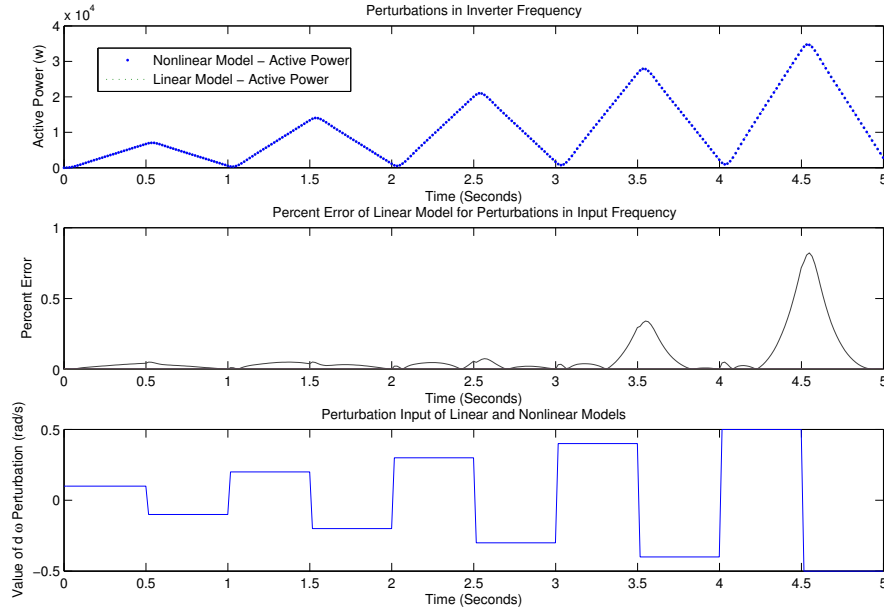


Figure 2.12: Transient power response of open loop linear and nonlinear systems for a sequence of perturbations in frequency. The percent error plot quantifies the linearization error.

modes of the voltage-reactive power channel are dictated by the lowpass filter used to average the calculated instantaneous power. Since the voltage difference between the two sources shown in Figure 2.9 is typically much larger than the frequency difference, there is typically more error.

The errors in Figures 2.12, 2.13, 2.14, and 2.15 consider error in the controlled power variable. This is to say that for an inductive line, as considered here, perturbations in frequency control active power and perturbations in voltage control the reactive power. Error due to cross coupling is negligible compared to the controlled variable and is not considered here.

The error in frequency response may be quantified using the multiplicative representation defined in (2.36) and (2.37), where G_0 is the linear model, G is the

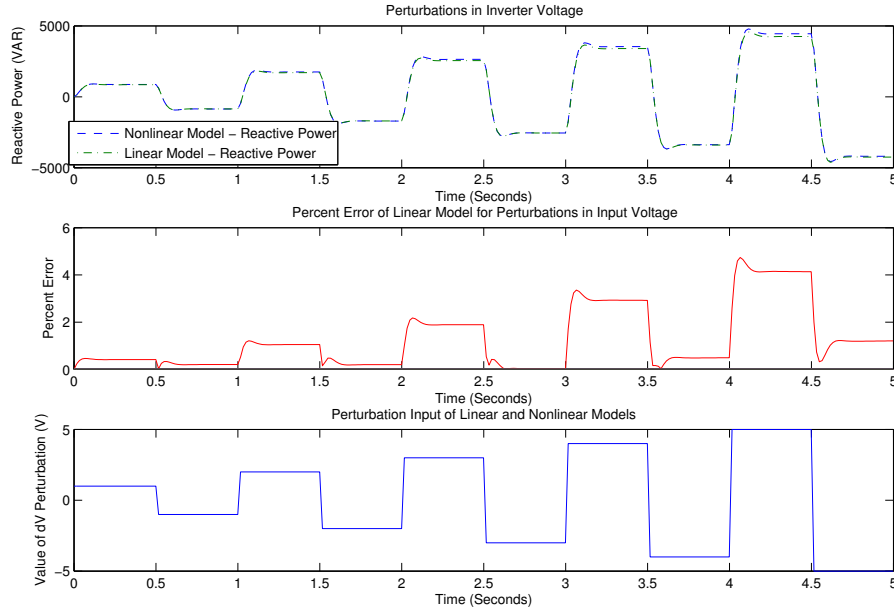


Figure 2.13: Transient power response of open loop linear and nonlinear systems for a sequence of perturbations in voltage. The percent error plot quantifies the linearization error.

nonlinear model, Δ_m is the multiplicative uncertainty, and δ , V_1 remain in a suitably small region around the operating point. The calculation is made by taking the FFT of the linear and nonlinear models and performing the computation (2.37). A plot of the open and closed loop multiplicative errors are shown in Figure 2.16 and Figure 2.17 respectively.

$$G_{\Delta_m} \approx G_0(I + \Delta_m) \quad (2.36)$$

$$\Delta_m = G_0^{-1}(G - G_0) \quad (2.37)$$

Figure 2.16 and Figure 2.17 also include upper bounds which are useful for robust control design, in particular noting the maximum useful control bandwidth. The applicability of the linearization error upper bound in control design is expressed in Figure 2.18.

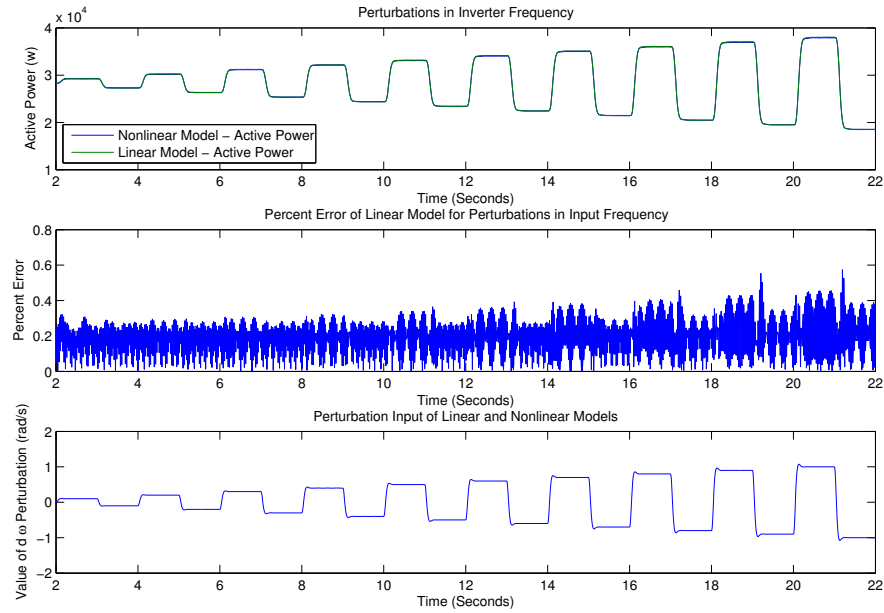


Figure 2.14: Transient power response of closed loop linear and nonlinear systems for a sequence of perturbations in frequency. The error is quite small and is dominated by 120 Hz ripple from the nonlinear model. The percent error plot quantifies the linearization error.

Of particular interest are the large excursions in Figure 2.16 and Figure 2.17. The excursions occur at 754 rad/s and 377 rad/s in the frequency-active power and voltage-reactive power channels respectively. These are predicted by the model since the frequency-active power channel truncates quadratic and higher order terms. Since the quadratic components will contribute the most to the nonlinear response, and the input is 377 rad/s, the non-zero harmonic will occur at 754 rad/s. Conversely, the voltage-reactive power channel does not truncate higher order terms and the error is due to different coefficient values at different operating points. Therefore the voltage channel error occurs at the fundamental frequency of 377 rad/s.

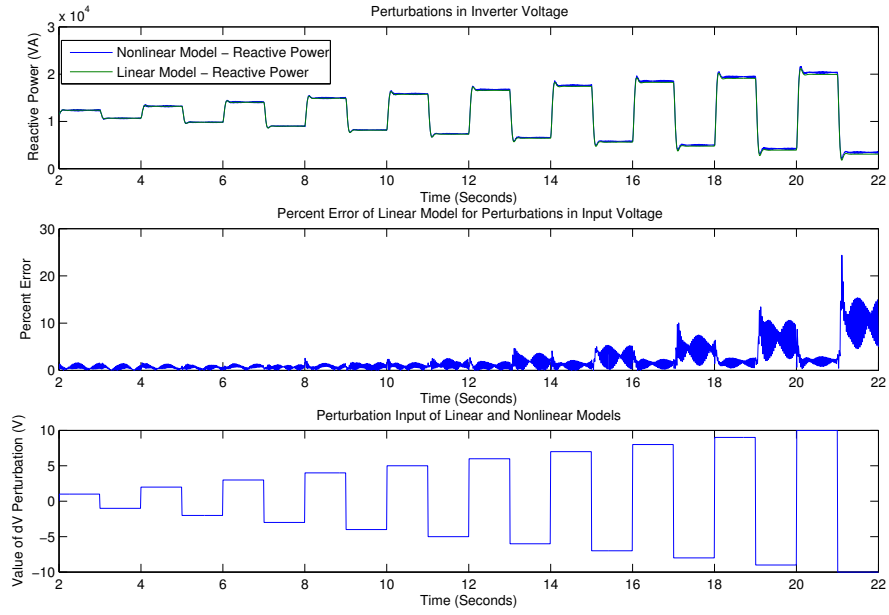


Figure 2.15: Transient power response of closed loop linear and nonlinear systems for a sequence of perturbations in voltage. The percent error plot quantifies the linearization error.

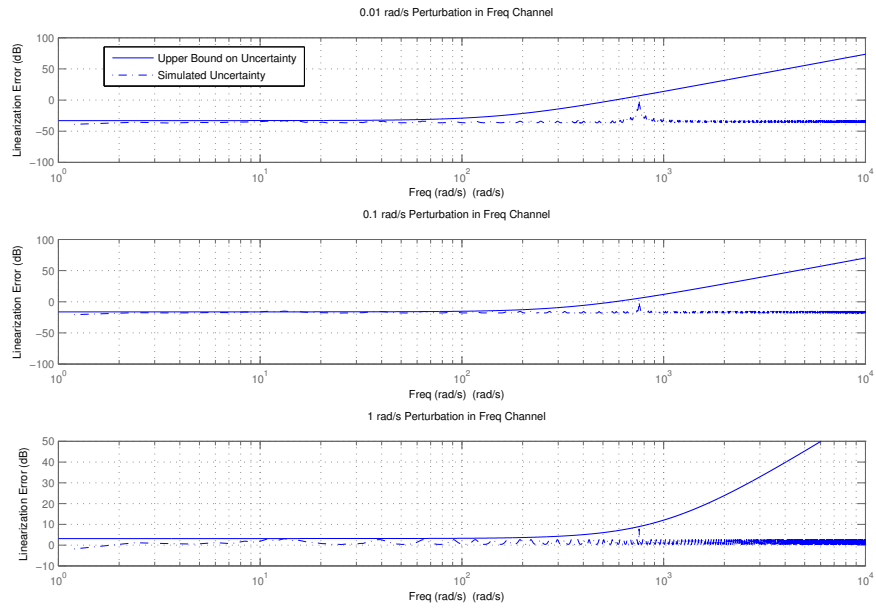


Figure 2.16: Multiplicative uncertainty of open loop system for perturbations in frequency.

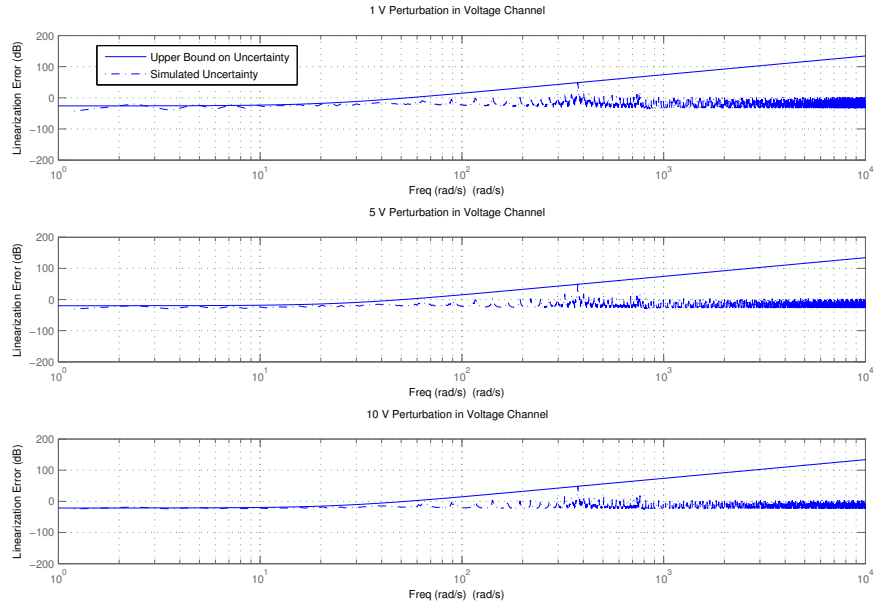
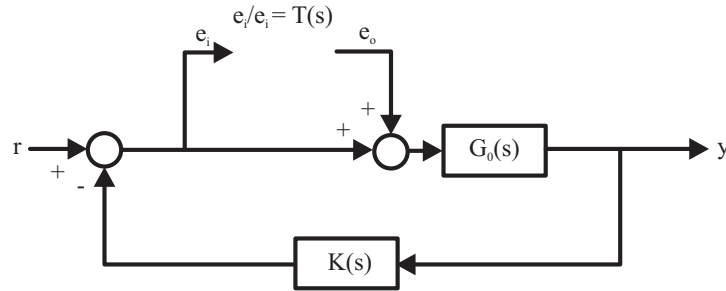
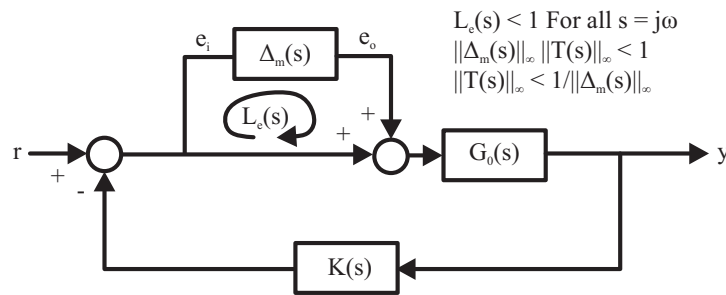


Figure 2.17: Multiplicative uncertainty of closed loop system for perturbations in voltage.



Closed loop nominal plant without linearization error.



Closed loop nominal plant with linearization error bound $\Delta_m(s)$.

Figure 2.18: Illustration of linearization error ($\Delta_m(s)$) and derivation of closed loop constraint based on the small gain theorem [49].

Chapter 3

COPRIME FACTORIZATION AND THE GAP METRIC

Given any MIMO or SISO transfer function G_0 that is both controllable and observable, the left and right coprime factorizations are written respectively in (3.1).

$$G_0 = \tilde{M}_L^{-1} \tilde{N}_L = \tilde{N}_R \tilde{M}_R^{-1} \quad (3.1)$$

In this representation, the terms $\tilde{N}_{L,R}$ and $\tilde{M}_{L,R}$ are stable coprime transfer functions. For these transfer functions to be stable, $\tilde{N}_{L,R}$ must contain all the RHP zeros and $\tilde{M}_{L,R}$ must contain all the RHP poles of G_0 as RHP zeros. For the transfer functions to be coprime, there cannot be common RHP zeros in $\tilde{N}_{L,R}$ and $\tilde{M}_{L,R}$ (the representation must be minimal). The left and right coprime factorizations may be normalized. The normalized left coprime factorization is given in (3.2).

$$M_L(j\omega)M_L^*(j\omega) + N_L(j\omega)N_L^*(j\omega) = I, \forall \omega \quad (3.2)$$

Such representations provide a convenient framework for representing uncertainty as given in (3.3) and shown in Figure 3.1. Considering Figure 3.1, expressions (3.4), (3.5), (3.6), and the small gain theorem, one will arrive at the stability constraint (3.7). Since the M_L and N_L terms are normalized, one may also express the stability criterion as (3.8). The stability relationship given in (3.8) is helpful to relate the internal stability of a system to a set of standard loop relationships as given in (3.9) which expresses the exogenous input-output relationship in Figure 3.2. One may also express (3.8) as a MIMO (or SISO) stability margin that is more general than the traditional gain and phase margins. Such an expression is given in (3.10).

$$G_{\Delta} = (M_L + \Delta_M)^{-1} (N_L + \Delta_N), \quad M_L, N_L \in H_{\infty} \quad (3.3)$$

With:

$$\| [\Delta_M, \Delta_N] \|_{\infty} < \varepsilon \quad (3.4)$$

$$\begin{pmatrix} z_1 \\ z_2 \end{pmatrix} = \begin{pmatrix} K \\ I \end{pmatrix} (I - GK)^{-1} M_L^{-1} w \quad (3.5)$$

$$w = (\Delta_N, -\Delta_M) \begin{pmatrix} z_1 \\ z_2 \end{pmatrix} \quad (3.6)$$

$$\left\| \begin{pmatrix} K \\ I \end{pmatrix} (I - GK)^{-1} M_L^{-1} \right\|_{\infty} \leq 1/\varepsilon \quad (3.7)$$

$$\left\| \begin{pmatrix} K \\ I \end{pmatrix} (I - GK)^{-1} (I, G) \right\|_{\infty} \leq 1/\varepsilon \quad (3.8)$$

$$\begin{pmatrix} z_1 \\ z_2 \end{pmatrix} = \begin{pmatrix} K(I - GK)^{-1} & K(I - GK)^{-1}G \\ (I - GK)^{-1} & (I - GK)^{-1}G \end{pmatrix} \begin{pmatrix} w_1 \\ w_2 \end{pmatrix} \quad (3.9)$$

$$g(G, K) = \left\| \begin{pmatrix} K \\ I \end{pmatrix} (I - GK)^{-1} (I, G) \right\|_{\infty}^{-1} \quad (3.10)$$

The stability criteria (3.10) is useful when considering the stability of an uncertain system. An uncertain system may be expressed as a family of plants where there is some distance between plants in the set of possible plants. Such a distance is referred to as a gap

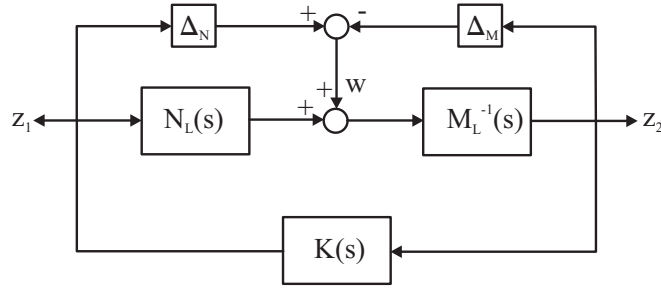


Figure 3.1: Block diagram representation of coprime factorized system with uncertainty.

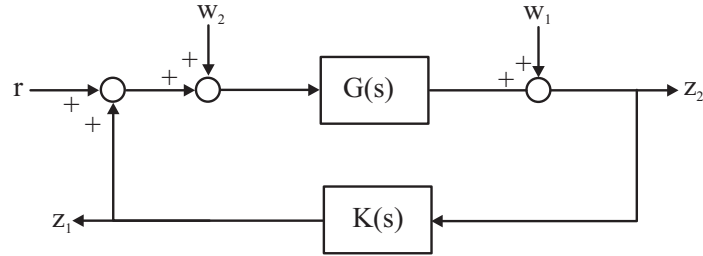


Figure 3.2: Block diagram representation of system with exogenous inputs and outputs.

metric and implies the stability condition (3.11). This result may be extended to include a performance criterion given as (3.12).

$$\delta_v < g(G_0, K) \quad (3.11)$$

Where δ_v is the distance between plants.

$$g(G_1, K_1) \geq g(G_0, K_0) - \delta_v(G_1, G_0) - \delta(K_1, K_0) \quad (3.12)$$

Where δ_v is the distance between plants and δ is the distance between controllers.

Chapter 4

GLOVER MCFARLANE LOOPSHAPING BACKGROUND

Glover McFarlane loopshaping is a method used to synthesize an H_∞ controller with a relatively simple design methodology [38]. The loopshaping and robust stabilization is achieved by applying pre and post weights to the plant to achieve the desired loop shape ($G_s = W_2 G W_1$), and simultaneously minimizing the cost functions (4.1) and (4.2).

$$\gamma_1 = \min_K \left\| \begin{bmatrix} I \\ K \end{bmatrix} (I - G_s K)^{-1} \begin{bmatrix} G_s & I \end{bmatrix} \right\|_\infty \quad (4.1)$$

$$\gamma_2 = \min_K \left\| \begin{bmatrix} I \\ G_s \end{bmatrix} (I - K G_s)^{-1} \begin{bmatrix} K & I \end{bmatrix} \right\|_\infty \quad (4.2)$$

Where $K = W_2 K_s W_1$.

The resulting controller is such that the sigma plot of the shaped loop is close to the target loop shape while ensuring that the closed loop system is also robustly stable. The robust stability margin is given by considering the normalized coprime factorization of the shaped plant and the metric γ in (4.3) and (4.4) respectively.

$$G_s = (N_R + \Delta_N)(M_R + \Delta_M)^{-1} \quad (4.3)$$

$$\left\| \begin{bmatrix} \Delta_N \\ \Delta_M \end{bmatrix} \right\|_{\infty} < 1/\gamma \quad (4.4)$$

4.1 Glover-McFarlane Loopshaping Applied to Droop Control with Dynamics

Two plant formulations may be used to design a GMFDC for an inverter. The first plant formulation is shown in Figure 4.1 and has the advantage of being simple to formulate as a controller synthesis problem, but may be difficult to achieve the required DC gain. The second formulation is shown in Figure 4.2 and ensures the appropriate DC gain (assuming the controller does not have a pole at the origin) but is more difficult to formulate as a controller synthesis problem and is not considered in this report.

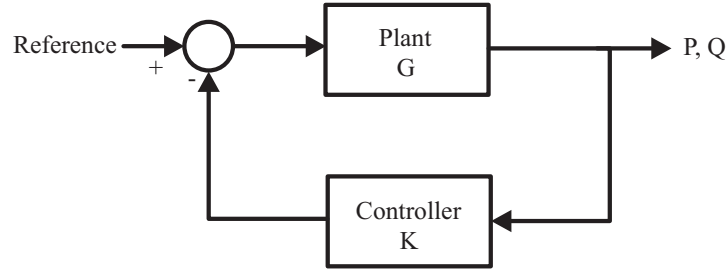


Figure 4.1: Problem formulation used to design dynamic controller.

Synthesizing Glover McFarlane Controllers for a Small Microgrid

The controller synthesis configuration presented in Figure 4.1 was used to design the controllers for a nine-inverter microgrid. The parameters of the inverters used in the design and validation of the proposed controller are given in Table 4.1.

The bode plot of the plant is shown in Figure 4.3. Based on this Bode plot and the desired DC gain of the controller (see Table 4.1), the weight used to synthesize a Glover McFarlane loopshaping controller is given as (4.5). The resulting sensitivity and complementary sensitivity sigma plots are shown in Figure 4.4. Comparing the sensitivity

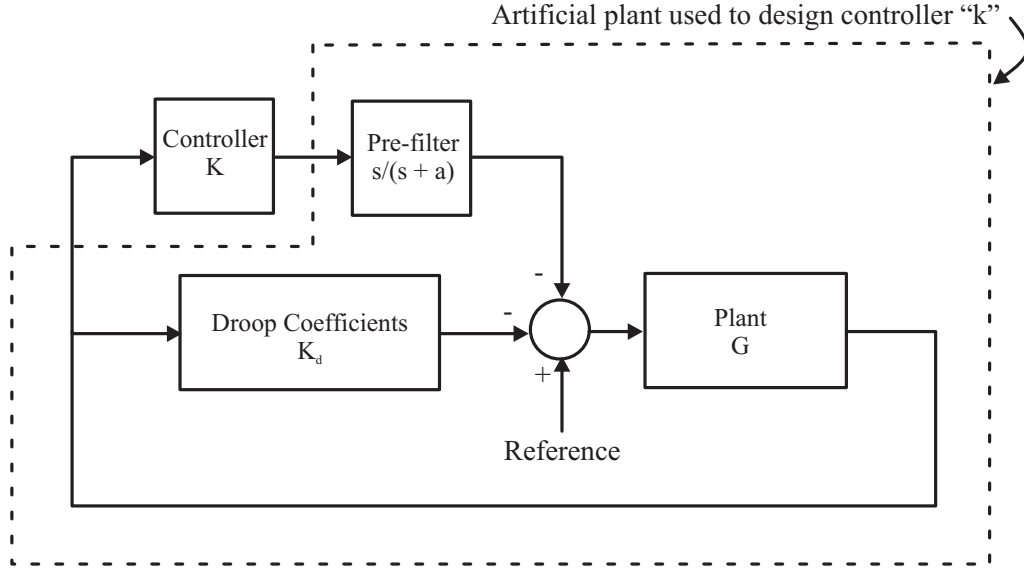


Figure 4.2: Problem formulation used to design a controller “k”.

and complementary sensitivity sigma plots for the dynamic and non-dynamic controllers, Figures 4.4 and 4.5 respectively, one will notice that the conditioning of the system with the dynamic controller is much better which will undoubtedly lead to better performance.

$$W_1 = \begin{pmatrix} 1.2 \cdot 10^{-4} & 0 \\ 0 & 5 \cdot 10^{-4} \end{pmatrix} \frac{(s/37.7 + 1)^2}{(s/100 + 1)(s/200 + 1)} \quad (4.5)$$

Assume that each channel has an uncertain DC value and may be within 50% of the nominal value given in (4.6) where $k_i \in [0.5, 1.5]$, $i = 1, 2, 3, 4$.

$$G = \begin{pmatrix} g_{11} \cdot k_1 & g_{12} \cdot k_2 \\ g_{21} \cdot k_3 & g_{22} \cdot k_4 \end{pmatrix} \quad (4.6)$$

Using this uncertainty description, the Matlab function “robuststab” may be used to

Table 4.1: Parameters used in the design and validation of the proposed controller. Note that the inverter parameters are given in terms of their maximum values and grid parameters are given in terms of their nominal values.

Parameter	Value
V_{INV}	$180 V_{peak}$
ω_{INV}	380 rad/s
V_{PCC}	$170 V_{peak}$
ω_{PCC}	377 rad/s
Z_L	$j 0.1 \Omega$
k_p	$1 \cdot 10^{-4} \text{ rad/s/w}$
k_v	$3.5 \cdot 10^{-6} \text{ V/VA}$
LPF Corner Frequency	37.7 rad/s

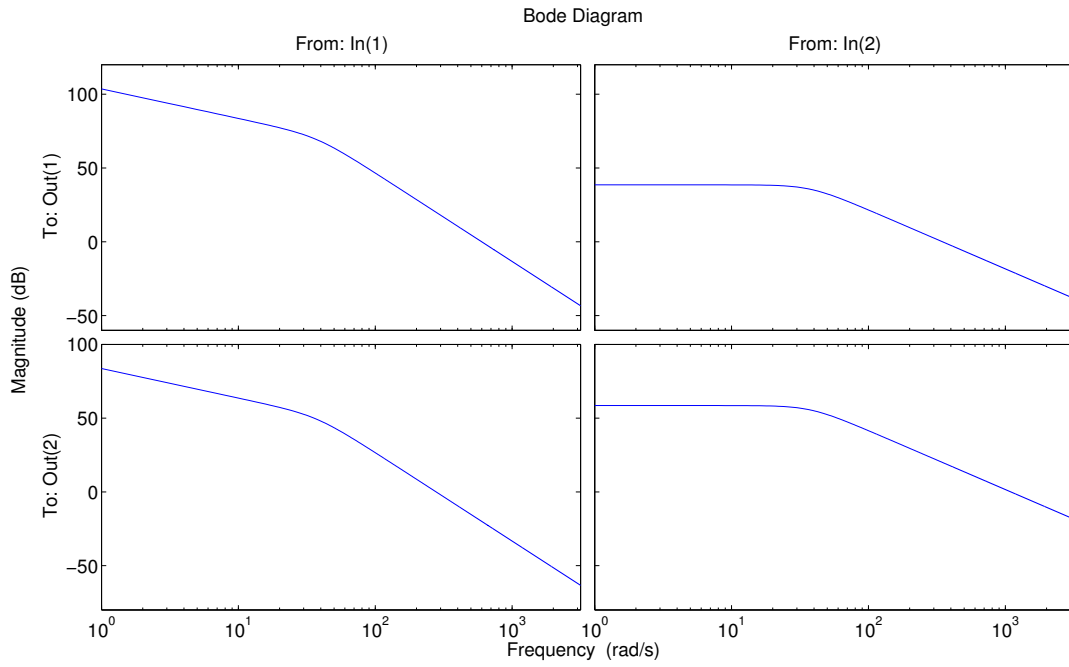


Figure 4.3: Bode magnitude plot of the plant. Note: The typical MIMO convention is used where the rows and columns represent the two outputs and inputs respectively.

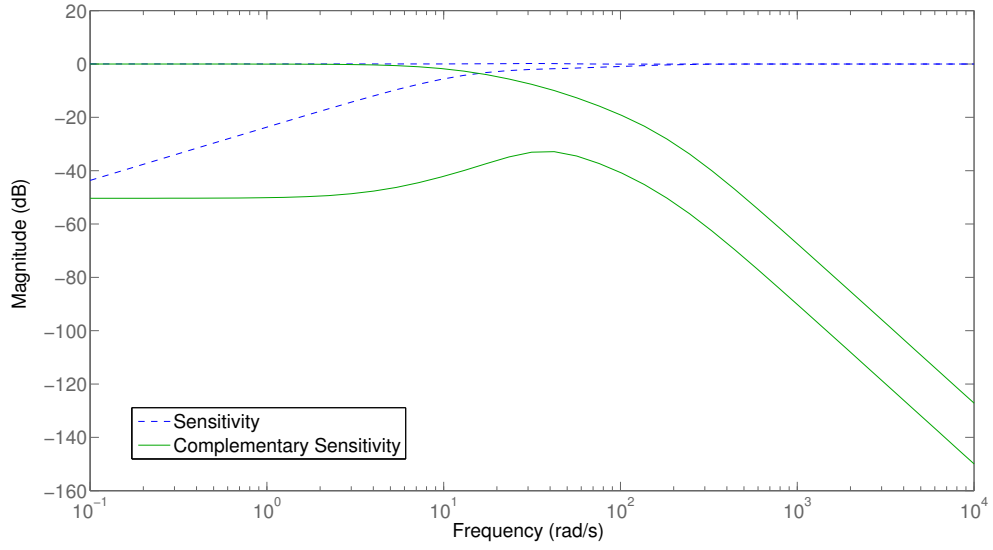


Figure 4.4: Sigma plot of the inverter sensitivity and complementary sensitivity responses when using a Glover McFarlane loopshaping controller.

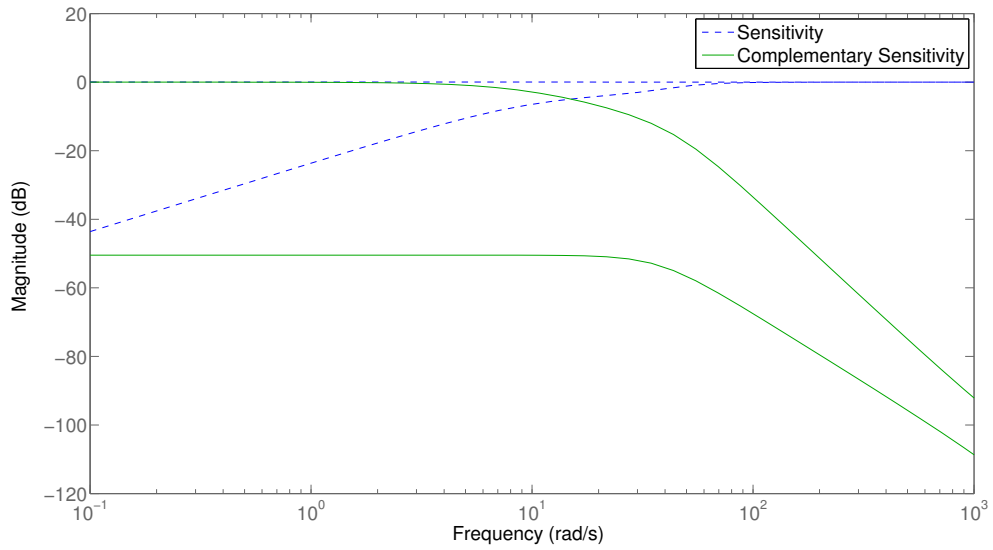


Figure 4.5: Sigma plot of the inverter sensitivity and complementary sensitivity responses when using conventional droop control with no dynamics.

Table 4.2: Results of report generated using the Matlab command “robuststab”. Note that the sensitivity is the reduction in stability margin divided by change in the given parameter. The standard abbreviation for “with respect to” wrt is used here.

Metric	Controller without Dynamics	Controller with Dynamics
Tolerable Uncertainty	84.2%	110%
Sensitivity wrt k_1	87%	46%
Sensitivity wrt k_2	152%	0%
Sensitivity wrt k_3	214%	72%
Sensitivity wrt k_4	567%	0%

generate a report regarding the stability of the system. Such an analysis was done using the synthesized controller and the constant gain controller. The results are given in Table 4.2.

From Table 4.2 it may be seen that the system using a Glover McFarlane loopshaping controller is robustly stable for 25.8% more uncertainty and is less sensitive to changes in the system parameters. From this alone one begins to see a clear advantage of the dynamic controller.

One may also consider the robustness offered by the two controller approaches using the gap metric. The gap metric for CGDC and GMFDC are shown for a range of DC values in Figure 4.6 and Figure 4.7 respectively. Either plot may be compared to the gap between plants with parameters in the range given in Table 4.3 and gap values shown in Figure 4.9. Using the inequalities in 3.11 or 3.12 in Section 3 illustrates the superior robustness offered by the GMFDC approach. One may arrive at the same conclusion by simply noting the pointwise difference between the surface plots (gap metrics) in Figure 4.6 and Figure 4.7 which are shown in Figure 4.8.

Table 4.3: Range of values about nominal operating point. Note that “ Δ ” is a factor denoting the tolerance of any given parameter value.

Parameter	Range of Values
V_{SST}	$170(1 \pm \Delta) V_{peak}$
V_{grid}	$179(1 \pm \Delta) V_{Peak}$
$ Z_{Line} $	$0.1(1 \pm \Delta) \Omega$
$\angle Z_{Line}$	$\pi/2(1 - 2\Delta)$ rad
δ	$0.1(1 \pm \Delta)$ rad

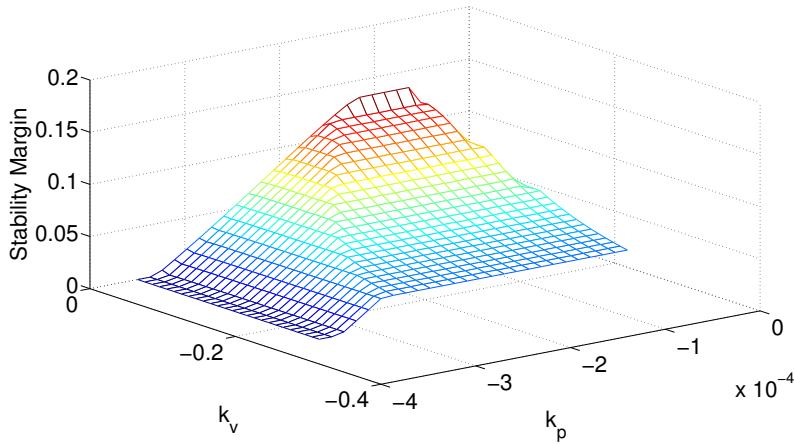


Figure 4.6: Stability margin for constant gain droop control over a wide range of gains. The stability margin is defined as the reciprocal of the gap metric in equation (4.4) in the first section of this chapter.

Nine-Inverter Microgrid Testbed

The synthesized dynamic controller and the constant gain controller were tested using a microgrid consisting of nine single-phase inverters as shown in Figure 4.10. The line and load impedances for this system are given in Table 4.4. One should note that “Load 3” is disconnected during startup and is connected at $t = 1$ second. This is used to simulate a perturbation in the system. The system is simulated using a nonlinear (large

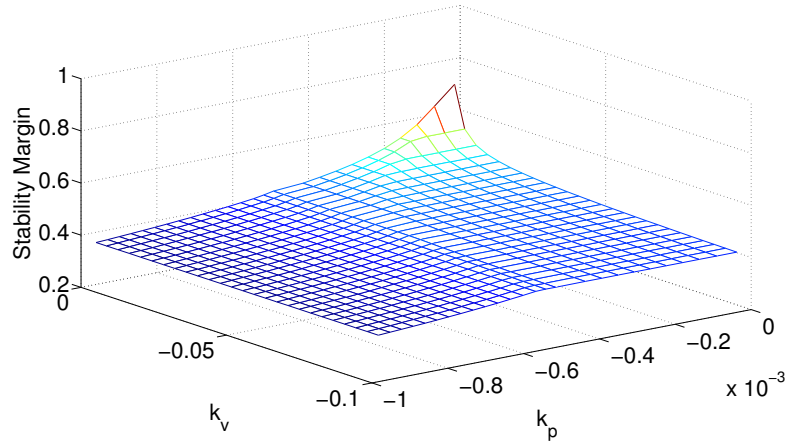


Figure 4.7: Stability margin for Glover McFarlane controllers with a wide range of DC gains. The stability margin is defined as the reciprocal of the gap metric in equation (4.4) in the first section of this chapter.

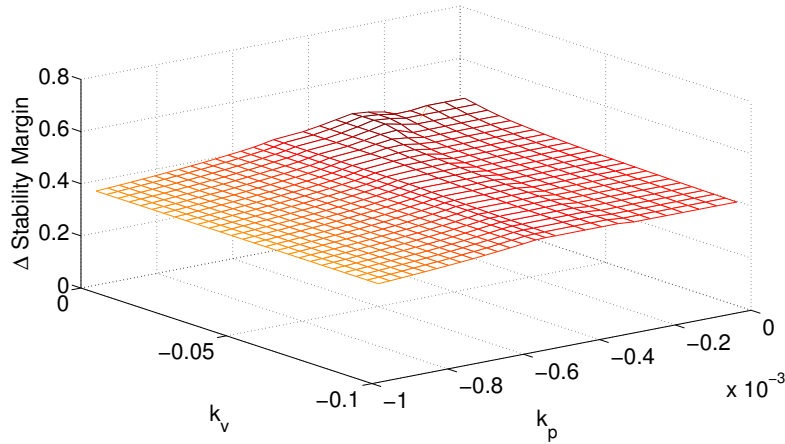


Figure 4.8: This figure illustrates the difference between stability margins for Glover McFarlane and constant gain droop controllers with a wide range of DC gains. The stability margin is defined as the reciprocal of the gap metric in equation (4.4) in the first section of this chapter.

signal) model for each inverter comprised of blocks in the Simulink blockset

“SimPowerSystems”.

The traditional droop approach that does not have dynamics, completely

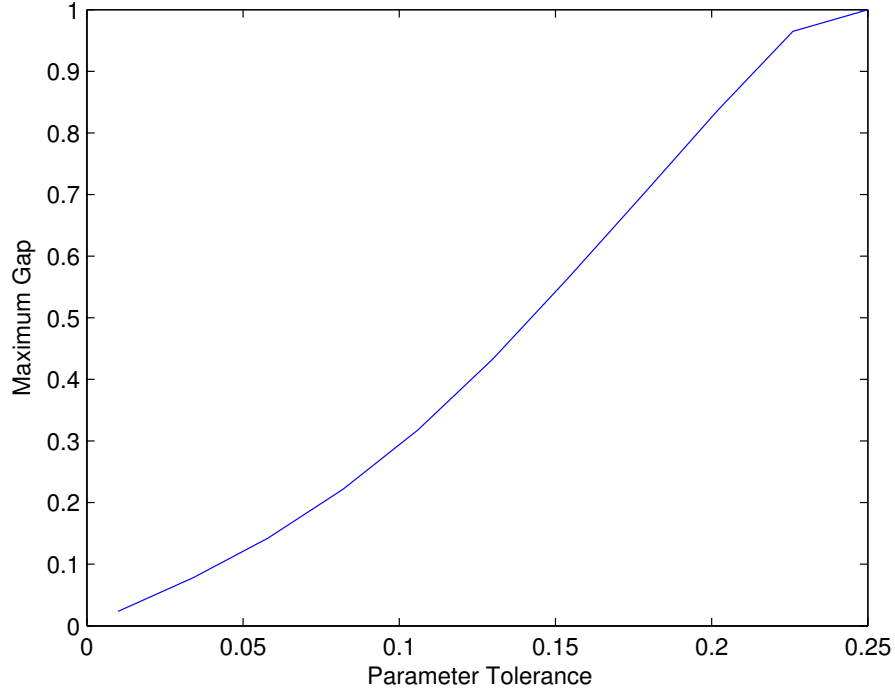


Figure 4.9: This illustrates the gap between plants with parameter values in the set in Table 4.3.

destabilizes the system as shown in Figures 4.11, 4.12, and 4.13. The constant gain control method was augmented such that each inverter would have a virtual output impedance as proposed in [22]. This was implemented for a virtual resistive output impedance and a virtual inductive output impedance. The value of the impedance was determined in a heuristic fashion by starting with a large impedance value and slowly decreasing that value until the system became unstable. The smallest virtual impedances such that the system is stable are 0.025Ω and $j0.1\Omega$. The transient response of the active and reactive power are shown for each inverter using both modifications in figures 4.14-4.19. While these transient responses may appear to be good, it is important to note that the designer still has limited degrees of freedom (the “controller” is at most first order), there is not a structured design methodology for the virtual output impedance approach, it may be difficult to keep

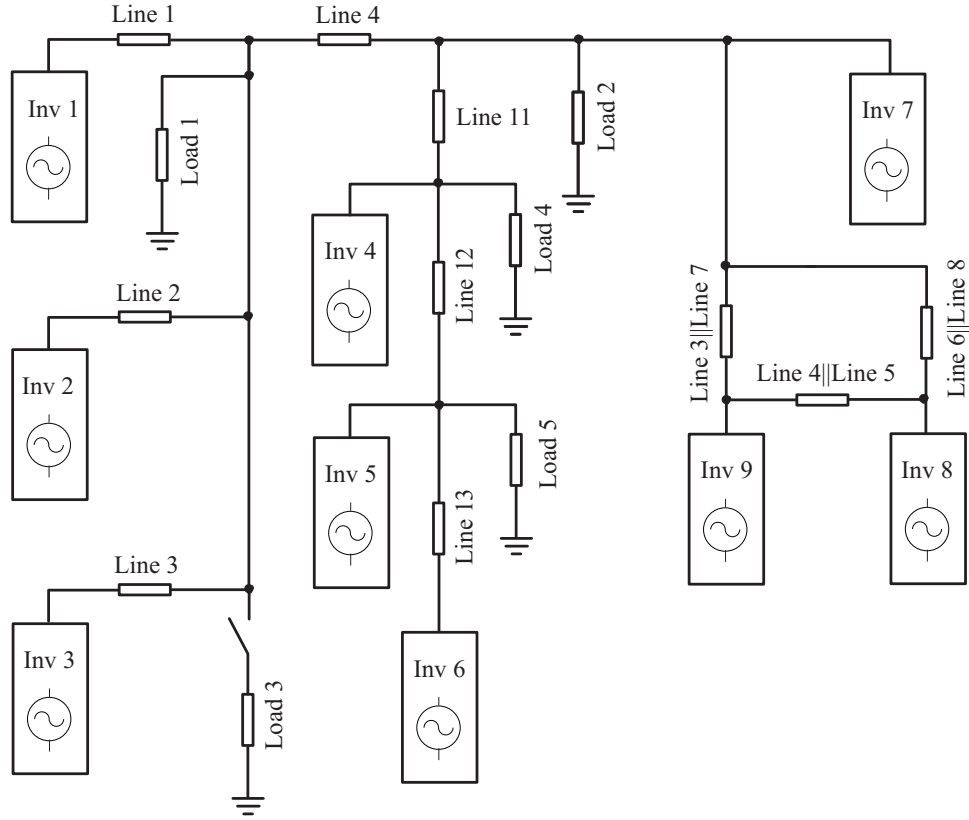


Figure 4.10: A microgrid with nine inverters.

the output voltage within the desired range¹, and the controller is not as robust as a GMFDC. The gap margins of CGDC, CGDC with virtual output resistance, CGDC with virtual output inductance, and GMFDC are 0.37, 0.39, 0.55, and 0.64 respectively. Based on Figure 4.9 these values correspond to parametric uncertainty between 10 % for CGDC to 17 % for GMFDC. It is generally thought that increasing the output impedance of an inverter will improve the power sharing. Based on the simulation results, the system with virtual output impedance has approximately 1% better power sharing than the system using GMFDC. Based on these issues, there is a clear advantage of the GMFDC approach and the CGDC variations will not be considered further.

¹It may be difficult to keep the output voltage within the desired range because the output voltage will drop based on the droop parameters and in proportion to the load current which is subject to a great deal of uncertainty.

Table 4.4: Parameters used in the testing of the nine-inverter microgrid.

Parameter	Value
Line 1 Impedance	$j0.2458m\Omega$
Line 2 Impedance	$j0.2151m\Omega$
Line 3 Impedance	$j0.1792m\Omega$
Line 4 Impedance	$j0.2007m\Omega$
Line 5 Impedance	$j0.1859m\Omega$
Line 6 Impedance	$j0.1427m\Omega$
Line 7 Impedance	$j0.1644m\Omega$
Line 8 Impedance	$j0.1490m\Omega$
Line 9 Impedance	$j0.1570m\Omega$
Line 10 Impedance	$j0.1644m\Omega$
Line 11 Impedance	$j0.1880m\Omega$
Line 12 Impedance	$j0.1392m\Omega$
Line 13 Impedance	$j0.2523m\Omega$
Load 1	$1/3 \Omega$
Load 2	1Ω
Load 3	1Ω
Load 4	1Ω

The transient active and reactive power response for inverters 1-9 using GMFDC are shown in Figures 4.20, 4.21, and 4.22. It can be seen that the system is stable and does not overshoot more than 20%. It can also be seen that the system performs equally well for the load step that occurs at $t = 1$ second.

To further test the controller design, the microgrid configuration was changed as shown in Figure 4.23. Maintaining the same GMFDC as the previous case, the system remained stable as shown in Figure 4.24, 4.25, and 4.26. Using the traditional constant gain droop control, all inverters in the system were unstable. The reason for the difference

in results are the phase lag of the plant and the phase lead offered by the dynamic controller. In order to stabilize the system using a constant gain controller, the gain must be lowered until the phase is less than -180° at crossover. This, however, is not always a feasible option as the droop gain is dictated by the frequency, voltage, and power limitations. A significant role in the frequency response, and therefore the stable operating range, is the line impedance. While the dynamic controller has been shown to operate over a wider range (see section 4.1), the range may be further expanded using a gain schedule scheme [16]. Such approaches will be addressed in section 5.1.

The GMFDC was used with a nine-inverter testbed with dynamic load as shown in Figure 4.27. It is important to note that this configuration includes a dynamic load. The parameters and model for the dynamic load are shown in figures 4.28 - 4.30 respectively. The transient response of each inverter is shown in figures 4.31-4.33. It can be seen that all the inverters using GMFDC are well behaved. When the same system (nine-inverter testbed with dynamic load as shown in Figure 4.27) was simulated using CGDC, none of the inverters were stable.

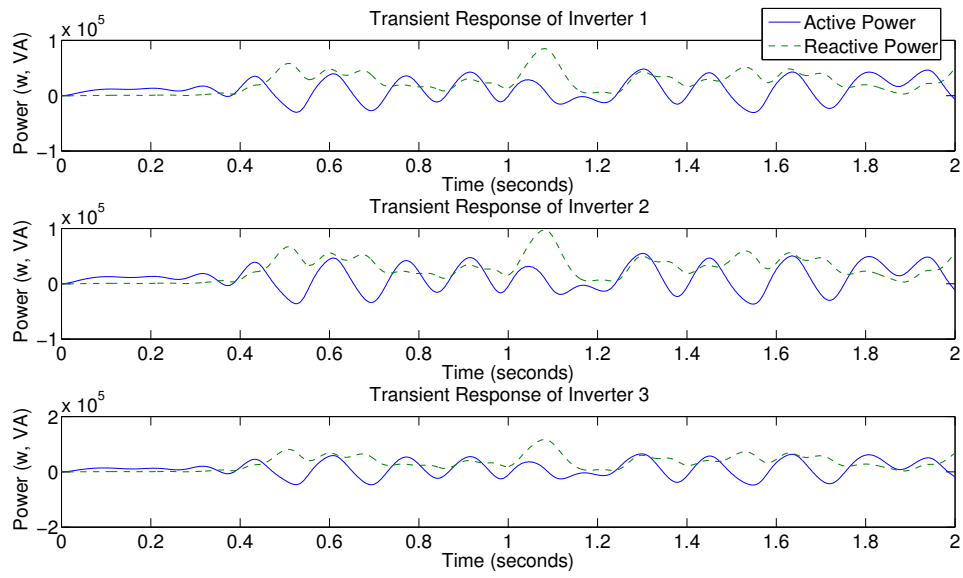


Figure 4.11: Transient power response of inverters 1 – 3 in the nine-inverter microgrid shown in Figure 4.10. Each inverter uses CGDC.

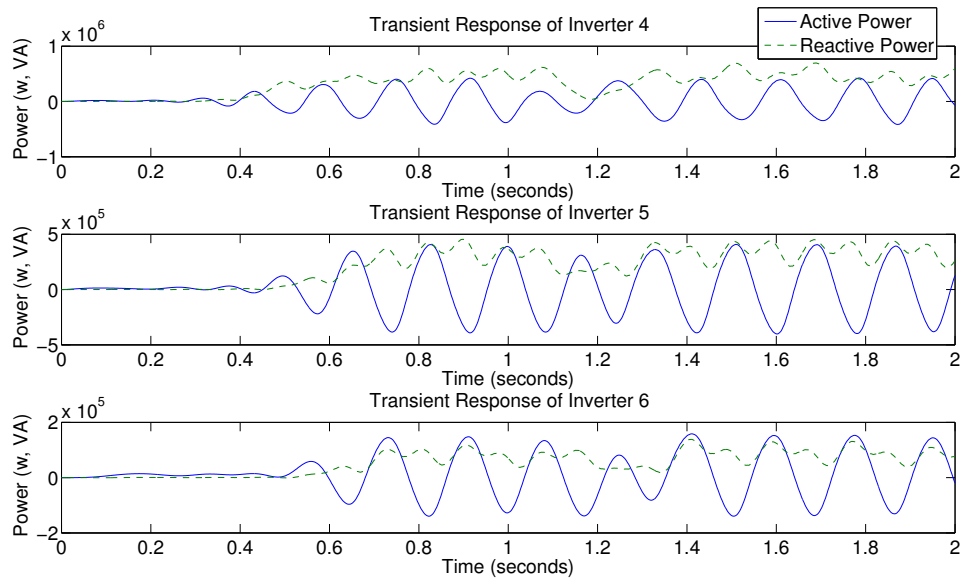


Figure 4.12: Transient power response of inverters 4 – 6 in the nine-inverter microgrid shown in Figure 4.10. Each inverter uses CGDC.

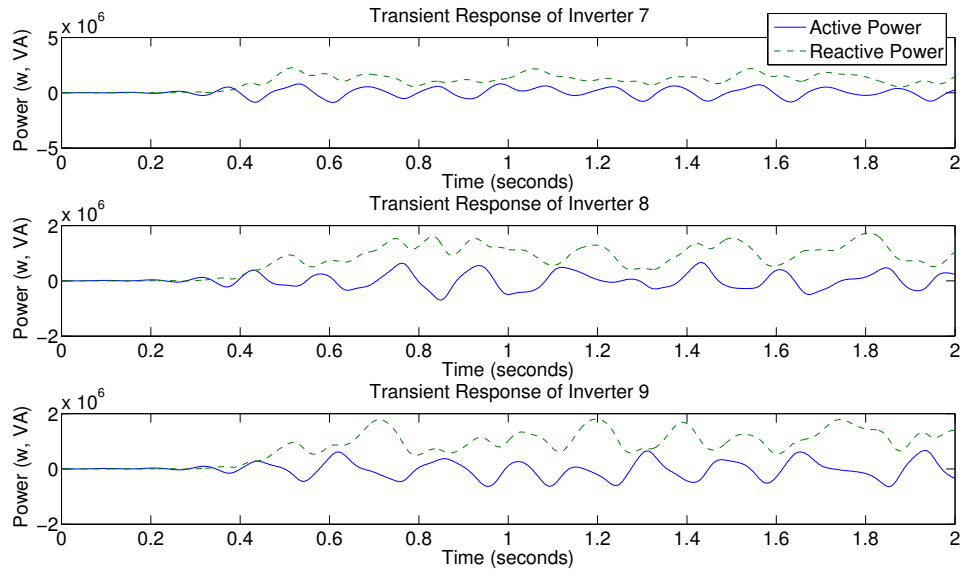


Figure 4.13: Transient power response of inverters 7 – 9 in the nine-inverter microgrid shown in Figure 4.10. Each inverter uses CGDC.

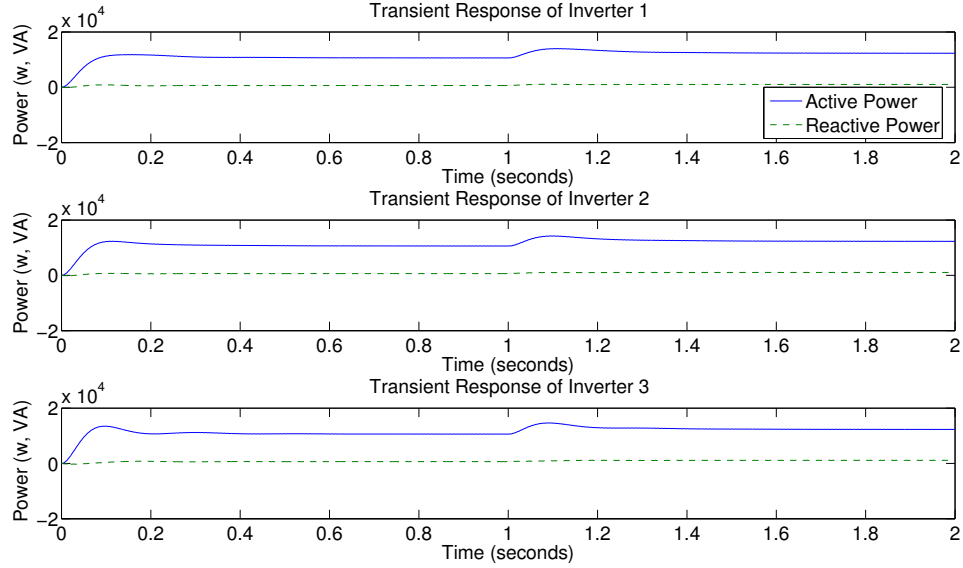


Figure 4.14: Transient power response of inverters 1 – 3 in the nine-inverter microgrid shown in Figure 4.10. Each inverter uses conventional droop control with virtual output resistance.

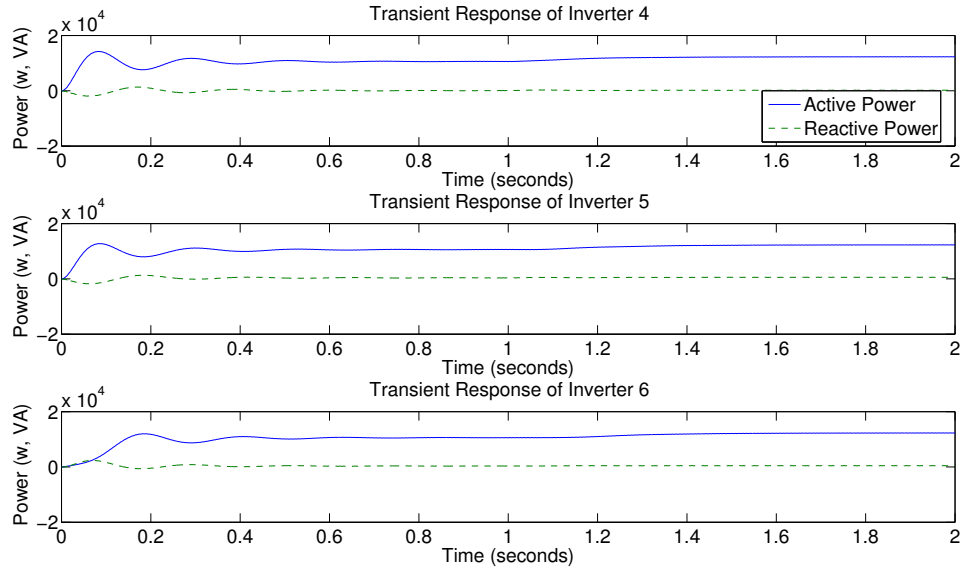


Figure 4.15: Transient power response of inverters 4 – 6 in the nine-inverter microgrid shown in Figure 4.10. Each inverter uses conventional droop control with virtual output resistance.

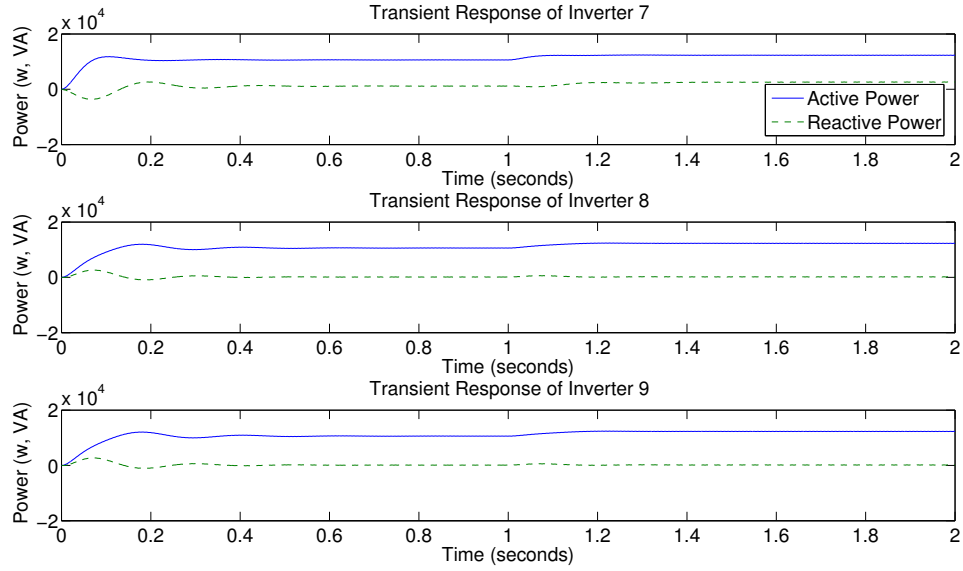


Figure 4.16: Transient power response of inverters 7 – 9 in the nine-inverter microgrid shown in Figure 4.10. Each inverter uses conventional droop control with virtual output resistance.

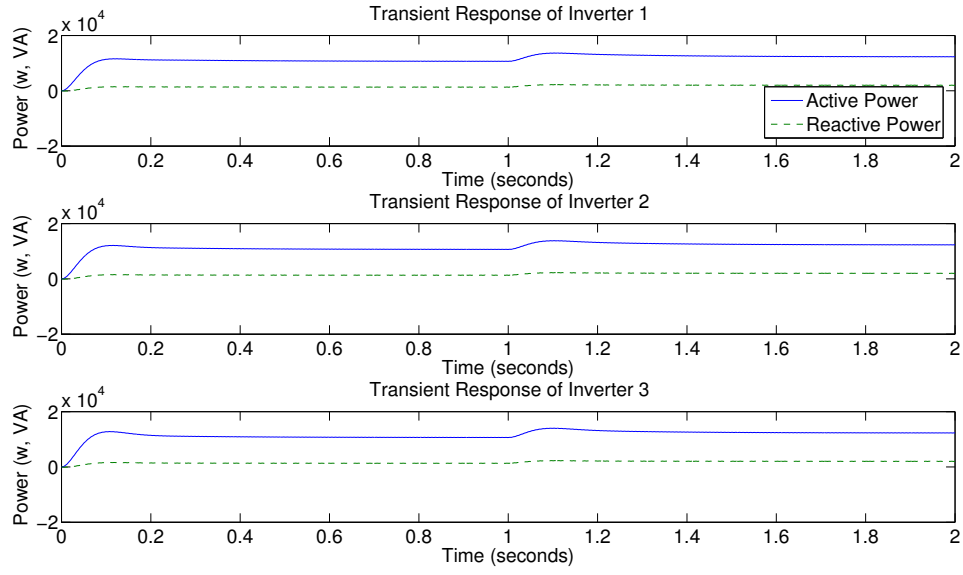


Figure 4.17: Transient power response of inverters 1 – 3 in the nine-inverter microgrid shown in Figure 4.10. Each inverter uses conventional droop control with virtual output inductance.

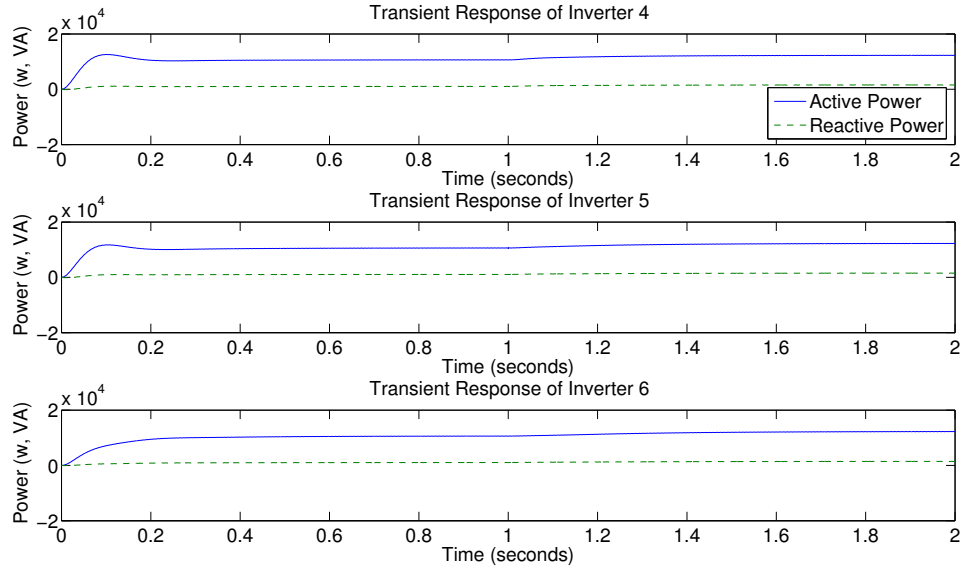


Figure 4.18: Transient power response of inverters 4 – 6 in the nine-inverter microgrid shown in Figure 4.10. Each inverter uses conventional droop control with virtual output inductance.

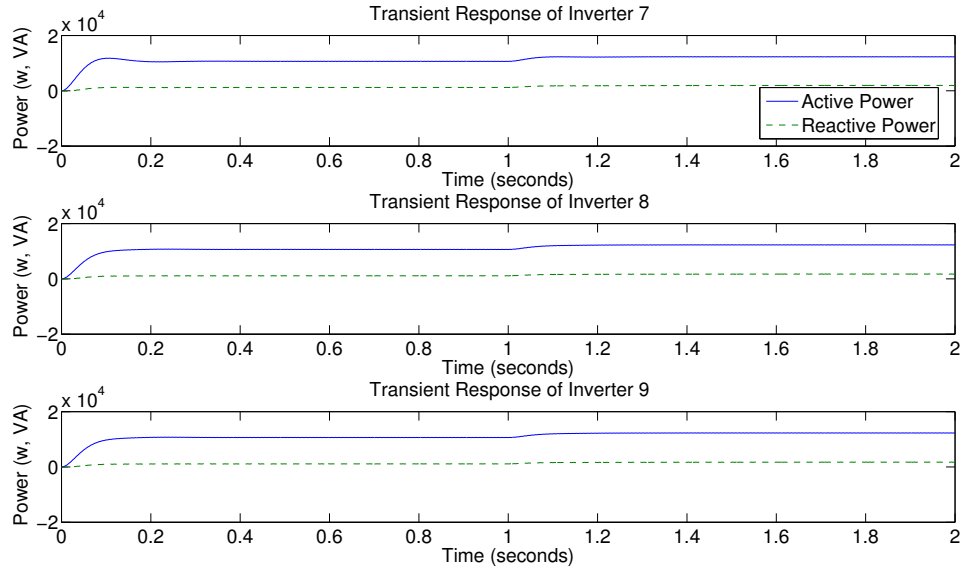


Figure 4.19: Transient power response of inverters 7 – 9 in the nine-inverter microgrid shown in Figure 4.10. Each inverter uses conventional droop control with virtual output inductance.

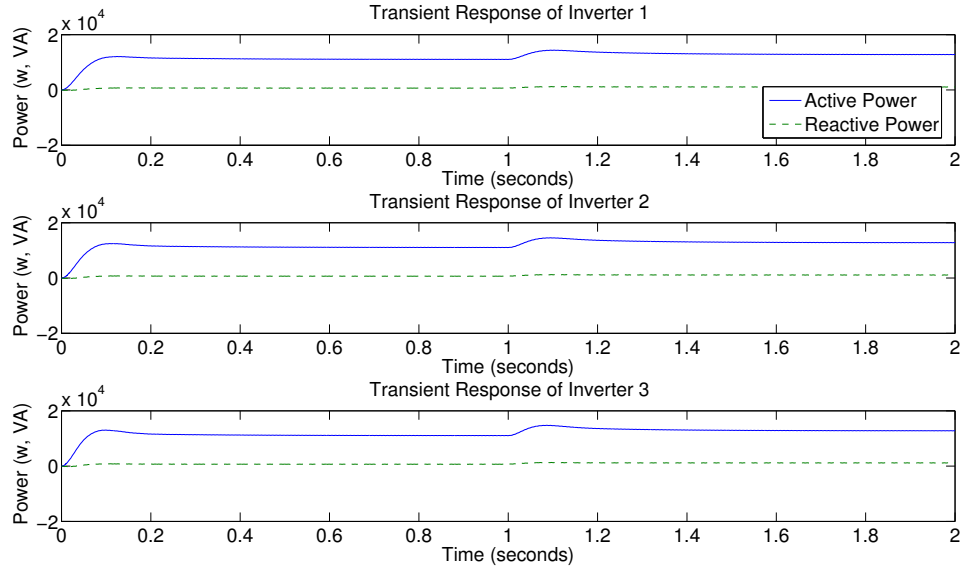


Figure 4.20: Transient power response of inverters 1 – 3 in the nine-inverter microgrid shown in Figure 4.10. Each inverter uses GMFDC.

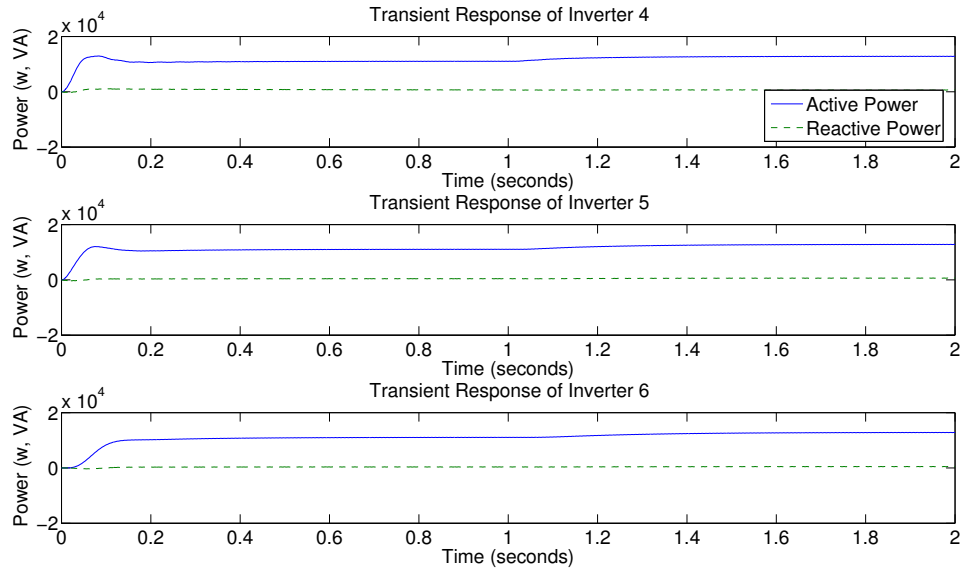


Figure 4.21: Transient power response of inverters 4 – 6 in the nine-inverter microgrid shown in Figure 4.10. Each inverter uses GMFDC.

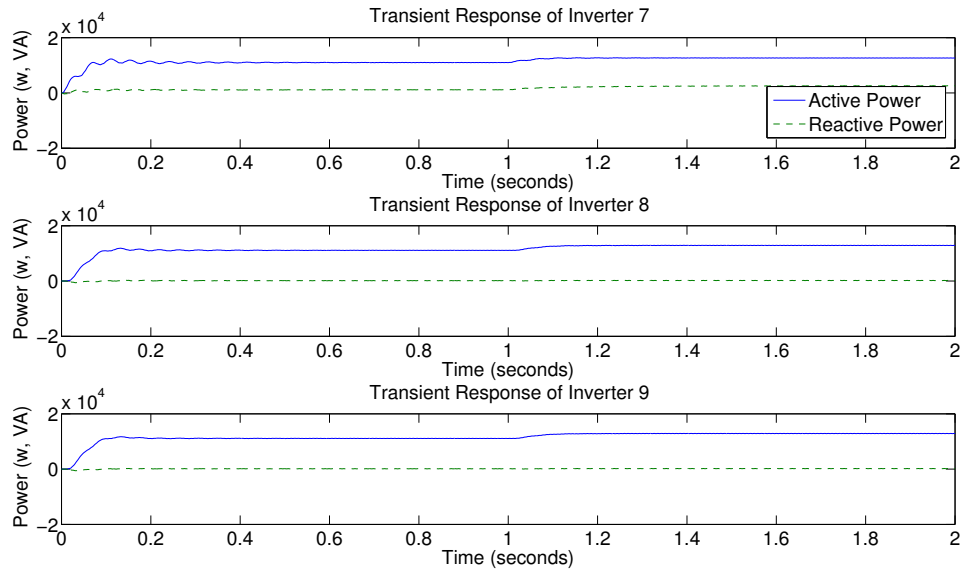


Figure 4.22: Transient power response of inverters 7 – 9 in the nine-inverter microgrid shown in Figure 4.10. Each inverter uses GMFDC.

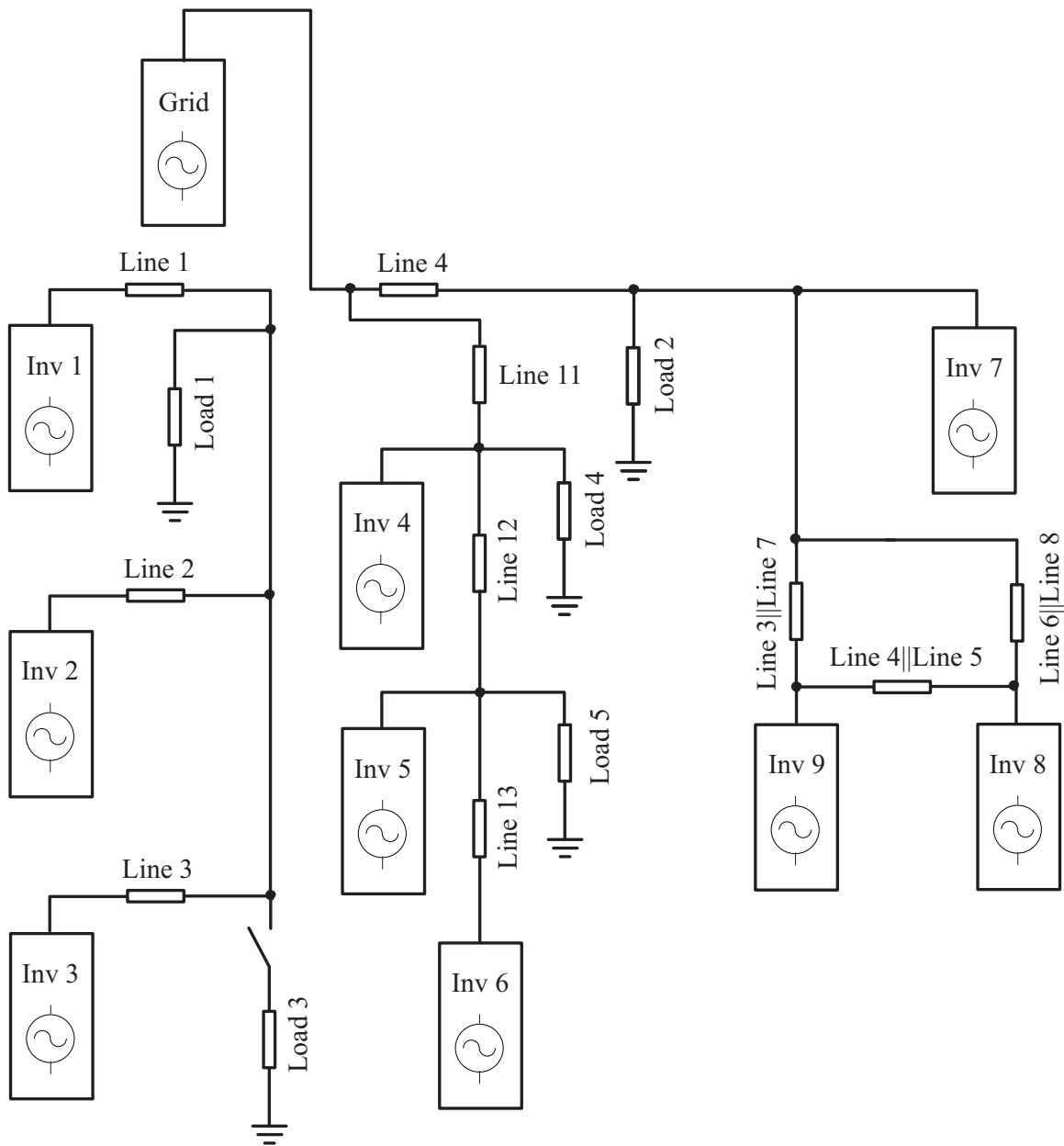


Figure 4.23: An alternate microgrid configuration with nine inverters.

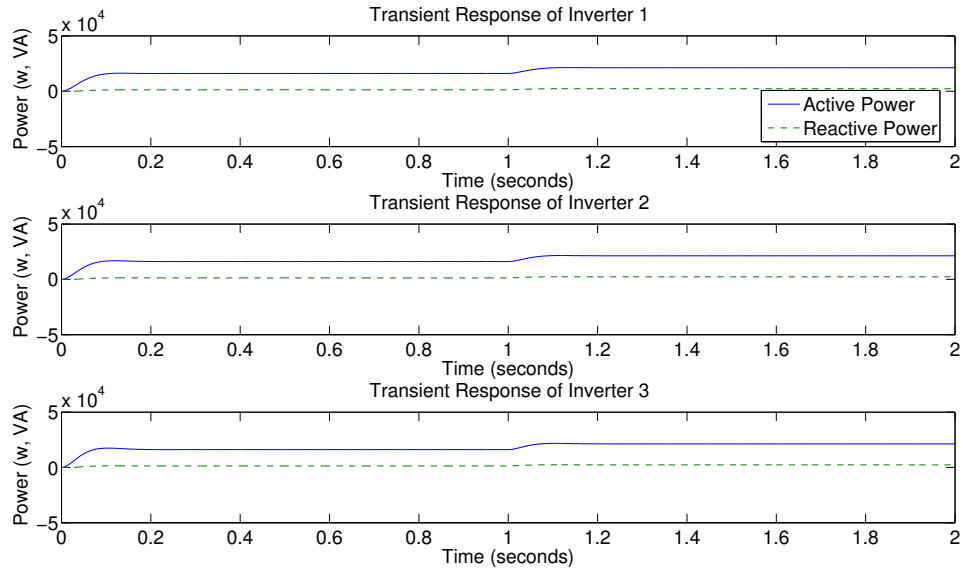


Figure 4.24: Transient power response of inverters 1 – 3 in the alternative configuration of the nine-inverter microgrid shown in Figure 4.23. Each inverter uses a Glover McFarlane loopshaping controller.

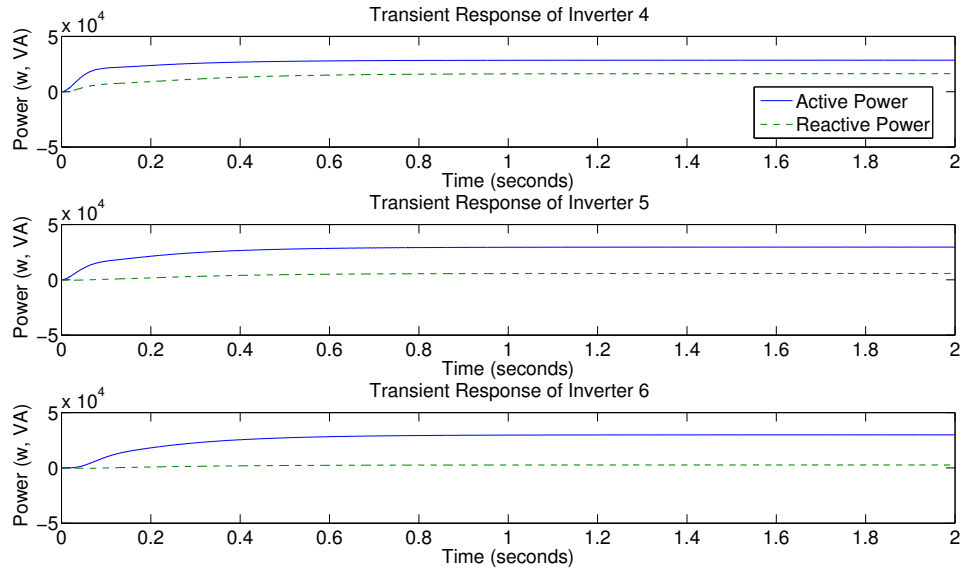


Figure 4.25: Transient power response of inverters 4 – 6 in the alternative configuration of the nine-inverter microgrid shown in Figure 4.23. Each inverter uses a Glover McFarlane loopshaping controller.

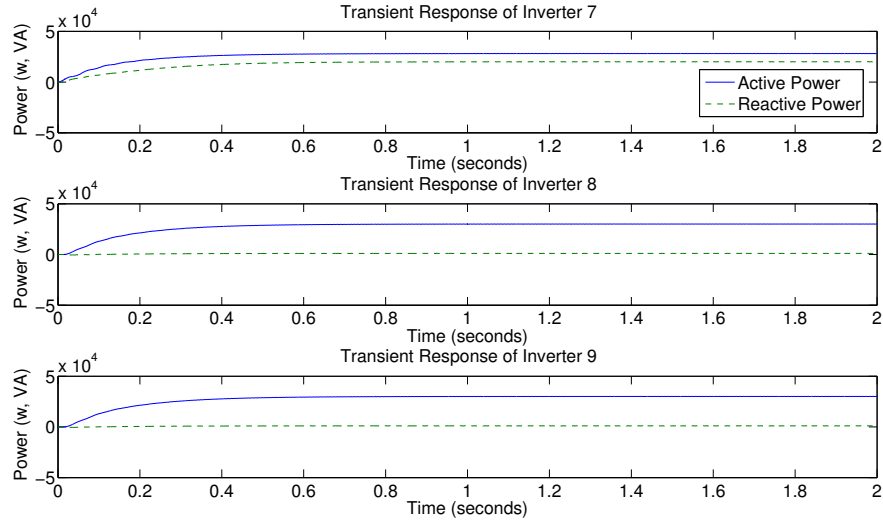


Figure 4.26: Transient power response of inverters 7 – 9 in the alternative configuration of the nine-inverter microgrid shown in Figure 4.23. Each inverter uses a Glover McFarlane loopshaping controller.

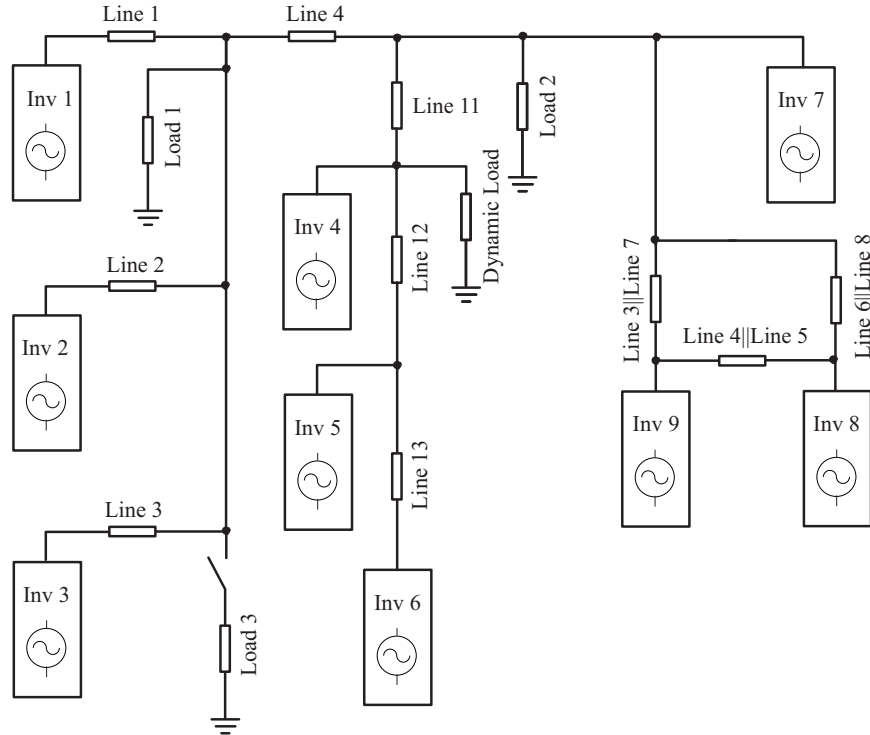


Figure 4.27: Nine inverter microgrid with dynamic load.

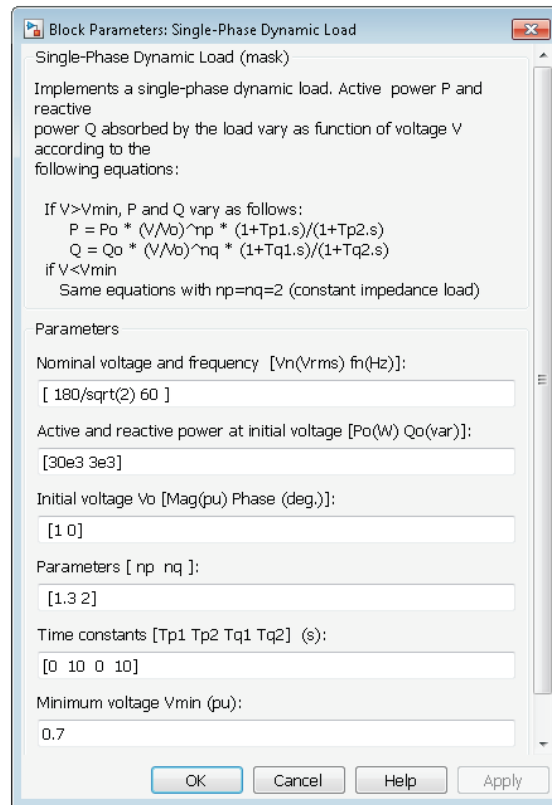


Figure 4.28: Parameters for dynamic load for the system shown in Figure 4.27.

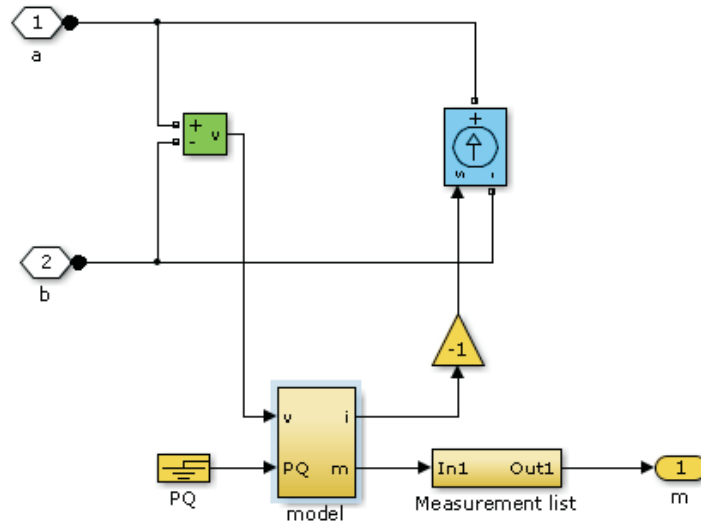


Figure 4.29: Top level for dynamic load model used in the system shown in Figure 4.27.

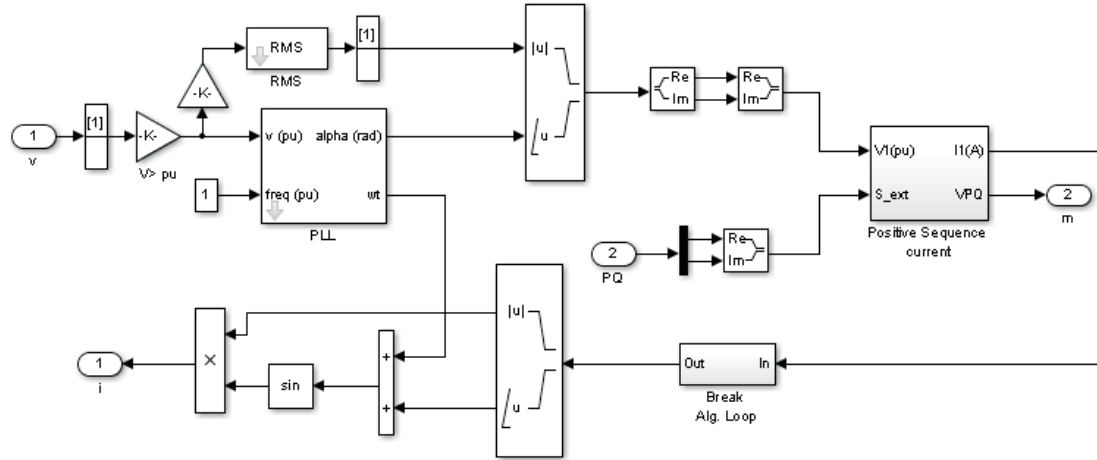


Figure 4.30: Model for dynamic load for the system shown in Figure 4.29. Note that the top level of the model is shown in Figure 4.29 and this figure is the contents of the “model” block in the same figure.

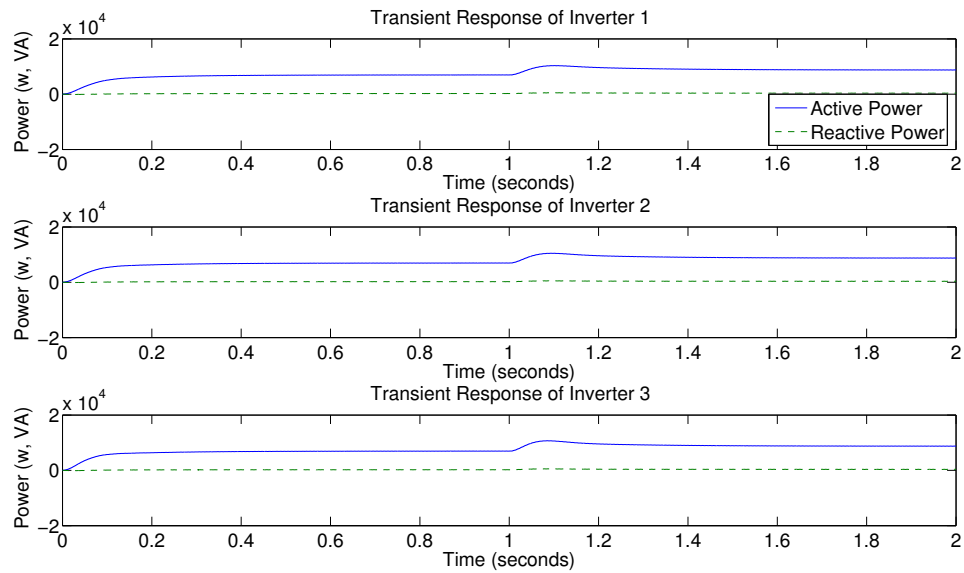


Figure 4.31: Transient power response of inverters 1-3 as shown in Figure 4.27.

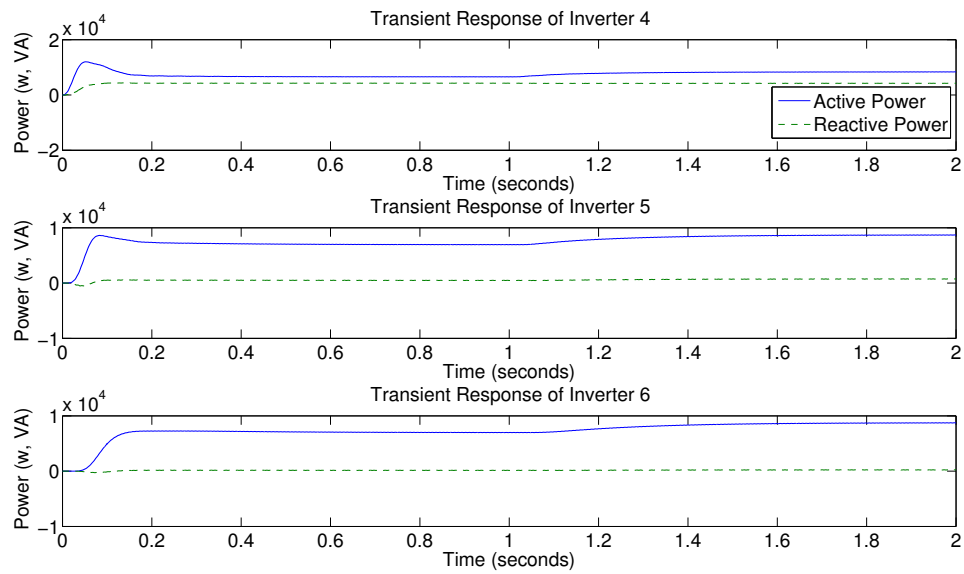


Figure 4.32: Transient power response of inverters 1-3 as shown in Figure 4.27.

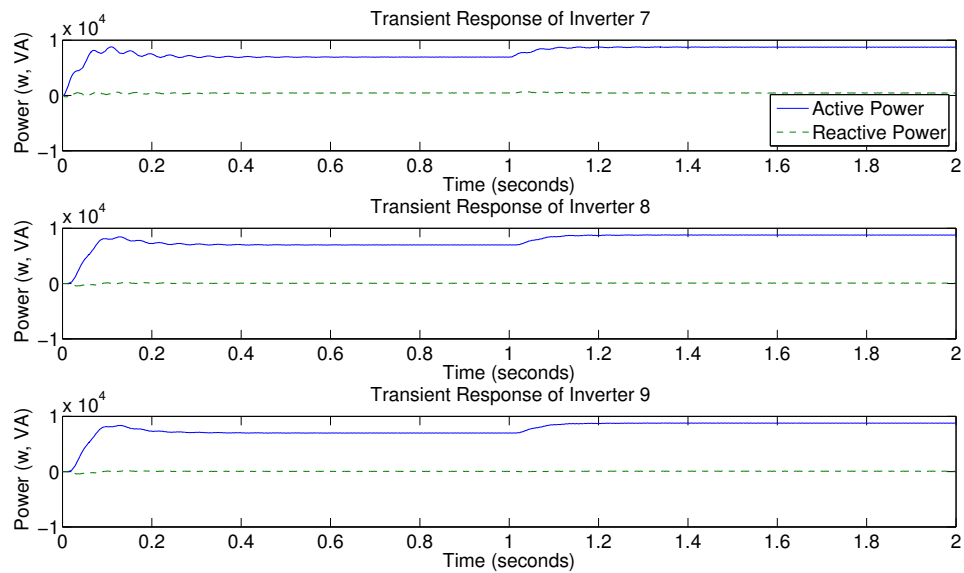


Figure 4.33: Transient power response of inverters 1-3 as shown in Figure 4.27.

Chapter 5

GAIN SCHEDULED CONTROLLER SYNTHESIS

5.1 Gain Scheduling Based on Line Phase

The dependence of the control law on the angle of the complex line impedance was introduced in Section 1.4 and is discussed in greater detail in this chapter. Consider the system shown in Figure 5.1.

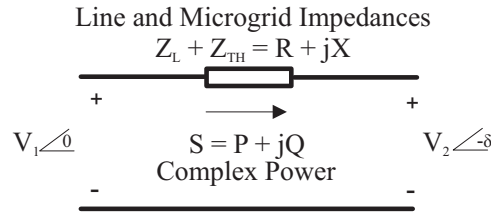


Figure 5.1: Two inverter system.

The fundamental relationships relating system voltage and phase to active and reactive power are given as (5.1) and (5.2).

$$V_2 \sin(\delta) = \frac{XP - RQ}{V_1} \quad (5.1)$$

$$V_1 - V_2 \cos(\delta) = \frac{RP + XQ}{V_1} \quad (5.2)$$

If one assumes $X \gg R$ and $\delta \ll 1$, the relationships may be simplified to (5.3) and (5.4).

$$\delta \simeq \frac{XP}{V_1 V_2} \quad (5.3)$$

$$V_1 - V_2 \simeq \frac{XQ}{V_1} \quad (5.4)$$

Alternatively, if one assumes $R \gg X$ and $\delta \ll 1$, the relationships may be simplified to (5.5) and (5.6).

$$\delta \simeq -\frac{RQ}{V_1 V_2} \quad (5.5)$$

$$V_1 - V_2 \simeq \frac{RP}{V_1} \quad (5.6)$$

Conventional droop control is based on several assumptions such as the output impedance having negligible effect on the power characteristic (output impedance is small compared to line impedance) and there is no cross coupling in the $P - \omega$ or $Q - V$ relationships. It is clear, however, that the assumptions made can significantly influence the appropriate control law. One way these issues are addressed is by applying a linear rotational transformation matrix and modifying the control law [16]. The linear rotational transformation is applied as (5.7).

$$\begin{pmatrix} P' \\ Q' \end{pmatrix} = \begin{pmatrix} \sin(\theta) & -\cos(\theta) \\ \cos(\theta) & \sin(\theta) \end{pmatrix} \begin{pmatrix} P \\ Q \end{pmatrix} \quad (5.7)$$

Where $\theta = \tan^{-1}(X/R)$ is the angle of the complex line impedance.

The transformed power quantities P' and Q' , are then used in the power relationships (5.8) and (5.9).

$$\delta \simeq \frac{ZP'}{V_1 V_2} \quad (5.8)$$

$$V_1 - V_2 \cos(\delta) \simeq \frac{ZQ'}{V_1} \quad (5.9)$$

For $\delta \ll 1$ the droop control laws may be expressed as (5.10) and (5.11).

$$\omega - \omega_0 = -k_p(P' - P'_0) \quad (5.10)$$

$$V - V_0 = -k_v(Q' - Q'_0) \quad (5.11)$$

This approach may be implemented with CGDC or GMFDC as shown in Figure 5.2.

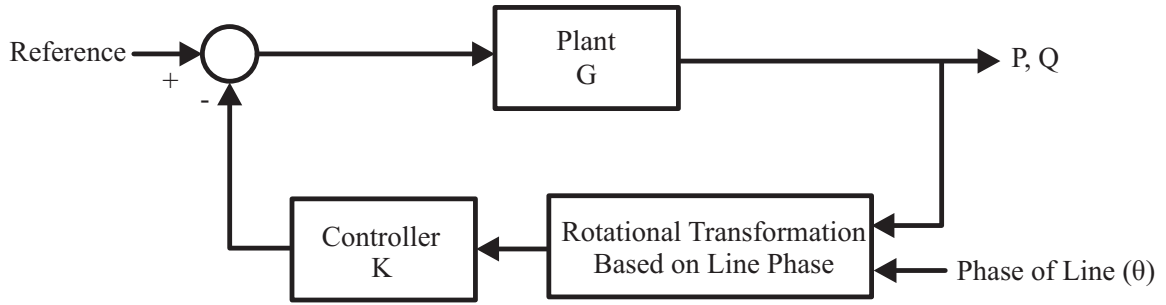


Figure 5.2: Implementation of the rotational transformation based on line impedance.

This approach may be implemented a number of ways, namely estimating the line phase, or assuming a given line phase for grid connected and islanded modes and switching the assumed impedance using an island detection scheme. Gain scheduling based on the phase of a complex line impedance may enhance performance by a limited degree. This is because the magnitude of the line impedance can change, the inverter or PCC voltages can change, and the relative angle of the inverter and PCC voltages can change. To address these issues the plant may be modeled as a parameter varying system and a polytopic controller synthesized. These topics are addressed in the following sections.

5.2 Polytopic and Affine System Models

To design a gain scheduled GMFDC, the system must be modeled as an affine or polytopic system. The analytical system model was derived in detail in Section 2.3 and is

repeated in this section for clarity. This model is further generalized in (5.12), (5.13), and (5.14). It is important to note that changes in the system parameters only effect the “C” matrix in the state space representation. The family of models that result from varying system conditions will therefore only appear in the stated matrix.

$$\begin{pmatrix} \Delta P(s) \\ \Delta Q(s) \end{pmatrix} = \begin{pmatrix} \frac{1421C_1}{s(s^2+53.32s+1421)} & \frac{1421C_2}{s^2+53.32s+1421} \\ \frac{1421C_3}{s(s^2+53.32s+1421)} & \frac{1421C_4}{s^2+53.32s+1421} \end{pmatrix} \begin{pmatrix} \Delta\omega \\ \Delta V \end{pmatrix} \quad (5.12)$$

$$\dot{x} = \begin{pmatrix} 0 & 1 & 0 & 0 & 0 \\ 0 & 0 & 1 & 0 & 0 \\ 0 & -1421 & -53.32 & 0 & 0 \\ 0 & 0 & 0 & 0 & 1 \\ 0 & 0 & 0 & -1421 & -53.32 \end{pmatrix} x + \begin{pmatrix} 0 & 0 \\ 0 & 0 \\ 1 & 0 \\ 0 & 0 \\ 0 & 1 \end{pmatrix} \begin{pmatrix} \Delta\omega \\ \Delta V \end{pmatrix} \quad (5.13)$$

$$\begin{pmatrix} \Delta P \\ \Delta Q \end{pmatrix} = \begin{pmatrix} 1421C_1 & 0 & 0 & 1421C_2 & 0 \\ 1421C_3 & 0 & 0 & 1421C_4 & 0 \end{pmatrix} x \quad (5.14)$$

Polytopic Representations

The time varying system given by (5.15) and (5.16) (in block form in (5.18)) may be represented as a polytopic system. Polytopic representations are used to represent time varying systems that vary within a convex hull (polytope) in (5.19).

$$E(t)\dot{x} = A(t)x + B(t)u \quad (5.15)$$

$$y = C(t)x + D(t)u \quad (5.16)$$

Where:

$$A(t) + jE(t) \in Co \left\{ \sum_{i=1}^n A_i + jE_i \right\} \quad (5.17)$$

$$S(t) = \begin{pmatrix} A(t) + jE(t) & B(t) \\ C(t) & D(t) \end{pmatrix} \quad (5.18)$$

$$S(t) \in \left\{ \sum_{i=1}^k \alpha_i S_i : \alpha_i \geq 0, \sum_{i=1}^k \alpha_i = 1 \right\} \quad (5.19)$$

Where S_i are the vertices of the system and α_i are the polytopic coordinates.

The system is quadratically stable if (5.20)-(5.22) are satisfied [1].

$$A_i Q E_j^T + E_j Q A_i^T + A_j Q E_i^T + E_i Q A_j^T < 2t_{ij}I, \quad \forall i, j \in \{1..n\} \quad (5.20)$$

$$Q > I \quad (5.21)$$

$$\begin{pmatrix} t_{11} & \cdots & t_{1n} \\ \vdots & \ddots & \vdots \\ t_{1n} & \cdots & t_{nn} \end{pmatrix} < 0 \quad (5.22)$$

Affine Representations

Affine representations are used to represent systems that have an affine dependance on time varying parameters. For example, the system (5.23) and (5.24) (in block form in (5.31)) may be represented as an affine system using (5.25)-(5.29).

$$E(p)\dot{x} = A(p)x + B(p)u \quad (5.23)$$

$$y = C(p)x + D(p)u \quad (5.24)$$

Where $p = (p_1, \dots, p_n)$ and the following:

$$A(p) = A_0 + \sum_{i=1}^n p_i A_i \quad (5.25)$$

$$B(p) = B_0 + \sum_{i=1}^n p_i B_i \quad (5.26)$$

$$C(p) = C_0 + \sum_{i=1}^n p_i C_i \quad (5.27)$$

$$D(p) = D_0 + \sum_{i=1}^n p_i D_i \quad (5.28)$$

$$E(p) = E_0 + \sum_{i=1}^n p_i E_i \quad (5.29)$$

Similarly, (5.30) may be expressed as (5.31).

$$S(p) = \begin{pmatrix} A(p) + jE(p) & B(p) \\ C(p) & D(p) \end{pmatrix} \quad (5.30)$$

$$S(p) = S_0 + \sum_{i=1}^n p_i S_i \quad (5.31)$$

Where $p_i(t) \in [p_{i_{\min}}, p_{i_{\max}}]$.

Let the extreme values of $p_i(t)$ denote system vertices ξ_v for $v = 2..2^n$.

The system is quadratically stable if there exist symmetric matrices Q and $\{M_v\}_{v=2}^{2^n}$ such that (5.32)-(5.35) are satisfied [1].

$$A(\xi_v)QE(\xi_v)^T + E(\xi_v)QA(\xi_v)^T + \Sigma_v \xi_v^2 M_v < 0, \quad \forall \xi_v \quad (5.32)$$

$$A_v P E_v^T + E_v P A_v^T + M_v \geq 0, \quad \forall v \quad (5.33)$$

$$M_v \geq 0 \quad (5.34)$$

$$Q > I \quad (5.35)$$

Quadratic Stability

The quadratic stability test may be implemented in Matlab using the function “quadstab” for polytopic systems with arbitrarily fast time variations or affine systems with user specified time variations. The function may also be used with affine representations of the system to determine the maximum region for which the system is quadratically stable. Less conservative estimates of stability may be determined using the Matlab function “pdlstab” which uses parameter dependent Lyapunov functions and assumes the system is time invariant. This is a reasonable approximation for slowly varying systems.

5.3 The Family of Plants

A family of plants may be established by considering the values assumed by constants $C_{1,2,3,4}$ in (5.14). This family is defined by the extreme values of the noted constants. A typical example of a given system with uncertainty factor “ Δ ” is shown in Table 5.1.

5.4 Synthesis of Gain Scheduled Glover McFarlane Controller

Two approaches were used to synthesize gain scheduled Glover McFarlane controllers (gs GMFDC). In the first approach the Matlab function “hinfgs” was used, however, this function is difficult to use, particularly when a specific DC gain is needed. The second approach was to synthesize GMFDC for each vertex and check stability of the

Table 5.1: Two uncertainty descriptions for a family of plants.

Parameter	Parameter Values
V_{INV}	$170(1 \pm \Delta) V_{\text{peak}}$
V_{PCC}	$179(1 \pm \Delta) V_{\text{peak}}$
$ Z_L $	$0.1(1 \pm \Delta) \Omega$
$\angle Z_L$	$\pi/2(1 - 2\Delta) \text{ rad}$
δ	$0.1(1 \pm \Delta) \text{ rad}$

complete system using parameter dependent Lyapunov functions. This approach was much easier to obtain the desired results and is the only approach considered in this report.

The uncertainty description used to synthesize the gs GMFDC is given in Table 5.1 with 30% uncertainty in the line impedance, line phase, and phase angle between sources. The uncertainty in inverter and microgrid voltages was assumed to be approximately 4%. The four parameters used to schedule the gs GMFDC, $C_1 - C_4$, are expressed in (5.36) as discussed in Section 5.2. These values may be calculated directly for a system with two sources or estimated using system ID for larger systems¹. In the interest of focusing solely on gs GMFDC, this treatment is limited to systems with two sources.

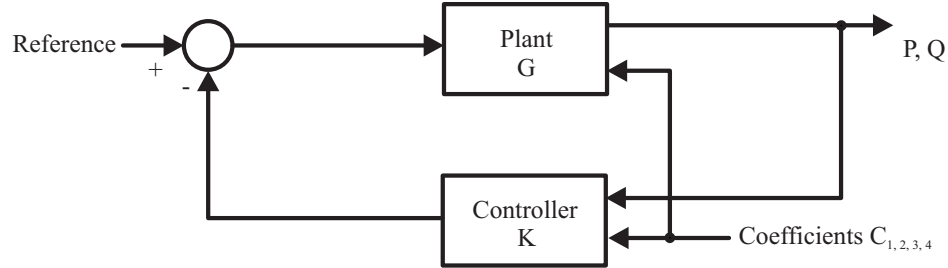


Figure 5.3: Block diagram of linear parameter dependent system and gs GMFDC controller implemented in Simulink.

¹One also has the option of testing the gs GMFDC in closed loop with arbitrarily defined coefficients. This may result in conditions that are not physically realizable, but an excellent way to test the capabilities of the controller.

$$\begin{pmatrix} \Delta P(s) \\ \Delta Q(s) \end{pmatrix} = \begin{pmatrix} \frac{1421C_1}{s(s^2+53.32s+1421)} & \frac{1421C_2}{s^2+53.32s+1421} \\ \frac{1421C_3}{s(s^2+53.32s+1421)} & \frac{1421C_4}{s^2+53.32s+1421} \end{pmatrix} \begin{pmatrix} \Delta\omega \\ \Delta V \end{pmatrix} \quad (5.36)$$

A simulation was run using a single inverter connected to a sinusoidal source using an inductive impedance of $j0.1\Omega$ at 377 rad/s. The sinusoidal source (representing the microgrid point of common coupling (PCC)) was subjected to a 2 rad/s perturbation in frequency and a 2V perturbation in voltage. The coefficients $C_1 - C_4$ were calculated in real time and are shown in Figure 5.4. The transient PQ responses of systems with a CGDC, GMFDC, and gs GMFDC are shown in figures 5.5, 5.6, and 5.7 respectively. From these transient plots one can see a clear improvement for increasing controller complexity.

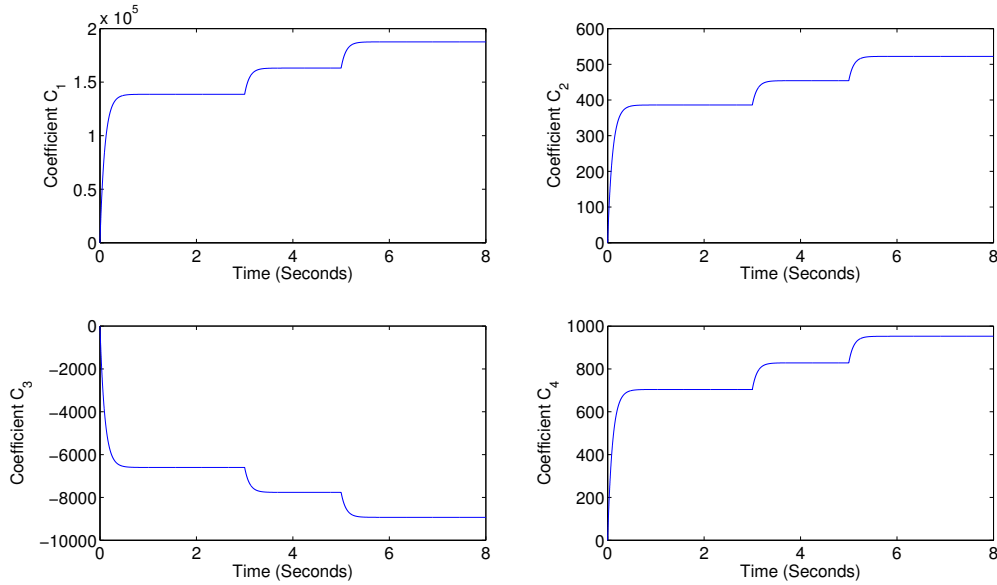


Figure 5.4: Plot of the plant coefficients as shown in Figure 5.3.

It is interesting to note the behavior of the plant and gain scheduled controller over time. Several “snapshots” are shown for the plant and controller in figures 5.8 and 5.9 respectively. One will note that there does not appear to be a significant change in either

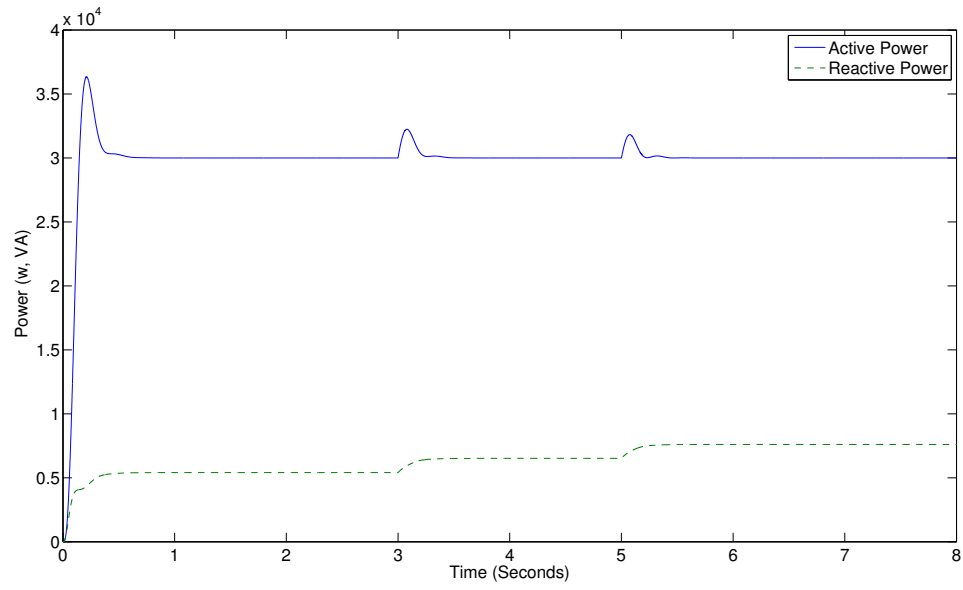


Figure 5.5: Transient PQ response of parameter dependent system in Figure 5.3. This plot is for a parameter dependent system with a CGDC.

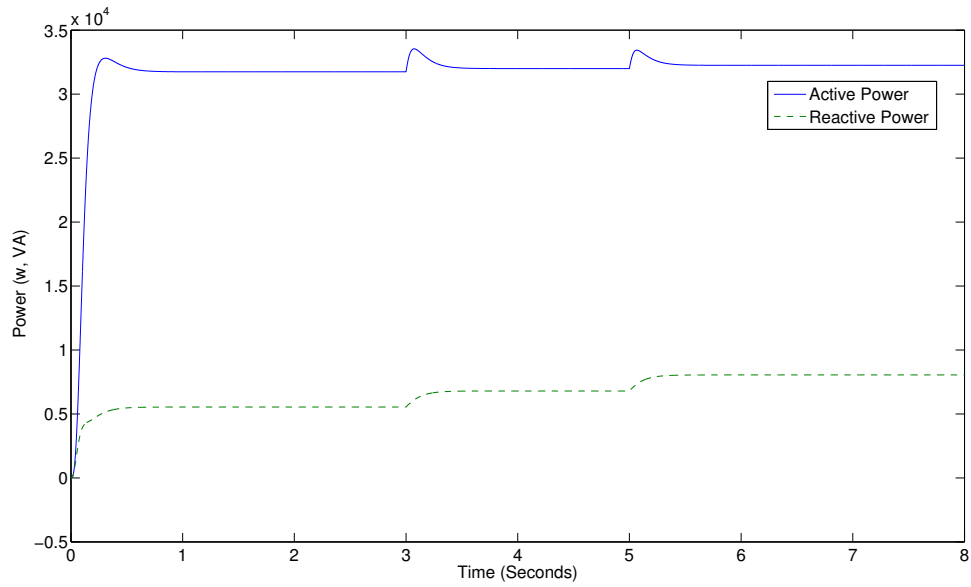


Figure 5.6: Transient PQ response of parameter dependent system in Figure 5.3. This plot is for a parameter dependent system with a GMFDC.

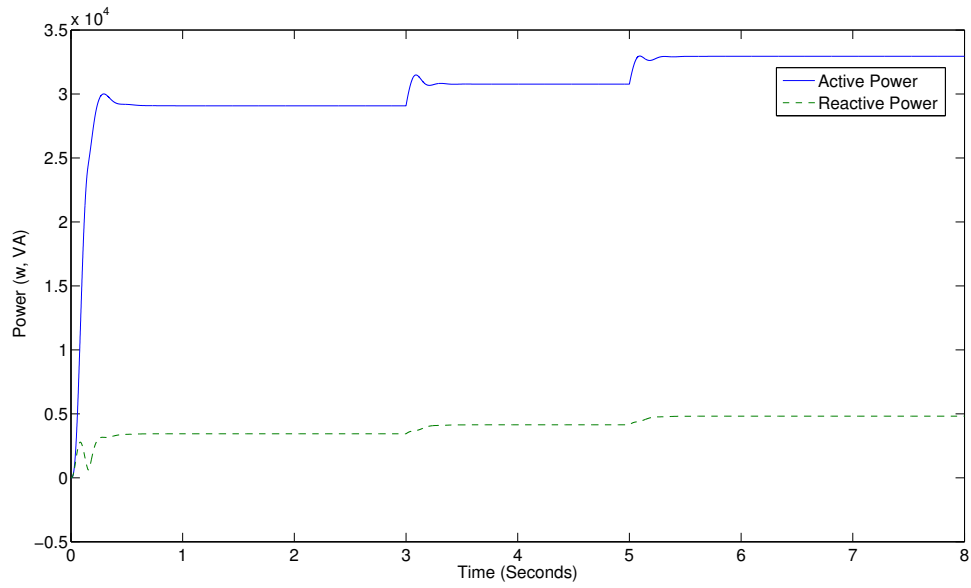


Figure 5.7: Transient PQ response of parameter dependent system in Figure 5.3. This plot is for a parameter dependent system with a gain scheduled GMFDC.

the plant or the controller over time. This is due to the fact that the snapshots occur during steady state and the fluctuations are much more apparent during transient conditions as shown for the plant and controller in Figure 5.10 and Figure 5.11 respectively.

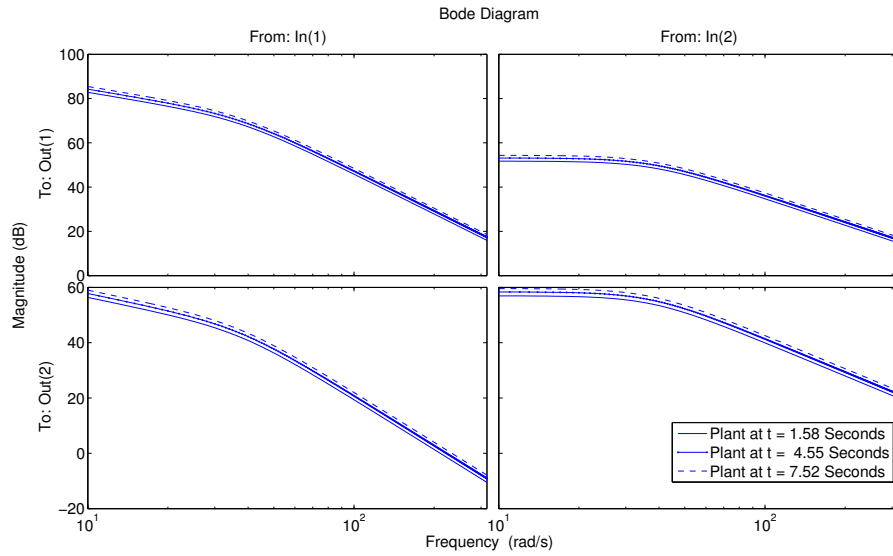


Figure 5.8: This figure contains Bode magnitude plots for the system at several instants in time. These Bode plots may be thought of as “snapshots” of the plant magnitude response as the system evolves over time. Corresponding “snapshots” of the gain scheduled controller are contained in Figure 5.9.

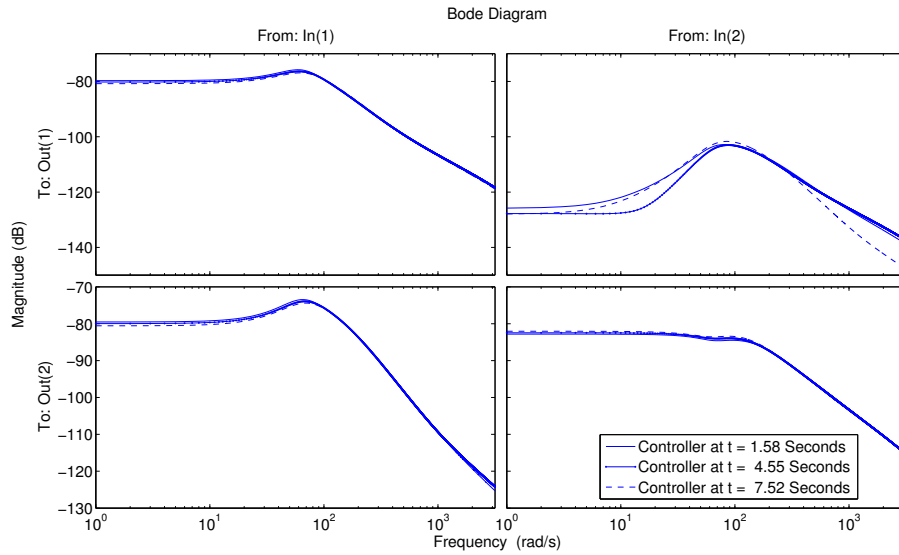


Figure 5.9: This figure contains Bode magnitude plots for the gain scheduled controller at several instants in time. These Bode plots may be thought of as “snapshots” of the controller magnitude response as the system evolves over time. Corresponding “snapshots” of the plant are contained in Figure 5.8.

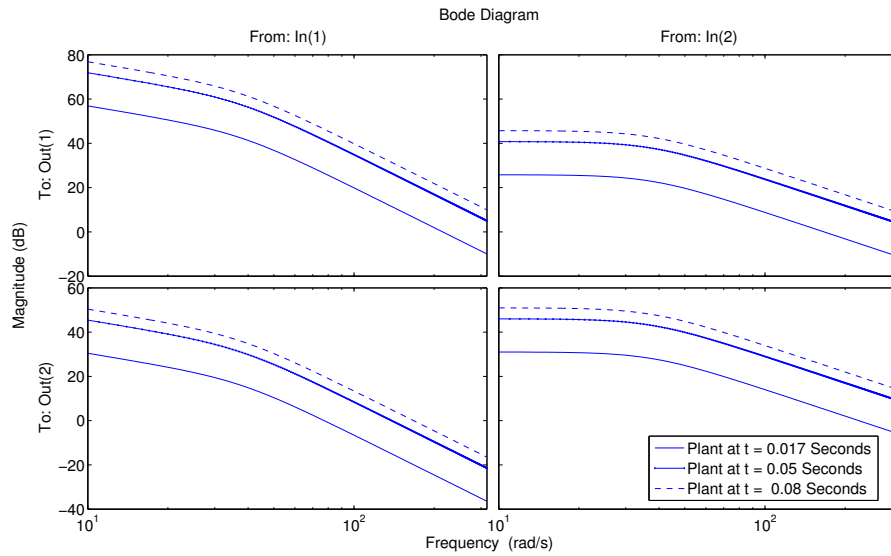


Figure 5.10: This figure contains Bode magnitude plots for the plant at several instants in time. These Bode plots may be thought of as “snapshots” of the controller magnitude response as the system evolves over time.

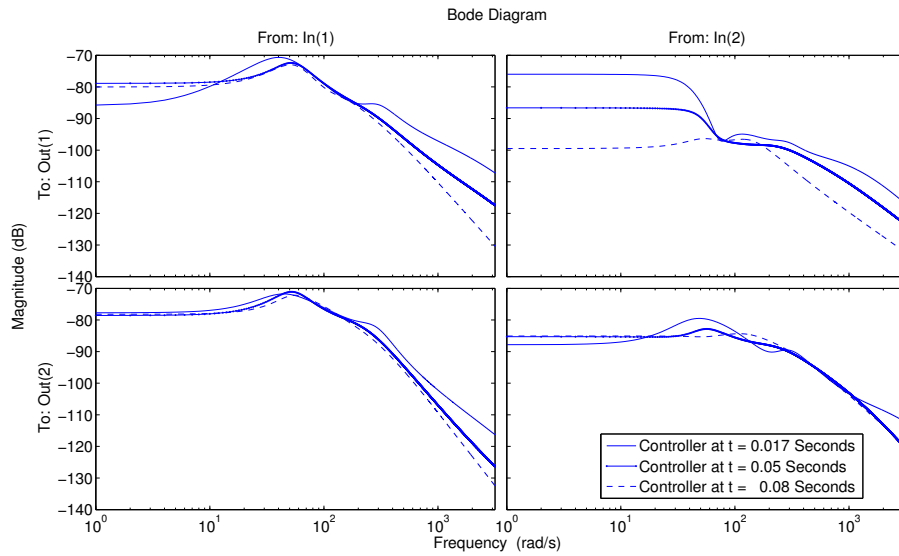


Figure 5.11: This figure contains Bode magnitude plots for the gain scheduled controller at several instants in time. These Bode plots may be thought of as “snapshots” of the controller magnitude response as the system evolves over time.

5.5 Bumpless Control

Bumpless controllers have appeared in the literature as an ad-hoc adaptive control scheme. The approach is less conservative, easier to synthesize, and easier to implement than a gain scheduled polytopic controller or other interpolation scheme [8], and has a larger operating range than a nominal controller [23], [42]. The fundamental paradigm of bumpless control is to identify the salient parameters of a system, synthesize controllers based on these parameter values, and switch between controllers as one moves through the parameter space. If this is done using conventional controllers as shown in Figure 5.12, then there will be discontinuities at the controller outputs (plant input) when switching between controllers as shown in Figure 5.13.

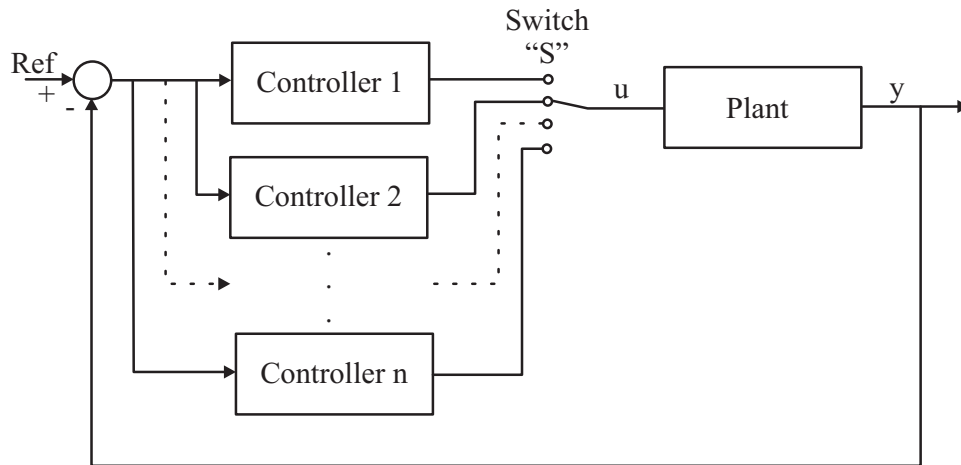


Figure 5.12: Plant with a set of “ n ” conventional, “bumpy” controllers. These plants are bumpy since switching between them will result in discontinuities at the plant input.

The “bumpless” in bumpless control refers to maintaining the same, or nearly the same, output at each controller regardless of which controller is active. Maintaining the outputs in such a way ensures a smooth transition. A block diagram of a typical system level implementation is shown in Figure 5.14. Each controller in the system is typically implemented as shown in Figure 5.15.

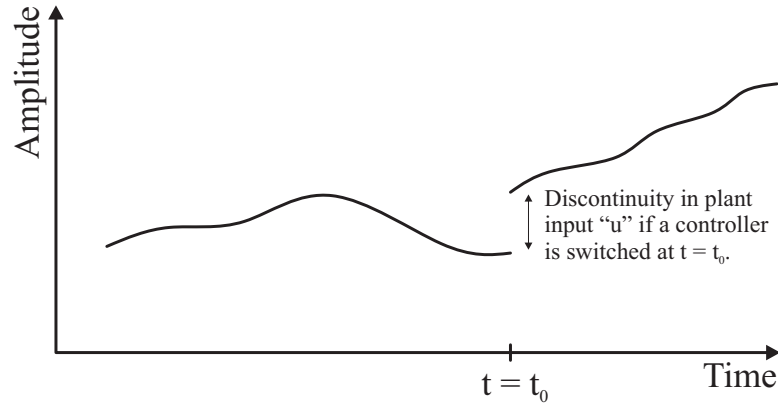


Figure 5.13: Hypothetical transient plot of plant input “u” with a set of conventional, “non-bumpless” controllers. Clearly the discontinuity will perturb the system and create undesirable issues. The purpose of bumpless control is to minimize the discontinuity shown in this figure.

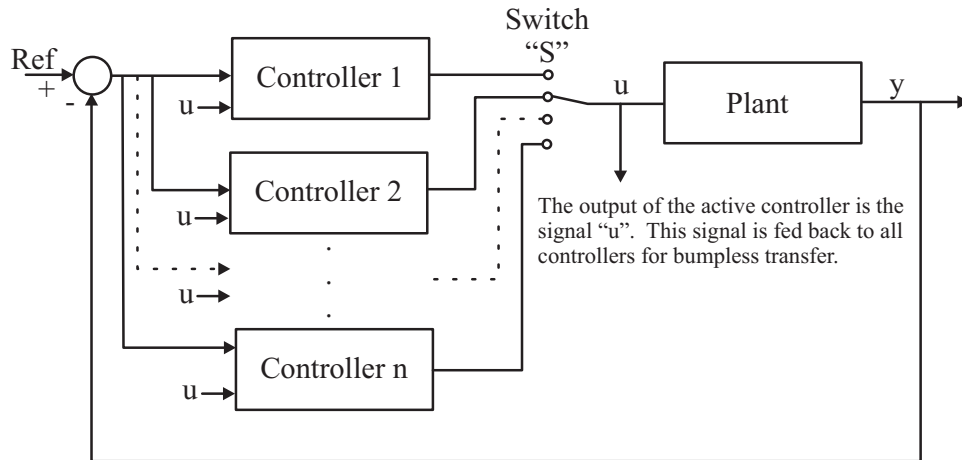


Figure 5.14: Plant with a set of “n” bumpless controllers. These controllers are called bumpless because the discontinuity between controller outputs is negligible.

From this figure one will see that when the controller is not active, the switch “S” is open and the feedback gain “L” is used to drive the output of the controller to the current value at the output. When the controller in Figure 5.15 is active, then the input to the bumpless gain “L” is zero and the active controller functions without any alteration.

To prevent chatter between various controller selections (and possible instability),

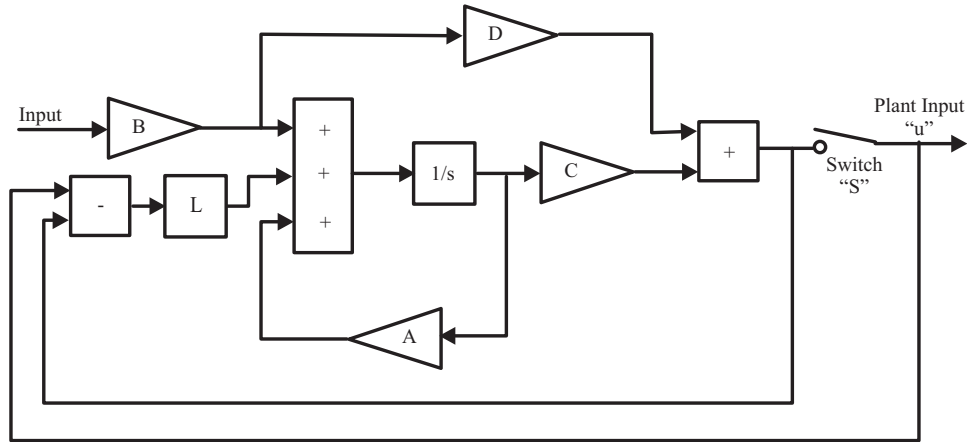


Figure 5.15: Implementation of a bumpless controller. Note that when the controller is not active, the switch “S” is open and the feedback gain “L” is used to drive the output of the controller to the current value of the active controller (not shown) at the output.

one may add hysteresis to the selection parameters. While this is a straightforward task, it becomes unwieldy for systems with a large number of controllers. One will note that if there are “np” parameters there will be $n_v = 2^{np}$ vertices with corresponding controllers. Using hysteresis for switching between these controllers, there will be $n_v(n_v-1)$ hysteresis blocks plus associated logic blocks. The approach taken here comes from a selection of theory from polytopic gain scheduled control is re-appropriated so that hysteresis may be easily incorporated into the selection of bumpless controllers with a significant reduction in complexity.

For example, rather than weight each of the controllers according to the current position of the system in the polytope, only one controller was active at any given time according to the nearest vertex. The nearest vertex was ascertained by continuously determining the largest weight that would be used if a gain scheduled controller was to be implemented.

One may consider the conventional hysteresis approach to have $n_v(n_v-1)$ hysteresis

blocks plus associated logic blocks. The proposed approach may be implemented in a variety of ways using individual blocks or user defined functions making it difficult to define a definite number of required blocks. One may, however, assume that there are $3nv+7$ blocks. Thus, the proposed approach shows a clear reduction in complexity for systems with six or more controllers. A system with three parameters where each parameter has a given minimum and maximum has $2^3 = 8$ vertices with one controller per vertex. One may see how quickly the number of controllers increases with the number of system parameters and the resulting problem simplification.

Representing the Scheduling Parameters in Polytopic Coordinates and Controller Selection

The parameters used to schedule a bumpless controller may be visualized using the system representation in (5.37) and represented in polytopic coordinates as (5.38). In this representation the extreme values of the system are represented by the system vertices $(A_v, B_v, C_v, D_v)|_{v=1}^{nv}$ and weighted according to the current position $\alpha_v(t)|_{v=1}^{nv}$. The polytopic coordinates provide a convenient framework to select a controller since the coordinate with the largest value (weight) represents the nearest vertex of the polytope. The designer may then use these weights to select the controller at the closest vertex.

$$\begin{pmatrix} A(p(t)) & B(p(t)) \\ C(p(t)) & D(p(t)) \end{pmatrix} = \sum_{v=1}^{nv} \alpha_v(t) \begin{pmatrix} A_v & B_v \\ C_v & D_v \end{pmatrix} \quad (5.37)$$

Where $\alpha_v(t)$ is solved using the recursive relationship for $\beta_i(t)$:

$$\begin{aligned}\beta_i(t) &= [\beta_{i-1}(t)(1-t_i(t)) \quad \beta_{i-1}(t)t_i(t)] \\ t_i(t) &= \frac{p_i(t) - p_{i \min}}{p_{i \max} - p_{i \min}} \\ i &= 1, \dots, np\end{aligned}\tag{5.38}$$

One should note that $\beta_0 = 1$, p_i refers to real-time values of parameter number “i”, $p_{i \max, \min}$ refer to extreme values in the set of possible values for parameter number “i”, $\alpha_v(t)$ weights controllers at each vertex according to the real-time values for the system parameters p_i . Solving β_i for “np” parameters results in $n_v = 2^{np}$ entries ($\beta_{np}(t) = [\alpha_1(t), \dots, \alpha_{n_v}(t)]$), one for each system vertex. These entries are used to weight the controllers in (5.37).

As stated in the first section of this chapter, incorporating hysteresis into the selection of bumpless controllers can become unwieldily for systems with more than a few controllers. To address this issue, the approach shown in Figure 5.16 may be used to greatly reduce the number of required elements.

Simulation Example

While the advantage of the proposed approach is in the implementation of a large number of controllers, it is necessary to limit the number of controllers to four so that two dimensional plots may be used. In this section an example with two sets of parameter trajectories. The first set of parameter trajectories is shown in Figure 5.17. Each of the two parameters is linearly varying in time such that a diamond shape is traversed counter-clockwise in time. A deadzone value of 0.3 is used such that the enable signal for choosing the controller at the nearest vertex and corresponding polytopic coordinates are shown in Figure 5.18. One will note that the enable signal only allows a controller to be selected when there is a clear advantage of one controller over another as specified by the

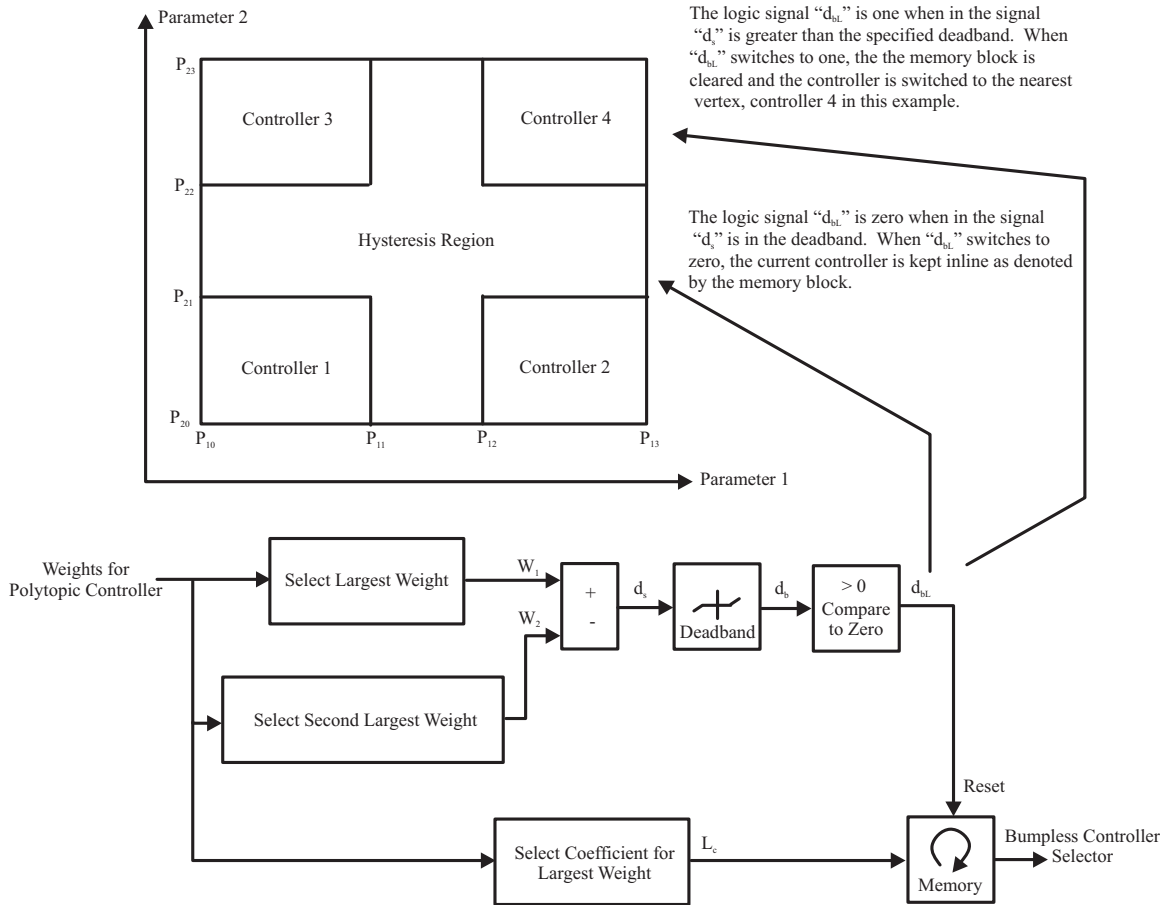


Figure 5.16: This block diagram illustrates the selection of a bumpless controller based on the distance between vertices in a polytope. The selection is based on the nearest vertex in a polytope. When the difference between the nearest vertex and second nearest vertex is less than a specified value then one may say that the vertices are equidistant or nearly equidistant. Under such conditions chatter may occur, thus the deadband and memory blocks simply and easily incorporate hysteresis to eliminate such issues.

deadband and polytopic coordinates. Disallowing controllers of nearly equal distance in polytopic coordinates eliminates chatter assuming the proper deadzone (and resulting hysteresis) are specified.

An example of one linearly varying parameter and one parameter with a discontinuity is shown in Figure 5.19. In this set of parameter trajectories a “backwards c” shape is traversed counterclockwise in time. As in the previous set of parameter

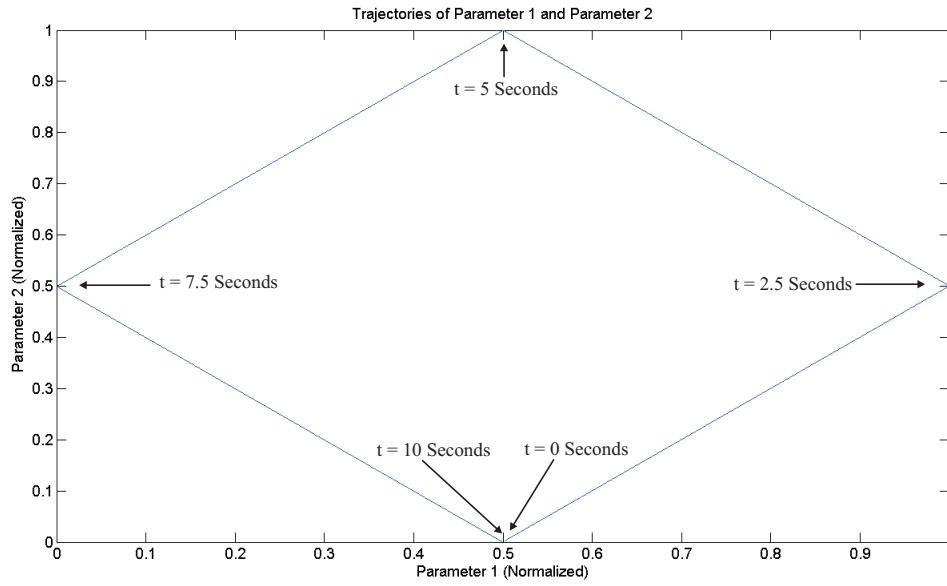


Figure 5.17: Parametric plot of normalized parameter trajectories. Note the trajectory of the parameters is counterclockwise in time from 0 seconds to 10 seconds.

trajectories, a deadzone value of 0.3 is used such that the enable signal for choosing the controller at the nearest vertex and corresponding polytopic coordinates are shown in Figure 5.20. Note that a discontinuity in parameter trajectory results in a discontinuity in the enable signal for selecting a controller. This is to be expected as the controller must be switched for such trajectories in the polytope.

If one wishes to incorporate a dependence on time in the selection of a controller, such as a rate limiter or filter to prevent noise from causing erroneous switching events, a single rate limiter or filter may be added following the “Compare to Zero” block. Doing so further reduces the system complexity by a factor of “n” for a system with that many controllers.

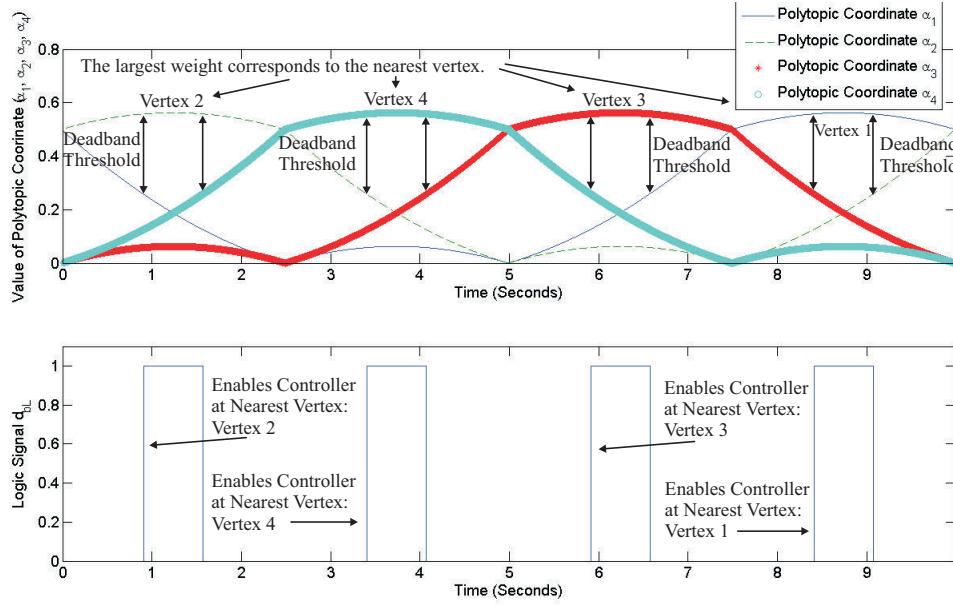


Figure 5.18: Plot of polytopic coordinates and enable signal to select the nearest vertex. The state of the logic signal in time ensures that the controller selection will not chatter between controllers. For this example the deadband threshold is selected as 0.3 and is the distance between the maximum weight and second largest weight in order for a switching event to occur.

Application to an Inverter

The bumpless controller theory presented in this section was applied to the polytopic controller example in Section 5.4. The controllers were the same and the only difference being the selection criteria and bumpless feedback (inner loop within a given controller). The PQ transient response using sixteen bumpless controllers is shown in Figure 5.21. Comparing the response of the bumpless controllers in Figure 5.21 to that of the polytopic controller in Figure 5.7 in section 5.4, it can be seen that the bumpless controllers provide comparable transient performance and are much easier to implement.

In the interest of further simplification, a set of four bumpless controllers were synthesized and scheduled according to coefficients C_1 and C_4 in the model (5.36). The

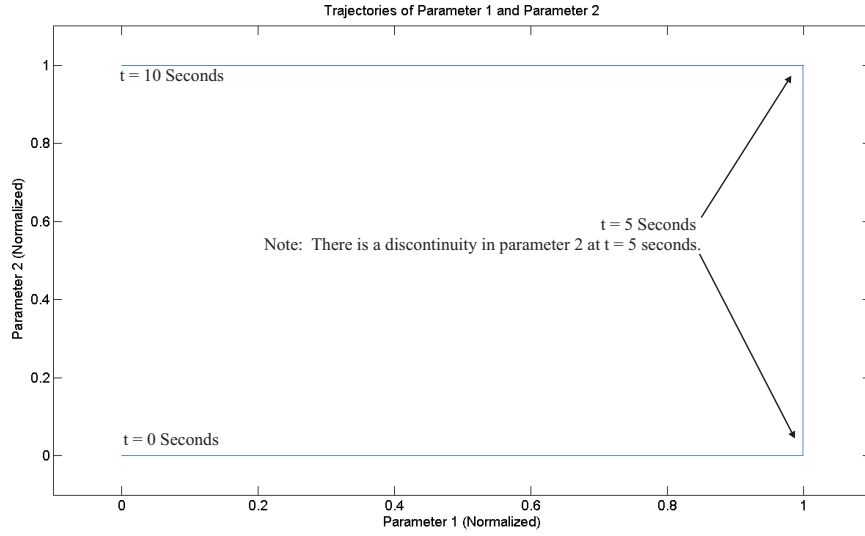


Figure 5.19: Parametric plot of normalized parameter trajectories. Note the trajectory of the parameters is counterclockwise in time from 0 seconds to 10 seconds.

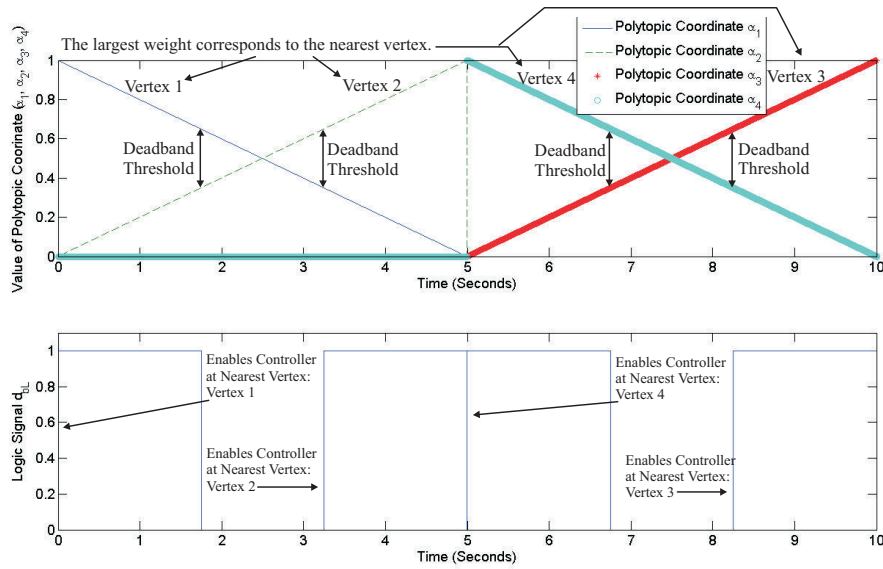


Figure 5.20: Plot of polytopic coordinates and enable signal to select the nearest vertex. The state of the logic signal in time ensures that the controller selection will not chatter between controllers. For this example the deadband threshold is selected as 0.3 and is the distance between the maximum weight and second largest weight in order for a switching event to occur.

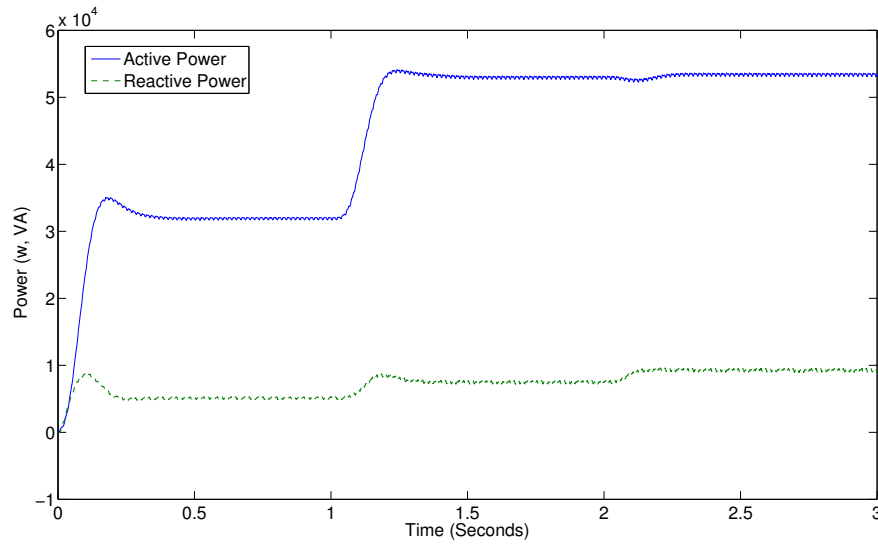


Figure 5.21: Transient active and reactive power response for an inverter using a set of 16 bumpless controllers. The inline controller is chosen according to the nearest vertex (largest weight for the gain scheduled case). The parameters for the system are given in Table 2.3 with a 2 rad/s perturbation at $t = 1$ second and 2 V perturbation at $t = 2$ seconds.

transient response when using four bumpless controllers is shown in Figure 5.22. While the transient response of the system with four bumpless controllers is comparable to the previous case utilizing sixteen bumpless controllers, it stands to reason that there will be tradeoffs in terms of achievable performance and operating range.

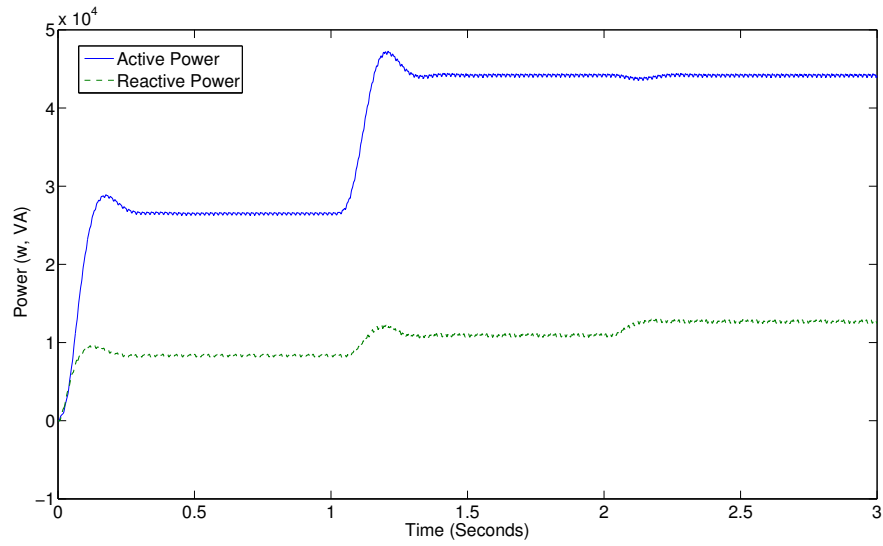


Figure 5.22: Transient active and reactive power response for an inverter using a set of 4 bumpless controllers. The inline controller is chosen according to the nearest vertex (largest weight for the gain scheduled case). The parameters for the system are given in Table 2.3 with a 2 rad/s perturbation at $t = 1$ second and 2 V perturbation at $t = 2$ seconds.

Chapter 6

HARDWARE IMPLEMENTATION

The CGDC and GMFDC described in this thesis were implemented using hardware as outlined in this section. An individual inverter with 5 kw capacity, single phase, 60 V_{RMS} nominal output voltage, 377 rad/s nominal output frequency, was connected to the grid using an auto-transformer. This was done to characterize the inverter and validate the analytical model described in Section 2.3. Then two identical 5 kw, single phase, inverters with 100 V_{RMS} nominal output voltage, 377 rad/s nominal output frequency, were connected in islanded mode as shown in Figure 6.1. This was done to compare the CGDC and GMFDC.

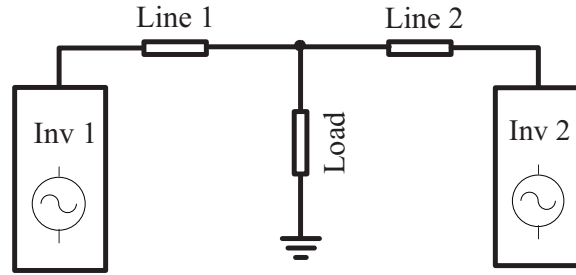


Figure 6.1: Two-inverter configuration used in the hardware implementation.

The implementation uses a TI TMS320LF2808 fixed point 32-bit DSP running at 50 MHz (10 kHz event loop). For digital implementation, continuous time filters and controller were converted to z-domain using the zero-order-hold (ZOH) as outlined in the following sections.

6.1 Power Calculation

Calculation of inverter output power (both active and reactive) is essential to droop control. The approach implemented in hardware is shown in Figure 6.2. The sinusoidal input to the power calculation is the reference voltage generated by the output of the droop

control (a PLL) and the co-sinusoidal input is a “fictitious” output generated using the same PLL. It is called fictitious since it is not actually an output of the inverter, but it would be if the sinusoidal output were delayed in time by the appropriate amount.

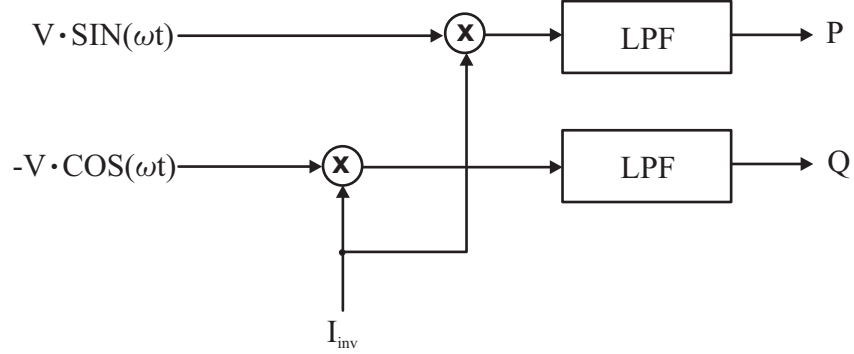


Figure 6.2: Methodology used to calculate the active and reactive inverter output power. Note that the sinusoidal voltage input is assumed to be the output of the droop control and the co-sinusoidal input is derived from the same source.

The low pass filter (LPF) is a second order butterworth filter with a corner frequency of 94 rad/s as given in (6.1) and (6.2) for a 10 kHz sampling rate.

$$F_s = \frac{8883}{s^2 + 133.3s + 8883} \quad (6.1)$$

$$F_z = \frac{4.422 \cdot 10^{-5}z + 4.402 \cdot 10^{-5}}{z^2 - 1.987z + 0.9868} \quad (6.2)$$

6.2 Control Design

The DC gain of both the constant gain and multi-variable controllers is dictated by the voltage and frequency limits and power capacity of a given inverter. Since the power capacity of the inverters are relatively large (5 kw), and there are no frequency or voltage limits in the context of this experiment, DC gains on the order of 10^{-3} were used. In the interest of comparison, controllers were synthesized using the weights (6.3) and (6.6) with the respective DC gains (6.4), (6.5), (6.7), and (6.8).

$$W = \begin{pmatrix} 0.005 & 0 \\ 0 & 0.005 \end{pmatrix} \frac{1}{\left(\frac{s}{20} + 1\right)} \quad (6.3)$$

$$k_p = 2.1 \cdot 10^{-3} \frac{\text{rad}}{s \cdot w} \quad (6.4)$$

$$k_v = 2.7 \cdot 10^{-4} \frac{V}{VA} \quad (6.5)$$

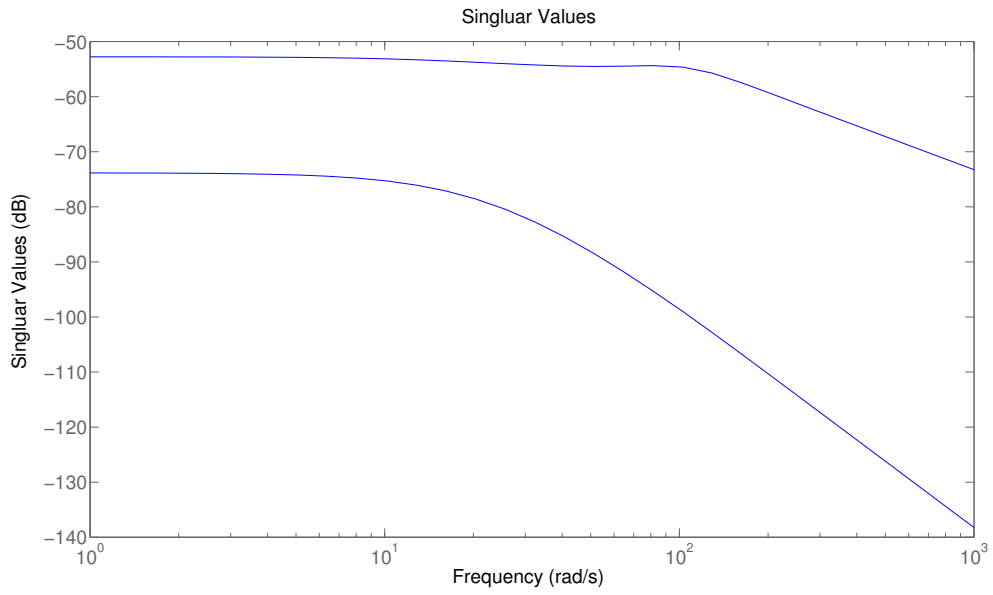


Figure 6.3: Sigma plot of the controller synthesized using the weight (6.3).

$$W = \begin{pmatrix} 0.01 & 0 \\ 0 & 0.01 \end{pmatrix} \frac{1}{\left(\frac{s}{20} + 1\right)} \quad (6.6)$$

$$k_p = 3.5 \cdot 10^{-3} \frac{\text{rad}}{\text{s} \cdot \text{w}} \quad (6.7)$$

$$k_v = 1.4 \cdot 10^{-3} \frac{\text{V}}{\text{VA}} \quad (6.8)$$

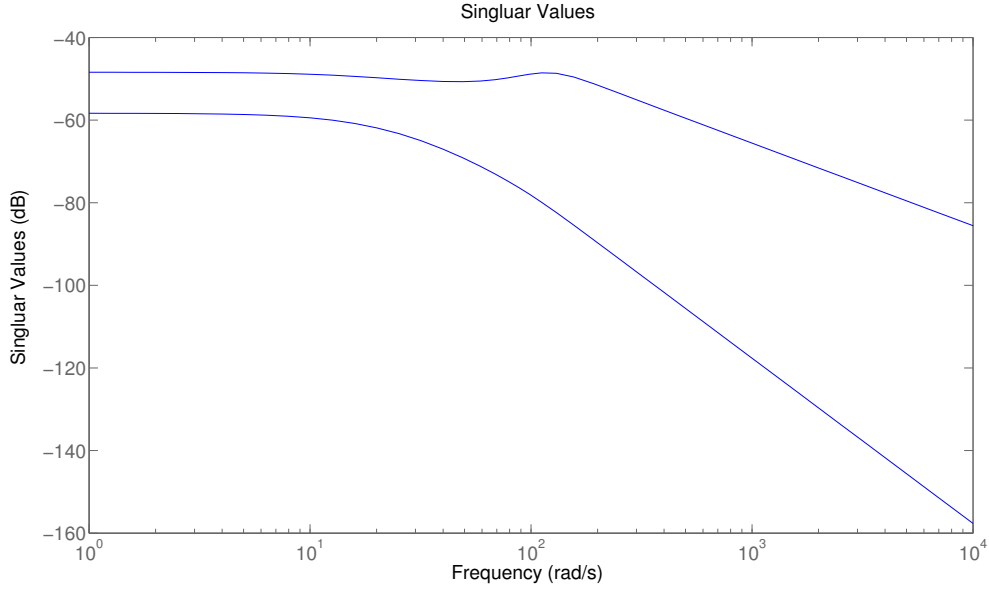


Figure 6.4: Sigma plot of the controller synthesized using the weight (6.6).

In analysing the results, one will find that the first GMFDC (GMFDC 1 using weight (6.3)) has a gap margin of 0.42, the second GMFDC (GMFDC 2 using weight (6.6)) has a gap margin of 0.36, and the corresponding CGDC have a gap margin on the order of machine precision. It can be seen, however, that the CGDC result in a stable but poorly damped system. The four controllers are compared using two control approaches in Figure 6.5.

6.3 Hardware Results

The hardware implementation of the inverter is shown in Figure 6.6. A single grid-connected inverter was tested in open loop to validate the analytical model (see

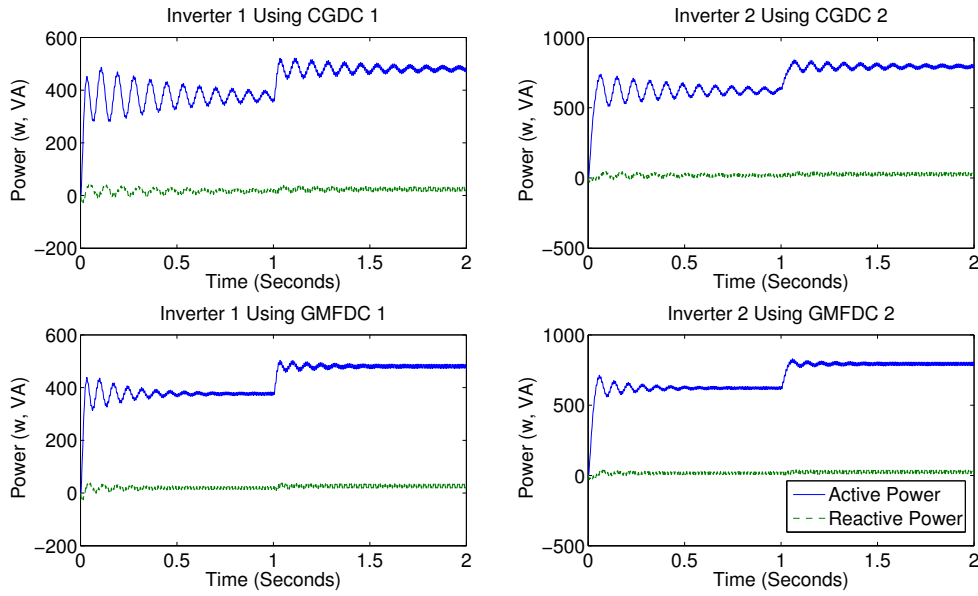


Figure 6.5: Transient plot comparing two system configurations. One configuration uses two CGDC and the other system configuration uses two GMFDC. It can be seen that the system with CGDC is poorly damped, but is stable. This is an indication of the conservative nature of the gap margin. It will be shown in section 6.3 that CGDC is not robust and destabilizes the physical system.

section 2.3), and two islanded inverters were operated in closed loop to compare CGDC to GMFDC.

The open loop system was tested by connecting an inverter to a grid-connected auto-transformer. The inverter was initially operated in closed loop to establish an operating point. After a given period of time, the frequency and voltage setpoints were stored, a given loop opened (at either the frequency input or voltage input), and the setpoints perturbed by a specified amount. The test setup was implemented in Simulink as shown in Figure 6.7 and Figure 6.8.

A critical aspect of validating the analytical model is to characterize all the components in the system. This includes determining the output impedance of the

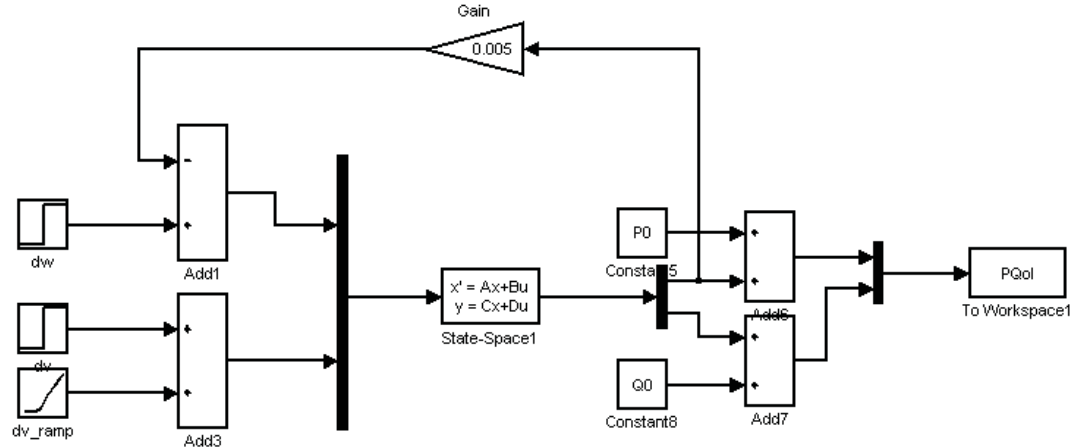


Figure 6.8: Architecture used to test open loop voltage perturbations in hardware.

auto-transformer was calculated using the procedure in Figure 6.9 and (6.9). The output resistance of the auto-transformer was calculated as 12.5Ω . One should note that the figure and expression denote the impedance as a resistance without any inductive component. The input and output voltages were compared on an oscilloscope and it was found that there was negligible phase difference between the two waveforms (on the order of 2°). One may therefore consider the output impedance to be a pure resistance at 60 Hz.

$$R_T = R_B \frac{V_{TH} - V_{Loaded}}{V_{Loaded}} \quad (6.9)$$

The same procedure was used to determine the output impedance of the inverter. It was calculated as 0.02Ω which is negligible compared to the output resistance of the auto-transformer and is neglected in this analysis. The impedance between the inverter and auto-transformer is easily determined by measuring the inductor with an LCR meter. The coupling inductance was measured as $900 \mu H$ with a parasitic resistance of 0.02Ω . One may then easily calculate the impedance at $60 Hz$ and include the parameters in the analytical model.

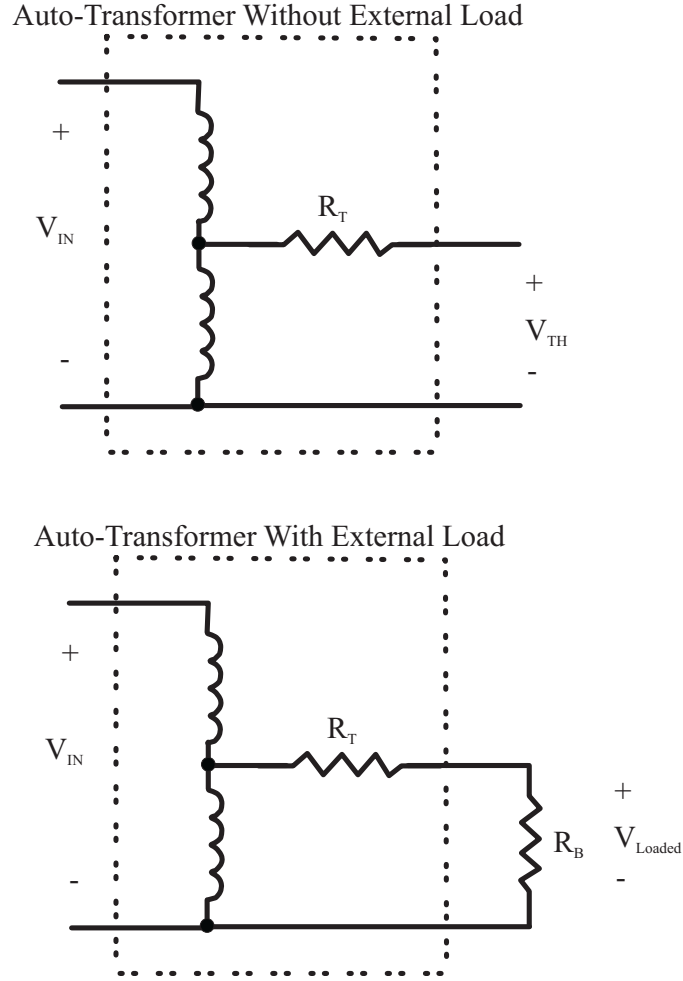


Figure 6.9: Methodology used to characterize Thevenin equivalent of auto-transformer.

Results of the hardware experiment are shown in figures 6.11-6.14. For the case where the frequency channel is subjected to a perturbation of 0.05 rad/s in Figure 6.11, the $P - \omega$ slope has an error of 10.2% and the $Q - v$ slope has an error of 110%. The error is attributed to a change in operating point and nonlinearities in the system.

For the case where the frequency channel is subjected to a perturbation of 0.1 rad/s in Figure 6.12, the $P - \omega$ slope has an error of 54.7% and the $Q - v$ slope has an error of 71.6%. The error is attributed to a change in operating point and nonlinearities in the system.

For the case where the voltage channel is subjected to a perturbation of 2V in Figure 6.13, the $P - \omega$ and $Q - v$ channels have no discernable steady state error. There is, however, some dynamic error that may be seen in the transition from one operating point to another. The error is due in part to perturbations in the inverter output voltage and grid voltage. It can also be seen that the error is small and will not be estimated in this report.

For the case where the voltage channel is subjected to a perturbation of 5V in Figure 6.14, the $P - \omega$ has no discernable error and the $Q - v$ channel has 39.4% steady state error. The error in the $Q - v$ channel appears to be due to linearization error. There is also some dynamic error that may be seen in the transition from one operating point to another. The error is due in part to perturbations in the inverter output voltage and grid voltage. It can also be seen that the error is small and will not be estimated in this report.

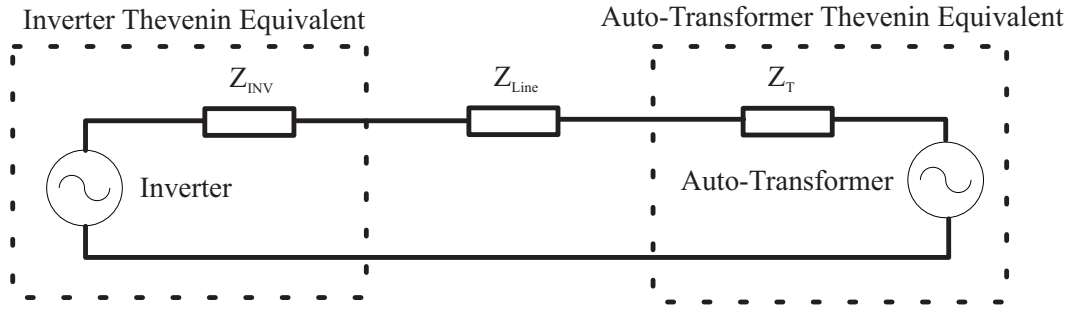


Figure 6.10: This figure depicts parasitics that influence hardware. Note that the inverter output impedance is negligible for this particular case. In general it is good to consider the effect of inverter output impedance and include or exclude it accordingly.

The inverters were then operated in closed loop in a microgrid as shown in Figure 6.15. The microgrid has parameters given in Table 6.1. One will note that the table refers to the DC gains of two controllers. These are the DC gains of two unique GMFDC controllers (GMFDC 1 and GMFDC 2) and two corresponding constant gain controllers (CGDC 1 and CGDC 2). This was done to simulate imbalances that would naturally occur in a microgrid.

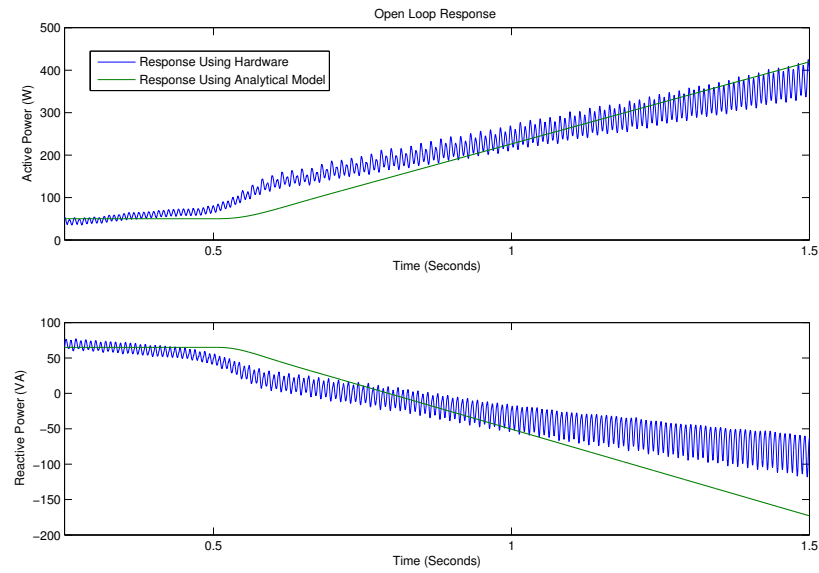


Figure 6.11: Transient response of active power (top) and reactive power (bottom) for a perturbation of 0.05 rad/s.

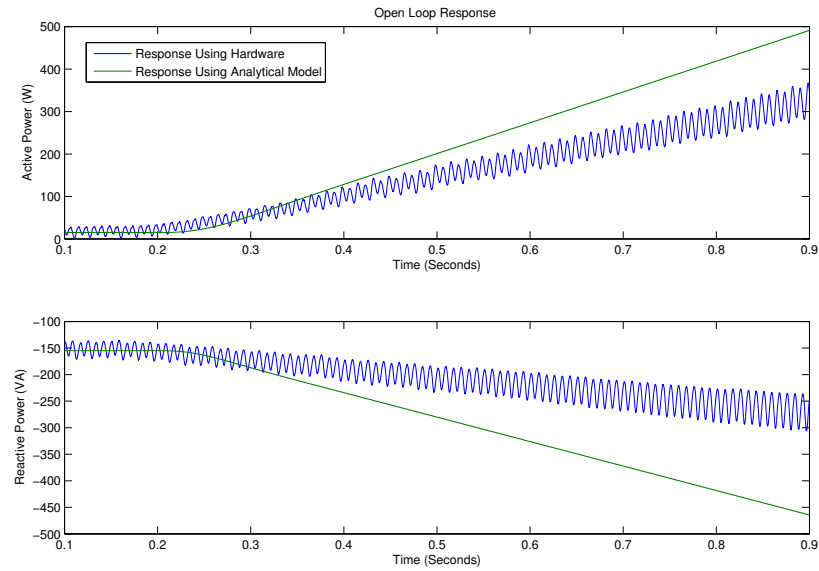


Figure 6.12: Transient response of active power (top) and reactive power (bottom) for a perturbation of 0.1 rad/s.

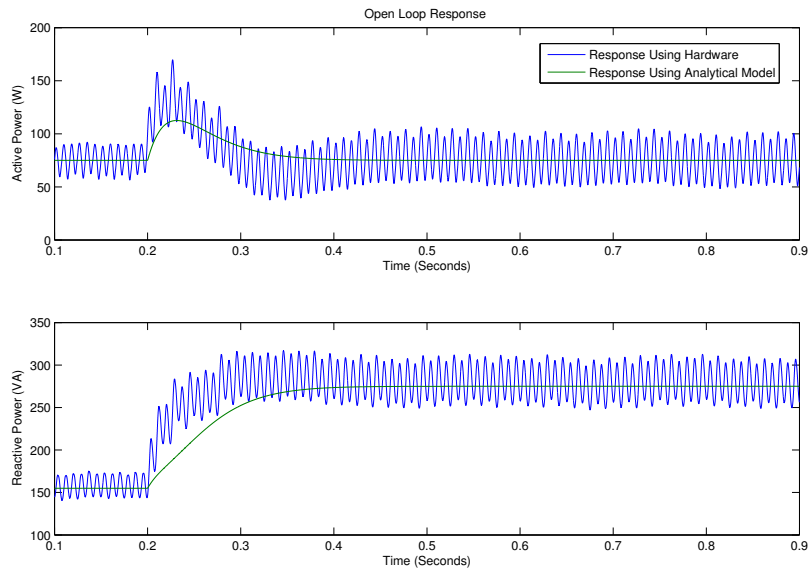


Figure 6.13: Transient response of active power (top) and reactive power (bottom) for a perturbation of 2V.

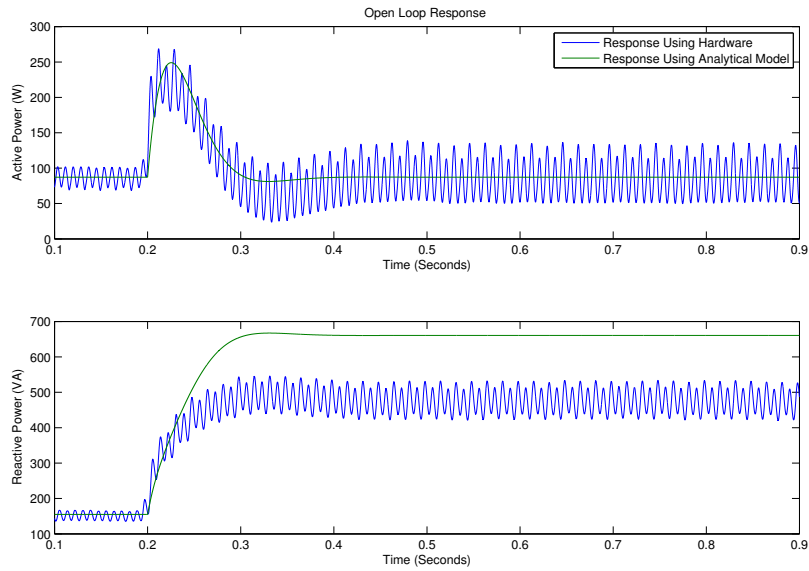


Figure 6.14: Transient response of active power (top) and reactive power (bottom) for a perturbation of 5V.

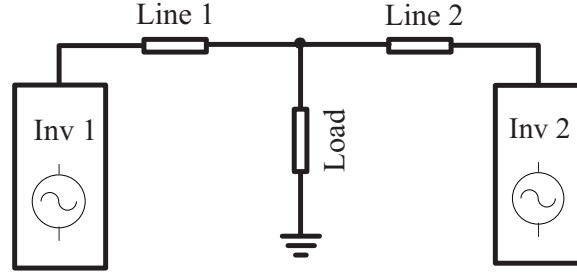


Figure 6.15: Two-inverter configuration used in the hardware implementation.

Table 6.1: Parameters used for both inverter 1 and inverter 2 shown in Figure 6.15.

Parameter	Value
Unloaded Inverter Voltage	$100V_{\text{RMS}}$
Unloaded Inverter Frequency	377 rad/s
Line Impedance	$0.02 + j 0.31 \Omega$
Lowpass Filter	$\frac{8883}{s^2 + 133.3 \cdot s + 8883}$
Controller 1 DC Gains	$k_p = 3.5 \cdot 10^{-3} \text{ rad/s/w}$ $k_v = 1.4 \cdot 10^{-3} \text{ V/VA}$
Controller 2 DC Gains	$k_p = 2.1 \cdot 10^{-3} \text{ rad/s/w}$ $k_v = 2.7 \cdot 10^{-4} \text{ V/VA}$

As noted in the previous section, the GMFDC controllers are 8^{th} order systems and no model order reduction was applied. The transient power response of both inverters operating using either set of controllers is shown in Figure 6.16. The transient voltage and current response of the inverters is shown in Figure 6.17. From these figures it is readily apparent that the inverters using constant gain droop control are unstable. In contrast to the constant gain case, the inverters using GMFDC controllers are stable and do not have an excessive amount of overshoot. It can be seen that the advanced approaches to modeling and control have a clear advantage in practical implementations.

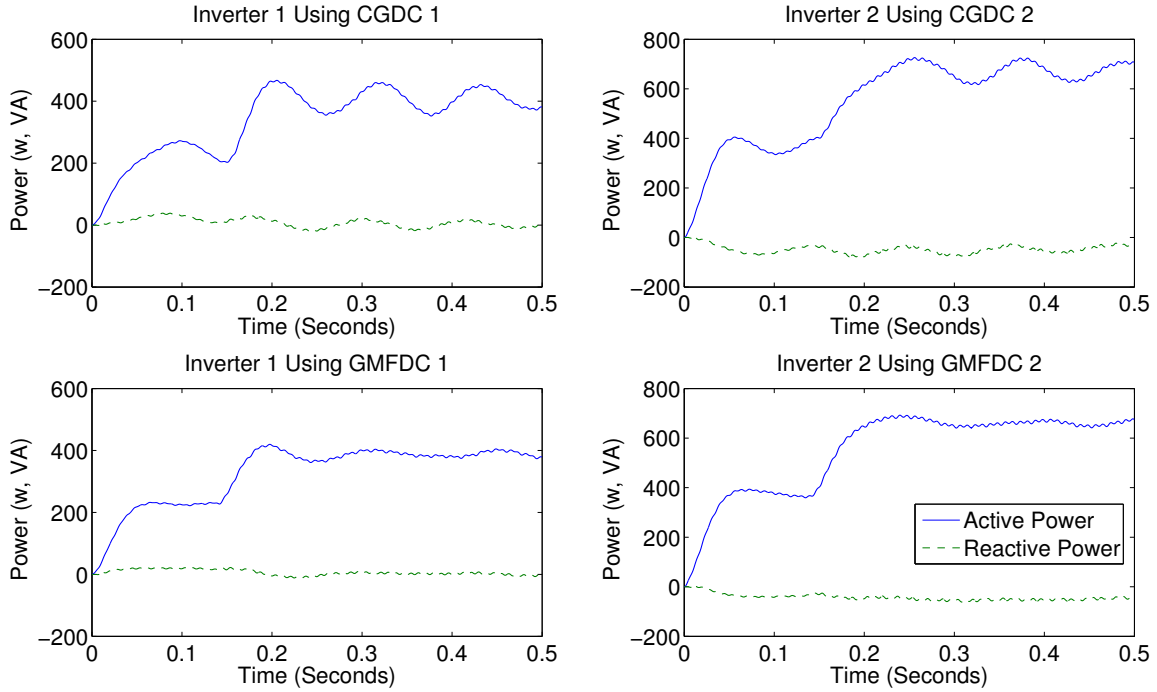


Figure 6.16: Comparison of transient power response using hardware. Inverters 1 and 2 are configured as shown in Figure 6.15. Controller 1 denotes a controller with larger DC gain than controller 2. The inverters using constant gain controllers are clearly unstable and the inverters using GMFDC controllers are stable and well behaved. It can be seen the the DC gain and dynamics, or lack of dynamics, have a strong impact on the stability and dynamic performance of the system.

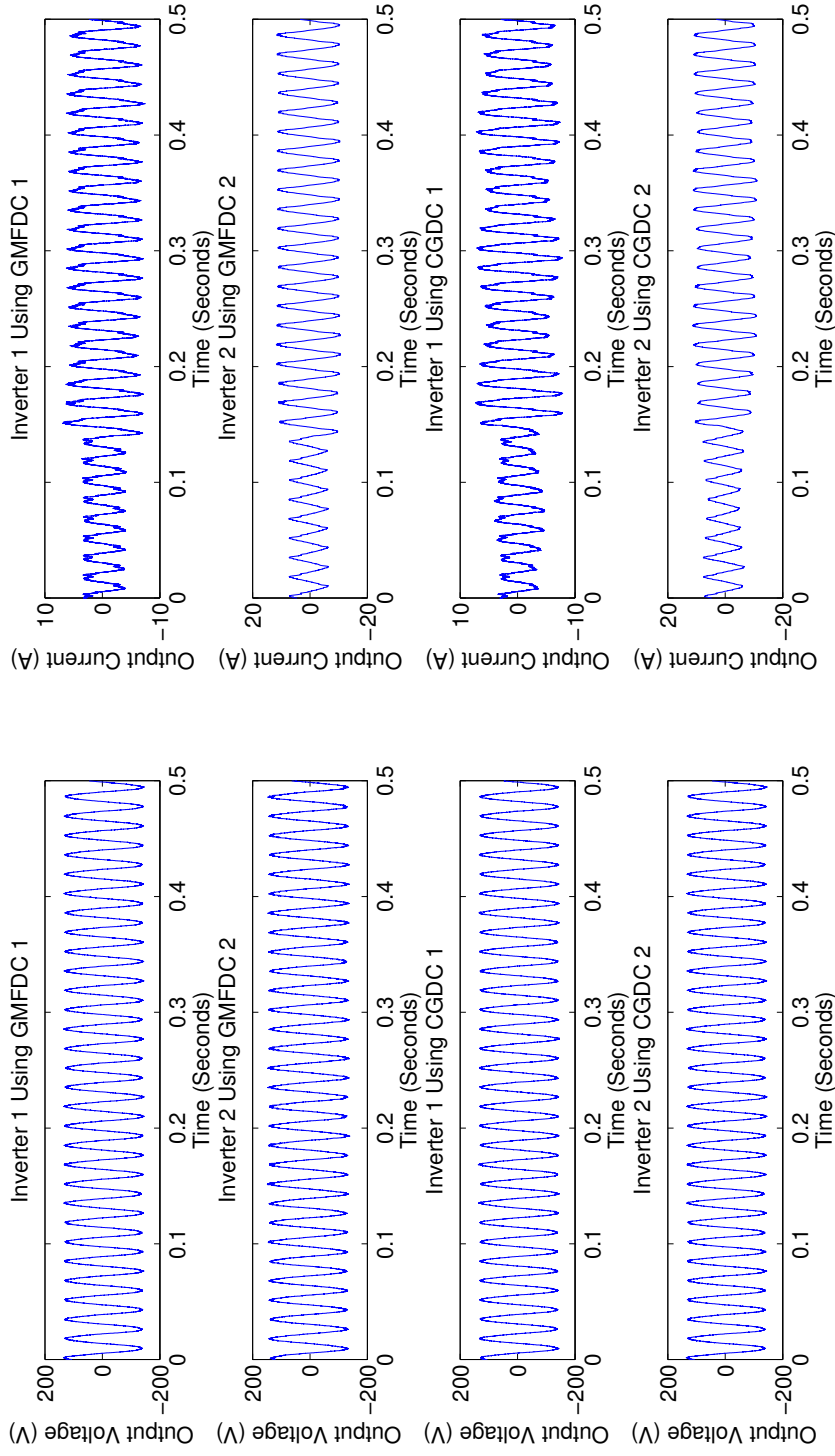


Figure 6.17: Comparison of transient voltage and current response using hardware. Inverters 1 and 2 are configured as shown in Figure 6.15. Controller 1 denotes a controller with larger DC gain than controller 2. The inverters using constant gain controllers are clearly unstable and the inverters using GMFDC controllers are stable and well behaved. It can be seen the the DC gain and dynamics, or lack of dynamics, have a strong impact on the stability and dynamic performance of the system.

Chapter 7

SUMMARY AND CONCLUSIONS

In this report, a variety of modeling and control methods have been presented. The primary contributions of this work are to model the microgrid in a general framework using a Thevenin equivalent circuit for both nominal and parameter varying cases, the design and simulation of robust multi-variable controllers for the nominal plant, gain scheduled (polytopic) robust controllers for the time-varying plant, bumpless controllers for the time-varying plant, and robustness analysis of the nominal system using the gap metric. It was shown that robust control methods yield superior performance due to their greater degree of freedom. The classical constant gain droop controller was implemented in hardware using two 5 kw inverters. It was shown that the hardware is in agreement with the analytical model derived in this thesis and is useful for control design. It was also shown that the traditional constant gain approach results in an unstable system and that the same system is stabilized using robust controllers.

In the future more work will be done by deriving nonlinear models useful for control design, real-time system identification, and the implementation of adaptive controllers in hardware.

REFERENCES

- [1] *LMI Control Toolbox for Use with Matlab.*
- [2] P. Apkarian, P. Gahinet, and G. Becker. Self-scheduled h-infinity control of linear parameter-varying systems: a design example. *Automatica*, 9:1251–1261, 1995.
- [3] Alan B. Arehart and William A. Wolovich. Bumpless switching controllers. In *Proceedings of the 35th Conference on Decision and Control*, 1996.
- [4] L. Asiminoaei, R. Teodorescu, F. Blaabjerg, and U. Borup. A digital controlled pv-inverter with grid impedance estimation for ens detection. *Power Electronics, IEEE Transactions on*, 20(6):1480 – 1490, 2005.
- [5] Behrooz Bahrani, Houshang Karimi, and Reza Irvani. Stability analysis and experimental validation of a control strategy for autonomous operation of distributed generation units. *IEEE*, pages 464–471, 2010.
- [6] E. Barklund, N. Pogaku, M. Prodanovic, C. Hernandez-Aramburo, and T.C. Green. Energy management in autonomous microgrid using stability-constrained droop control of inverters. *Power Electronics, IEEE Transactions on*, Volume: 23 , Issue: 5:2346 – 2352, 2008.
- [7] J. Bendtsen, J. Stoustrup, and K. Trangbaek. Bumpless transfer between advanced controllers with applications to power plant control. In *Proceedings of the 42nd Conference on Decision and Control*, 2003.
- [8] J. D. Bendtsen, J. Stoustrup, and K. Trangbaek. Bumpless transfer between

observer-based gain scheduled controllers. *International Journal of Control*, 78, No. 7:491504, 2005.

- [9] P. Bikash and B. Chaudhuri. *Robust Control In Power Systems*. Springer, 2005.
- [10] Shin-Young Cheong and M.G. Safonov. Slow-fast controller decomposition bumpless transfer for adaptive switching control. *Automatic Control, IEEE Transactions on*, 57:721 – 726, 2012.
- [11] Edwin Chong and Stanislaw Zak. *An Introduction to Optimization*. Wiley, 2008.
- [12] Il-Yop Chung, Wenxin Liu, David Cartes, and Karl Schoder. Control parameter optimization for a microgrid system using particle swarm optimization. *IEEE*, pages 837–842, 2008.
- [13] E.A.A. Coelho, P.C. Cortizo, and P.F.D. Garcia. Small signal stability for single phase inverter connected to stiff ac system. In *Industry Applications Conference, 1999. Thirty-Fourth IAS Annual Meeting. Conference Record of the 1999 IEEE*, volume 4, pages 2180 –2187 vol.4, 1999.
- [14] E.A.A. Coelho, P.C. Cortizo, and P.F.D. Garcia. Small-signal stability for parallel-connected inverters in stand-alone ac supply systems. *Industry Applications, IEEE Transactions on*, 38(2):533 –542, 2002.
- [15] E.A.A. Coelho, B.R. Menezes, P.C. Cortizo, and P.F. Donoso Garcia. Sliding mode controller for parallel connected inverters. In *Power Electronics Congress, 1998. CIEP 98. VI IEEE International*, pages 96 –102, October 1998.

- [16] K. De Brabandere, B. Bolsens, J. Van den Keybus, A. Woyte, J. Driesen, and R. Belmans. A voltage and frequency droop control method for parallel inverters. *Power Electronics, IEEE Transactions on*, 22(4):1107–1115, july 2007.
- [17] Richard C. Dorf and Robert H. Bishop. *Modern Control Systems*. Pearson Prentice Hall, 2005.
- [18] R.; Falcones, S.; Xiaolin Mao; Ayyanar. Topology comparison for solid state transformer implementation. *Power and Energy Society General Meeting, 2010 IEEE*, pages 1 – 8, 2010.
- [19] R.G. Ford and K. Glover. An application of coprime factor based anti-windup and bumpless transfer control to the spark ignition engine idle speed control problem. In *Proceedings of the 39th IEEE Conference on Decision and Control*, 2000,.
- [20] T.T. Georgiou and M.C. Smith. W-stability of feedback systems. *Systems and Control Letters*, 13:271–277, 1989.
- [21] J.M. Guerrero, N. Berbel, J. Matas, L.G. de Vicuna, and J. Miret. Decentralized control for parallel operation of distributed generation inverters in microgrids using resistive output impedance. In *IEEE Industrial Electronics, IECON 2006 - 32nd Annual Conference on*, pages 5149–5154, 2006.
- [22] J.M. Guerrero, L. Garcia de Vicuna, J. Matas, M. Castilla, and J. Mi. Output impedance design of parallel-connected ups inverters with wireless load-sharing control. *IEEE Transactions on Industrial Electronics*, 52 NO.4:1126–1135, 2005.

- [23] J.P. Hespanha and S.A. Morse. Switching between stabilizing controllers. *Automatica*, 38:1905-1917, 2002.
- [24] Shi-Ping Hsu, Art Brown, Loman Rensink, and R.D. Middlebrook. Modelling and analysis of switching dc-to-dc converters in constant-frequency current-programmed mode. *Proceedings of the IEEE Power Electronics Specialists Conference*, pages 169–186, 1979.
- [25] Jiabing Hu, Lei Shang, Yikang He, and Z. Q. Zhu. Direct active and reactive power regulation of grid-connected dc/ac converters using sliding mode control approach. *IEEE Transactions on Power Electronics*, 26:210–222, 2011.
- [26] Alex Q. Huang, Mariesa L. Crow, Gerald Thomas Heydt, Jim P. Zheng, and Steiner J. Dale. The future renewable electric energy delivery and management (freedm) system: The energy internet. *Proceedings of the IEEE*, 99:133–148, 2011.
- [27] T. Hussein, M. S. Saad, A. L. Elshafei, and A. Bahgat. Robust adaptive fuzzy logic power system stabilizer. *Expert Systems with Applications*, 36:12104–12112, 2009.
- [28] S.V. Iyer, M.N. Belur, and M.C. Chandorkar. A generalized computational method to determine stability of a multi-inverter microgrid. *Power Electronics, IEEE Transactions on*, Volume: 25 , Issue: 9:2420 – 2432, 2010.
- [29] Hongxin Ju, Ming Ding, Jianhui Su, Yan Du, and Liuchen Chang. Communicationless parallel inverters based on inductor current feedback control. *IEEE*, 2007.

- [30] T. Kawabata and S. Higashino. Parallel operation of voltage source inverters. *IEEE Transactions on Industry Applications*, 24:281–287, 1988.
- [31] Erwin Kreyszig. *Advanced Engineering Mathematics*. Wiley, 1999.
- [32] Alexander Lanzon. Simultaneous synthesis of weights and controllers in h₈ loop-shaping. *Proceedings of the 40th IEEE Conference on Decision and Control*, pages 670–675, 2001.
- [33] R.H. Lasseter. Microgrids. *Power Engineering Society Winter Meeting, 2002. IEEE*, 1:305 – 308, 2002.
- [34] Telles B. Lazzarin, Guilherme A. T. Bauer, and Ivo Barbi. A control strategy for parallel voltage source inverters. In *Power Electronics Conference, 2009. COBEP '09. Brazilian*, pages 80–87, 2009.
- [35] J. Liang, T.C. Green, G. Weiss, and Q.C. Zhong. Hybrid control of multiple inverters in an island-mode distribution system. *Power Electronics Specialist Conference, 2003. PESC '03. 2003 IEEE 34th Annual*, pages 61–66, 2003.
- [36] H.Z. Maia, J.O. Pereira Pinto, and E.A. Alves Coelho. Power response optimization of inverter grid parallel operation using v-; and q-v curves, and phase feedback based on genetic algorithm. In *Industrial Electronics Society, 2007. IECON 2007. 33rd Annual Conference of the IEEE*, pages 1679 –1684, 2007.
- [37] Xiaolin Mao, Sixifo Falcones, and Raja Ayyanar. Energy-based control design for a solid state transformer. *Power and Energy Society General Meeting, 2010 IEEE*,

pages 1–7, 2010.

- [38] D. McFarlane and K Glover. A loop-shaping design procedure using h8 synthesis. *IEEE Transactions on Automatic Control*, Volume 37, Issue 6:759–769, 1992.
- [39] A. Mohd, E. Ortjohann, D. Morton, and O. Omari. Review of control techniques for inverters in parallel operation. *Electric Power Systems Research*, 80:1477–1487, 2010.
- [40] H. Niemann, J. Stoustrup, and R.B. Abrahamsen. A note on switching between multivariable controllers. *Optimal Control Applications and Methods*, 25, pp. 5166, 2004, 25:5166, 2004.
- [41] Oliver and Shakiban. *Applied Linear Algebra*. Pearson Prentice Hall, 2006.
- [42] M. Pasamontes, J.D. Alvarez, J.L. Guzman, and M. Berenguel. Bumpless switching in control - a comparative study. In *Emerging Technologies and Factory Automation (ETFA), 2010 IEEE Conference on*, 2010.
- [43] J.A. Pecas Lopes, C.L. Moreira, and A.G. Madureira. Defining control strategies for analysing microgrids islanded operation. In *Power Tech, 2005 IEEE Russia*, pages 1–7, June 2005.
- [44] J.A.P. Pecas Lopes, C.L. Moreira, and A.G. Madureira. Defining control strategies for microgrids islanded operation. *Power Systems, IEEE Transactions on*, 21(2):916 – 924, May 2006.

- [45] Y. Pei and et al. Auto-master-slave control technique of parallel inverters in distributed ac power systems and ups. In *IEEE 35th Annual Power Electronics Specialists Conference*, 2004.
- [46] Z. Petruzzello and G. Joos. A novel approach to paralleling of power converter units with true redundancy. *21st Annual IEEE Power Electronics Specialists Conference*, 1990.
- [47] N. Pogaku, M. Prodanovic, and T.C. Green. Modeling, analysis and testing of autonomous operation of an inverter-based microgrid. *Power Electronics, IEEE Transactions on*, Volume: 22 , Issue: 2:613 – 625, 2007.
- [48] M. Prodanovic, T.C. Green, and H. Mansir. A survey of control methods for three-phase inverters in parallel connection. *International Conference on (IEE Conf. Publ. No. 475)*, pages 472 – 477, 2000.
- [49] Skogestad and Postlethwaite. *Multivariable Feedback Control*. Wiley, 2005.
- [50] M. Soliman, A. L. Elshafei, F. Bendary, and W. Mansour. Lmi static output-feedback design of fuzzy power system stabilizers. *Expert Systems with Applications*, 36:6817–6825, 2009.
- [51] Joel Steenis, Kostas Tsakalis, and Raja Ayyanar. Robust control of an islanded microgrid. In *IECON12*, 2012.
- [52] James Stewart. *Calculus: Early Transcendentals*. Brooks/Cole, 1999.

- [53] S. D. Sudhoff, S. F. Glover, P. T. Lamn, D. H. Schmucker, and D. E. Delisle. Admittance space stability analysis of power electronic systems. *IEEE Transactions on Aerospace and Electronic Systems*, 36:965–973, 2000.
- [54] J. C. Vasquez, J. M. Guerrero, A. Luna, P. Rodriguez, and R. Te. Adaptive droop control applied to voltage-source inverters operating in grid-connected and islanded modes. *IEEE Transactions on Industrial Electronics*, 56 NO. 10:4088–4096, 2009.
- [55] Glenn Vinnicombe. *Measure the Robustness of Feedback Systems*. PhD thesis, Churchill College, 1992.
- [56] Vatche Vorperian. *Fast Analytical Techniques for Electrical and Electronic Circuits*. Cambridge University Press, 2002.
- [57] L. Wang, X. Q. Guo, H. R. Gu, W.Y. Wu, and J. M. Guerrero. Precise modeling based on dynamic phasors for droop-controlled parallel-connected inverters. In *Industrial Electronics (ISIE), 2012 IEEE International Symposium on*, 2012.
- [58] Wei Yao, Min Chen, Jose Matas, Josep Gurrero, and Zhao-Ming Qian. Design and analysis of the droop control method for parallel inverters considering the impact of the complex impedance on the power sharing. *IEEE Transactions on Industrial Electronics*, 58, No2:576–588, 2011.
- [59] L. Zaccarian and A.R. Teel. A common framework for anti-windup, bumpless transfer and reliable designs. *Automatica*,, 38,:17351744, 2002.